The Dissertation Committee for Eun Sung Lee certifies that this is the approved version of the following dissertation:

STRUCTURAL AND ELECTROCHEMICAL CHARACTERIZATION OF HIGH-ENERGY OXIDE CATHODES FOR LITHIUM ION BATTERIES

Committee:

Arumugam Manthiram, Supervisor

Paulo J. Ferreira

Desiderio Kovar

Charles Buddie Mullins

Keith J. Stevenson

STRUCTURAL AND ELECTROCHEMICAL CHARACTERIZATION OF HIGH-ENERGY OXIDE CATHODES FOR LITHIUM ION BATTERIES

by

Eun Sung Lee, B.S.; M.S.

Dissertation

Presented to the Faculty of the Graduate School of

The University of Texas at Austin

in Partial Fulfillment

of the Requirements

for the Degree of

Doctor of Philosophy

The University of Texas at Austin

December 2012

Dedication

Dedicated to my wife and family

Acknowledgements

First of all, I would like to express my deep gratitude to my supervisor, Professor Arumugam Manthiram, for his inspiring guidance and continuous support through the course of my work. Without his valuable guidance, I could not have developed my research work successfully. I also thank all my committee members, Professors Paulo Ferreira, Desiderio Kovar, Charles Buddie Mullins, and Keith Stevenson for their helpful suggestions on my dissertation.

Additionally, I would like to thank Dr. Ashfia Huq at the Oak Ridge National Laboratory for her help with the neutron diffraction experiments and refinement. I would like to thank Dr. Kyung-Wan Nam at the Boorkhaven National Laboratroy for his help with synchrotron XRD experiment. I would like to thank the former and current members in Prof. Manthiram's group, specifically, Dr. Sukuen Yoon, Dr. Jung-Hyun Kim, Dr. Danielle Applestone, James Knight, Katharine Chemelewski, Thomas Cochell, Arturo Gutierrez, Yu-Sheng Su, and Zach Moorhead-Rosenberg for their kind help and support. I also thank the Department of Energy and NASA for financial support.

Above all, I am really thankful to my wife, Nakyung Moon, and my family. Without their support and sacrifice during the course of my work, it would not have been possible for me to finish my dissertation successfully.

STRUCTURAL AND ELECTROCHEMICAL CHARACTERIZATION OF HIGH-ENERGY OXIDE CATHODES FOR LITHIUM ION BATTERIES

Eun Sung Lee, Ph.D.

The University of Texas at Austin, 2012

Supervisor: Arumugam Manthiram

Lithium-ion batteries are the most promising rechargeable battery system for both vehicle applications and stationary storage of electricity produced from renewable sources such as solar and wind energies. However, the current lithium ion technology does not fully meet the requirements of these applications in terms of energy and power density. One approach to realizing a combination of high energy and power density is to use a composite cathode that consists of the high-capacity lithium-rich layered oxide $Li[Li,Mn,Ni,Co]O_2$ and the high-voltage spinel oxide $LiMn_{1.5}Ni_{0.5}O_4$. This dissertation explores the unique structural characteristics and their effect on the electrochemical performance of the layered-spinel composite oxide cathodes along with individual layered and spinel oxides over a wide voltage range (5.0 – 2.0 V).

Initially, the effect of cation ordering on the electrochemical and structural characteristics of $LiMn_{1.5}Ni_{0.5}O_4$ during cycling between 5.0 and 2.0 V were investigated by an analysis of the X-ray diffraction (XRD) and electrochemical data. Structural studies revealed that the cation ordering affects the size of the empty-octahedral sites in the spinel lattice. The differences in the size of the empty-octahedral sites affect the discharge profile below 3 V due to the variation in lattice distortion during lithium ion

insertion into 16c octahedral sites. With the doped $LiMn_{1.5}Ni_{0.5-x}M_xO_4$ (M = Cr, Fe, Co, and Ga) spinels, different dopant ions have different effects on the degree of cation ordering due to the differences in ionic radii and surface-segregation characteristics.

The compositional and wt.% variations of the layered and spinel phases from the nominal values in the layered-spinel composites were obtained by employing a joint XRD and neutron diffraction (ND) Rietveld refinement method. With the obtained composition and *ex-situ* XRD data, the mechanism for the increase in capacity and the facile phase transformation of the layered phase in the composite cathodes to a 3 V spinel-like phase during cycling was proposed. Investigations focused on synthesis temperature revealed that the electrochemical characteristics of the composites are highly affected by the synthesis temperature due to the change in the surface area of the sample and cation ordering of the spinel phase.

In addition, the electrochemical performance of the lithium-rich layered oxide $Li[Li,Mn,Ni,Co]O_2$ could be improved by blending it with a lithium-free insertion host VO_2(B) and by controlling the amount of lithium ions extracted from the layered lattice during the first charge process.

Table of Contents

List of Tables

List of Figures

Chapter 1: Introduction

1.1 LITHIUM ION BATTERIES

Lithium ion batteries have revolutionized portable electronics since they were first commercialized by Sony Inc. in 1991. Recently, lithium-ion batteries are becoming the most promising rechargeable battery system both as a power source for electric vehicles and as energy storage devices for renewable technologies because they offer much higher energy density when compared to other rechargeable systems.

1.1.1 Principle of operation

Similar to other electrochemical devices, lithium ion batteries are composed of four components: cathode, anode, electrolyte, and separator. When compared to other rechargeable systems, lithium ion batteries offer several unique features,[1] such as long shelf life, wide temperature of operation due to the use of nonaqueous electrolytes, and higher cell voltages arising from the use of nonaqueous electrolytes. The schematic illustration of a typical lithium ion battery is shown in Figure 1.1. In this illustration, $LiCoO_2$ serves as the cathode and graphite serves as the anode. During charge, lithium ions from the $LiCoO_2$ cathode migrate through the electrolyte to the graphite anode while the electrons flow from the cathode to the anode through the external circuit. During discharge, lithium ions from the graphite anode migrate through the electrolyte to the $Li_{1-x}CoO_2$ cathode while the electrons flow from the anode to the cathode through the external circuit.

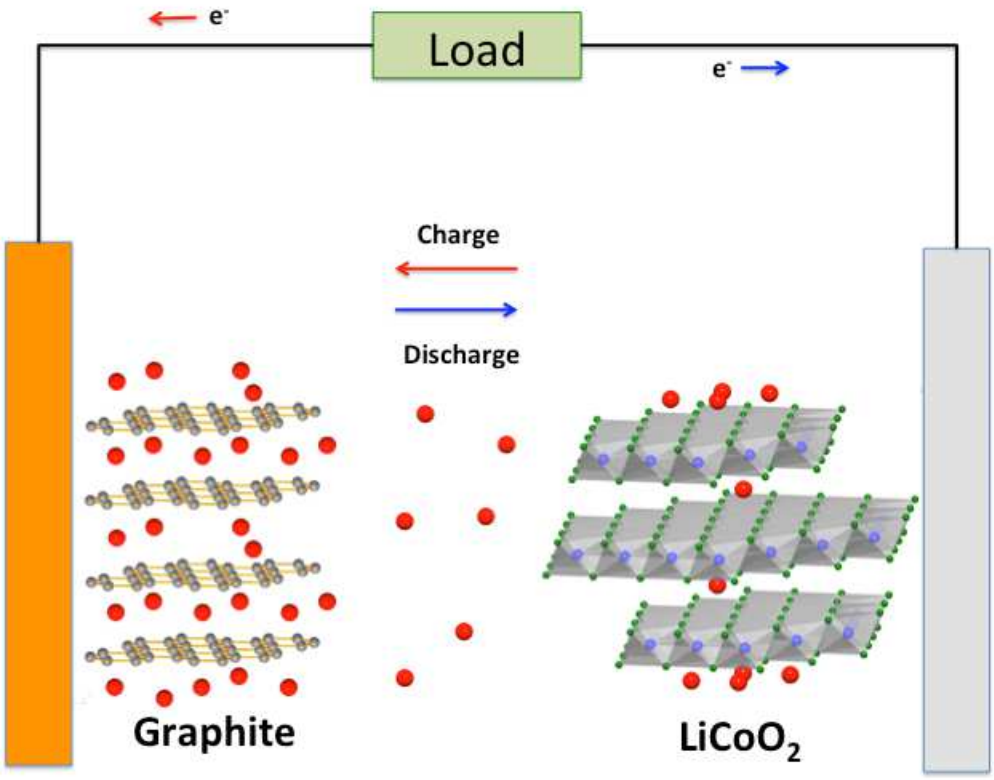

Figure 1.1. Schematic illustration of the lithium ion battery during the charge-discharge process.

1.1.2 Design consideration

In order to realize high voltage and energy in a lithium ion battery, thermodynamic considerations are needed to choose the electrode materials and electrolyte. The schematic energy diagram of a lithium ion battery at open circuit is shown Figure 1.2. The open circuit voltage V_{OC} of a lithium ion battery is determined by the chemical potential difference between the cathode and anode divided by Faraday constant as,

$$V_{oc} = (\mu_c - \mu_a) / F \qquad (1.1)$$

Therefore, a higher operating voltage can be obtained by choosing the cathode material with a lower lithium chemical potential and the anode with a higher lithium chemical potential. However, the chemical potential of both the cathode and anode materials should be located within the band gap E_g of electrolyte. The band gap E_g of the electrolyte is determined by energy difference between the highest occupied molecular orbital (HOMO) and the lowest unoccupied molecular orbital (LUMO) of the electrolyte. If the chemical potential of the cathode (μ_c) is below the HOMO of the electrolyte or if the chemical potential of the anode (μ_a) is above the LUMO of the electrolyte, unwanted redox reactions will occur on the electrolyte.

However, during the operation of lithium ion batteries, the voltage varies from the open circuit voltage due to polarization losses. The operating cell voltage V_{op} can be given as

$$V_{op} = V_{oc} - (\eta_a + \eta_c + IR) \qquad (1.2)$$

The activation overpotential (η_a) is related to the kinetics of electrode reactions. The concentration overpotential (η_c) is related to the mass transfer limitations of the reactants and products during reactions. The ohmic overpotential (IR) is related to the internal impedance of the cell.

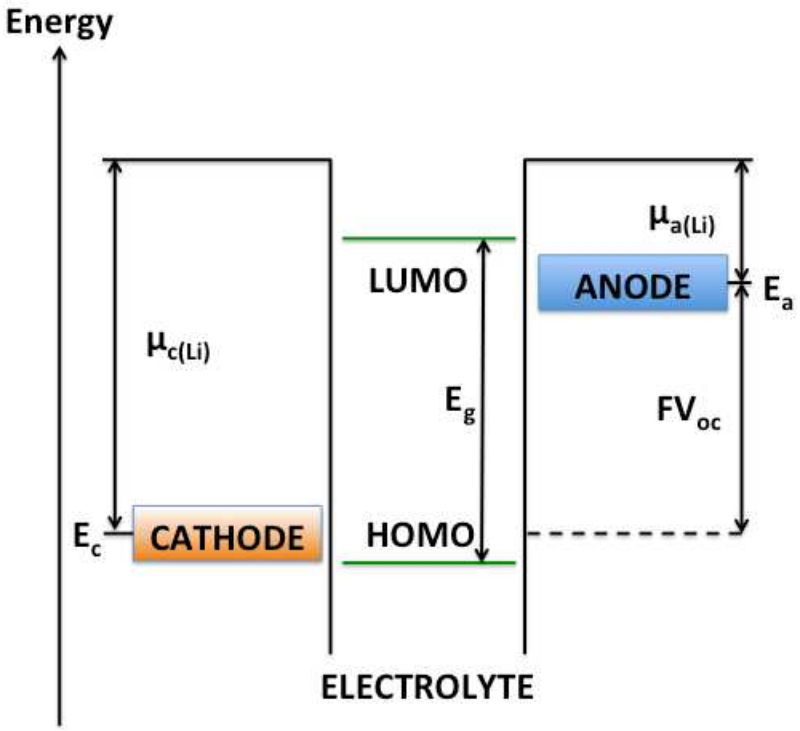

Figure 1.2. Schematic energy diagram of a lithium ion battery at open circuit.[2]

Therefore, the cell components in lithium ion batteries need to meet the requirements as listed below for acceptable performance:

- The difference in the lithium chemical potential between the cathode and anode materials should be large in order to maximize the operating cell voltage
- Cathode and anode materials should be able to insert/extract a large number of lithium ions to maximize the capacity and energy density
- The structural changes of the cathode and anode materials should be minimal in order to get good cycle performance

- Cathode and anode materials should have good electronic and lithium ion conductivity to support high power density during charge/discharge
- The electrolyte should have good lithium ion conductivity and a large band gap
- Cathode, anode, and electrolyte materials should be inexpensive, environmentally benign, and chemically stable within the operating temperature and voltage ranges

1.1.3 Cathode materials

Since the first commercialization of lithium ion batteries in 1991, most commercial lithium ion batteries have used $LiCoO_2$ as the cathode material. However, several drawbacks of $LiCoO_2$ such as high cost, safety concerns, and limited capacity have led to the research and development of alternative cathode materials. The major commercial cathode materials are compared in Table 1.1. Recently, alternative cathode materials such as spinel $LiMn_2O_4$, olivine $LiFePO_4$, layered $LiNi_{1/3}Mn_{1/3}Co_{1/3}O_2$ are being used in vehicle applications such as hybrid electric vehicle (HEV), plug-in hybrid electric vehicle (PHEV), and electric vehicle (EV) due to their advantages over $LiCoO_2$. Intensive research is on-going to develop new cathode materials with higher operating voltage and capacity because commercial cathode materials currently being used cannot fully satisfy the requirements for large applications. Cathode materials can be categorized by their crystal structure, which will be discussed in the next section.

Table 1.1 Comparison of cathode materials.

Cathode material	Specific capacity (mAh/g)	Advantages	Disadvantages
$LiCoO_2$	140	Good cycle life	Expensive Toxic Safety concerns
$LiMn_2O_4$	120	Better safety High rate capability	Low capacity
$LiFePO_4$	160	Excellent safety	Low volumetric capacity High processing cost
$LiNi_{1/3}Mn_{1/3}Co_{1/3}O_2$	150 - 200	High capacity	Moderately expensive

1.1.3.1 Layered structure

Layered oxides have the α-$NaFeO_2$ structure with the general formula $LiMO_2$ (M = V, Mn, Co, and Ni). The Li^+ and M^{3+} ions occupy the octahedral sites in the alternate (111) planes of the rock salt structure formed by cubic close packed O^{2-} ions as shown in Figure 1.3. A unit cell of α-$NaFeO_2$ structure has three MO_2 layers with the Li^+ ions occupying the octahedral interstitial sites between the MO_2 layers. Therefore, its structure is known as O3-type in Delmas notation.[3]

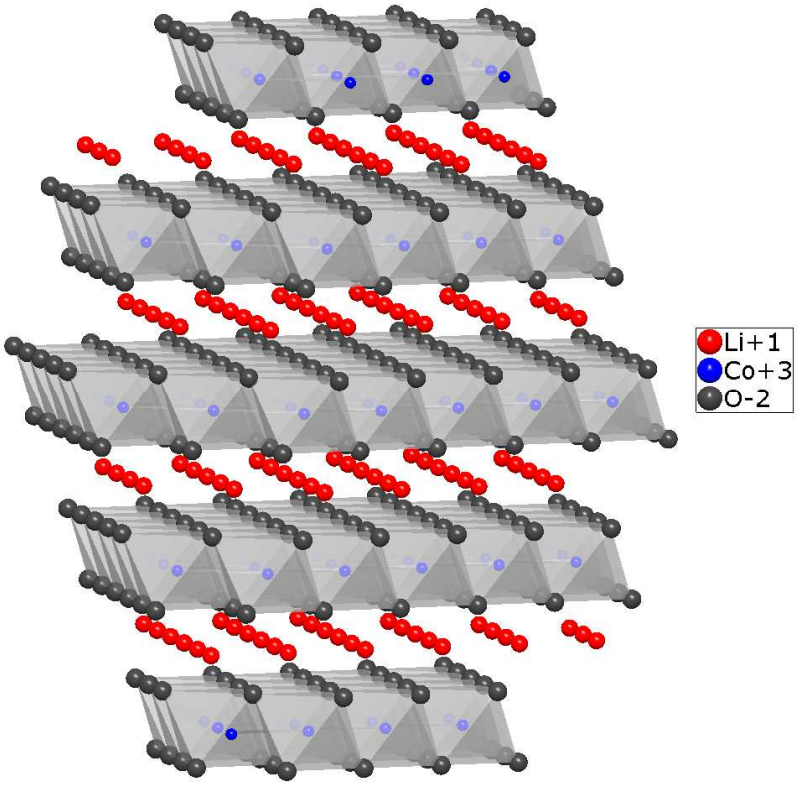

Figure 1.3. Crystal structure of $LiCoO_2$ having the O3 type layered structure.

$LiCoO_2$ has an ideal layered structure with well-defined two-dimensional Li^+ diffusional path due to the large difference in the ionic radii between Li^+ and Co^{3+}. In addition, the direct Co-Co interaction along the edge shared CoO_6 octahedra leads to good electronic conductivity.[4] The highly oxidized $Co^{3+/4+}$ redox couple also gives a high operating voltage of around 4 V vs. Li/Li^+. In addition, many advantageous features such as ease of synthesis, high reversibility, and long cycle life make $LiCoO_2$ a desirable cathode material. However, $LiCoO_2$ also has some drawbacks such as high cost, toxicity, and limited practical capacity of about 140 mAh/g, corresponding to 50 % of the theoretical capacity. The limited practical capacity of $LiCoO_2$ originates from the

chemical instability of the $Co^{3+/4+}$ redox couple, and it can be explained with the qualitative energy band diagram in Figure 1.4.[5-7] Co^{3+} ions in $LiCoO_2$ have a low spin $3d^6$ configuration, where the t_{2g} band is completely filled and the e_g band is empty. During charge lithium ions are extracted from $LiCoO_2$ by the oxidation of Co^{3+} ions to Co^{4+} ions. Since the t_{2g} band is significantly overlapping with the top of the O^{2-}:2p band, deeper lithium ion extraction ($1-x < 0.5$) can cause electron removal from both the $Co^{3+/4+}$:t_{2g} and O^{2-}:2p bands, resulting in a chemical instability of $Li_{1-x}CoO_2$ for $1-x < 0.5$.

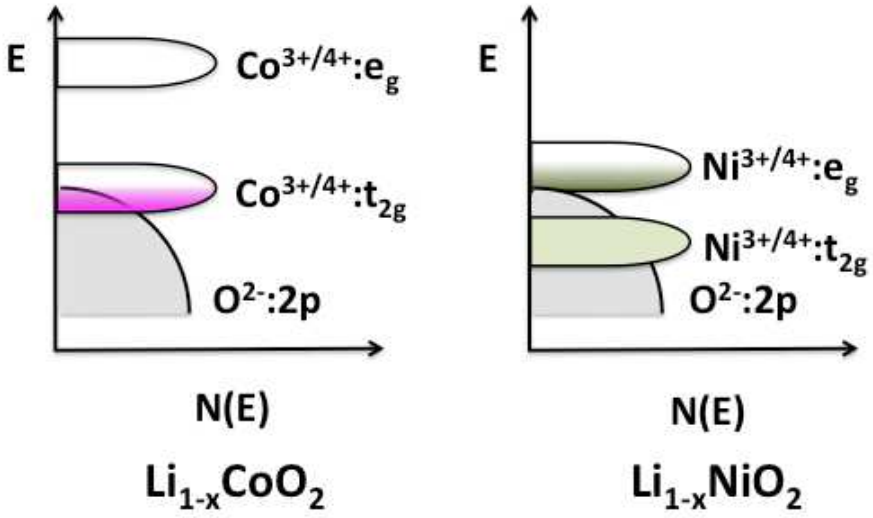

Figure 1.4. Comparison of the qualitative energy diagrams of $Li_{1-x}CoO_2$ and $Li_{1-x}NiO_2$.[4]

$LiNiO_2$ has the same O3 type layered structure as $LiCoO_2$. Nickel is less expensive and less toxic than cobalt, and most importantly $LiNiO_2$ shows higher capacity of around 200 mAh/g. The higher reversible capacity of $LiNiO_2$ originates from the better chemical stability of the $Ni^{3+/4+}$ redox couple compared to the $Co^{3+/4+}$ redox couple as shown in Figure 1.4.[6, 8] With a low spin Ni^{3+} : $t_{2g}^6e_g^1$ configuration, the e_g band barely touches the top of the O^{2-}:2p band and it allows the electron removal mostly from Ni^{3+} :

e_g band, not from the O^{2-}:2p band during lithium ion extraction, resulting in better chemical stability for $LiNiO_2$ compared to $LiCoO_2$.

However, $LiNiO_2$ has several critical drawbacks, which prevent its commercial use as a cathode material. It is very difficult to synthesize $LiNiO_2$ with a perfectly ordered layered structure due to the difficulty of keeping all the Ni as Ni^{3+} and the consequent cation mixing between Ni^{2+} and Li^+.[9, 10] The cation mixing between Ni^{2+} and Li^+ originates from their similar ionic radii. Nickel ions in the lithium layer reduce the diffusion rate of lithium ions. $LiNiO_2$ also suffers from severe capacity fade during cycling due to irreversible phase transformations.[11, 12] In addition, there are safety concerns with $LiNiO_2$ because oxygen is released at elevated temperatures through a spontaneous exothermic reaction due to the chemical instability of Ni^{4+}.

In order to overcome the drawbacks of $LiNiO_2$, cation substitutions for Ni with Al, Mn, and Co have been intensively studied.[13-18] For example, partial substitution of Co for Ni was shown to suppress cation mixing and phase transformation during cycling. Partial substitutions of Mn or Al for Ni may also minimize the exothermic reaction at elevated temperatures. Among them, the layered $LiNi_{1/3}Co_{1/3}Mn_{1/3}O_2$ has become an attractive cathode material for the replacement of $LiCoO_2$ due to its higher capacity and enhanced safety.[19, 20] Another promising layered oxide cathode material is the high-capacity lithium-rich layered oxides, $Li[Li,Mn,Ni,Co]O_2$, which is a solid solution between layered $Li[Li_{1/3}Mn_{2/3}]O_2$ and $LiMO_2$ (M = Mn, Co, and Ni) since it shows high-capacity values of ~ 250 mAh/g when charged above 4.5 V. The high-capacity lithium-rich layered oxides are one topic of my dissertation and will be discussed later.

1.1.3.2 Spinel structure

Spinel oxides have the general formula LiM_2O_4 (M = Ti, V, and Mn). The Li^+ and $M^{3+/4+}$ ions occupy, respectively, the 8a tetrahedral and 16d octahedral sites of the cubic close-packed oxygen array as shown in Figure 1.5. Lithium ions can be extracted reversibly from the 8a tetrahedral sites without collapsing the M_2O_4 spinel framework. The spinel structure provides a three-dimensional pathway for lithium ions through the unoccupied 16c octahedral sites, enabling high-rate capability. Like the layered structure, edge-shared MO_6 octahedra with direct M-M interactions offer good electrical conductivity.[21] Additional lithium ion can also be inserted into the empty 16c octahedral sites of the spinel LiM_2O_4, giving the lithiated spinel $Li_2M_2O_4$.

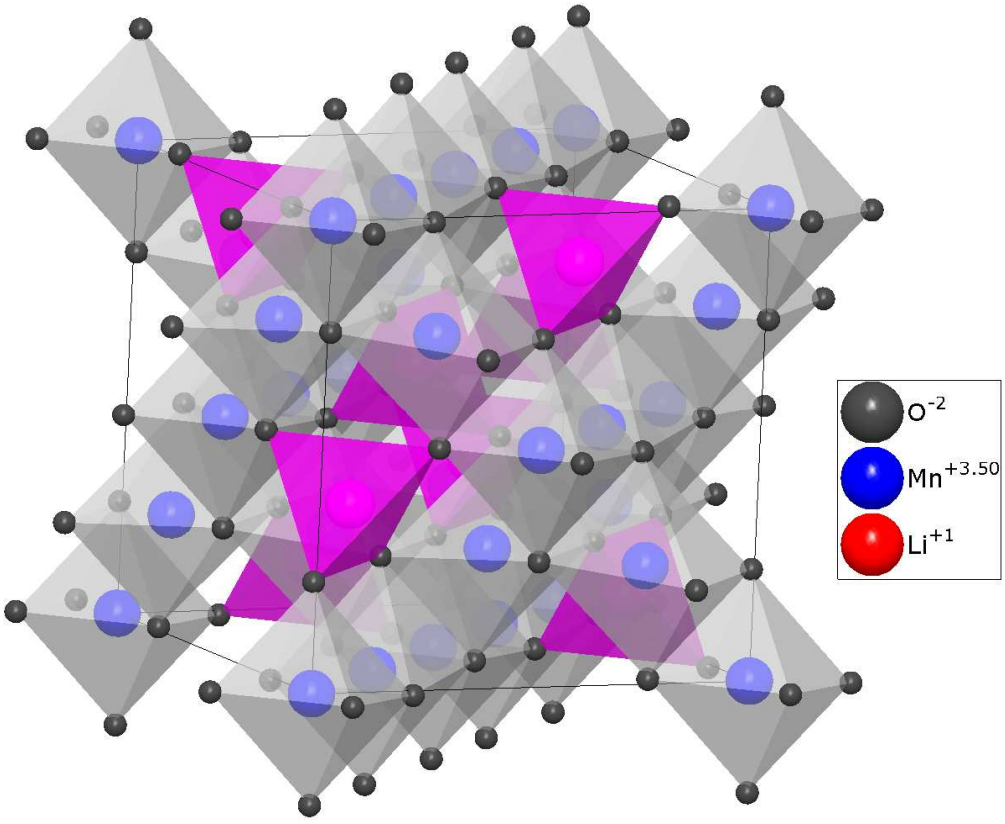

Figure 1.5. Crystal structure of spinel $LiMn_2O_4$.

Spinel $LiMn_2O_4$ has become appealing because Mn is inexpensive and environmentally benign compared to Co and Ni. Therefore, spinel $LiMn_2O_4$ has recently been used as the cathode material of the lithium ion battery system in HEV and PHEV. Two lithium ions can be reversibly inserted into $[Mn_2]O_4$, which exhibit two distinctive voltage plateaus. Lithium ions inserting into the 8a tetrahedral sites occurs around 4 V while maintaining the cubic symmetry, whereas insertion into the 16c octahedral sites occurs around 3 V by a two-phase reaction involving cubic $LiMn_2O_4$ and tetragonal $Li_2Mn_2O_4$.[22, 23] The cubic to tetragonal transition originates from the Jahn-Teller distortion associated with the single electron found in the e_g orbital in the high spin Mn^{3+}: $3d^4$ configuration.[23, 24] However, spinel $LiMn_2O_4$ suffers from severe capacity fade, particularly at elevated temperatures, and its practical capacity is around 120 mAh/g. Several reasons for the capacity fade of $LiMn_2O_4$ have been suggested such as manganese dissolution from the lattice into the electrolyte,[25] Jahn-Teller distortion due to the non-equilibrium cycling,[23, 24] and mircrostrain in the lattice due to the lattice parameter difference between the two cubic phases formed during cycling.[25, 26] In order to overcome the capacity fade problem, cationic substitutions for Mn with Li or other transition metals have been intensively studied to increase the average oxidation state of Mn above 3.5+.[27-30] However, these approaches result in a decrease in capacity in the 4 V region. For example, the lithium excess spinel $Li_{1.33}Mn_{1.67}O_4 (=Li_4Mn_5O_{12})$ exhibits only a 3 V plateau without any 4 V plateau due to the difficulty of further oxidation of Mn^{4+}. On the other hand, the high-voltage spinel $LiMn_{2-x}M_xO_2$ (M = Cr, Fe, Co and Ni) appears to be a promising cathode material because it exhibit a 5 V plateau in addition to a 4 V plateau where lithium ions insert into the 8a tetrahedral sites, giving higher energy and power densities compared to those of $LiMn_2O_4$.[31, 32] High-voltage spinel oxides are another topic of my dissertation and will be discussed in further detail later.

1.1.3.3 Olivine structure

Phospho-olivine cathode materials have the olivine structure with the general formula $LiMPO_4$ (M = Mn, Co, and Ni). Among them, olivine $LiFePO_4$ is a promising cathode material because Fe is abundant, inexpensive, and environmentally benign. The unit cell of olivine $LiFePO_4$ consists of FeO_6 octahedra and PO_4 tetrahedra with the Li^+ and Fe^{2+} ions ordered in alternate (001) planes as shown in Figure 1.6.[33, 34] The olivine $LiFePO_4$ exhibits a good theoretical capacity of 170 mAh/g with a flat voltage of around 3.4 V. It also has good structural and chemical stabilities, resulting in better safety over other cathode materials. However, the low electronic and lithium ion conductivities of olivine $LiFePO_4$ limit its reversible capacity and rate capability. Carbon or conducting polymer coatings on the nano-sized $LiFePO_4$ have been adopted to improve the electronic and ionic conductivities.[35-37] Nevertheless, the relatively low operating voltage of 3.4 V vs. Li/Li^+ along with the low volumetric capacity reduce the energy density of the cell and hinder the use of $LiFePO_4$ for high energy applications.

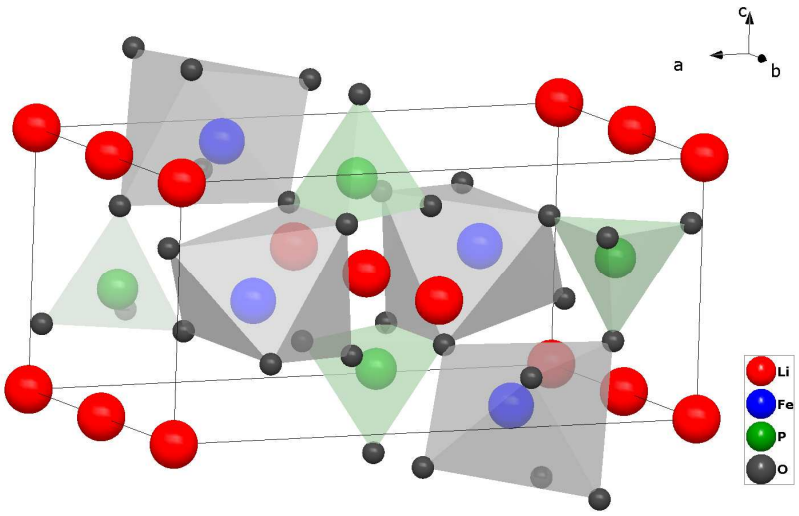

Figure 1.6. Crystal structure of olivine $LiFePO_4$.

1.1.3.4 High-capacity lithium-rich layered oxides

The high energy density of lithium-ion batteries has made them attractive both as a power source for the electric vehicles and as an energy storage device for renewable energy technologies because they offer much higher energy density compared to other rechargeable systems. However, the energy density of the present-day lithium-ion batteries is limited by the cathode capacity of < 200 mAh/g and an operating voltage of ~ 4 V. With an aim to increase the energy density further, there is immense interest in developing new cathode materials that operate at significantly higher voltages and/or with much higher capacities.[38] In this regard, solid solutions between layered $Li[Li_{1/3}Mn_{2/3}]O_2$ (commonly designated as Li_2MnO_3) and layered $Li[Mn_{1-y-z}Ni_yCo_z]O_2$ (designated as lithium-rich layered oxides $Li[Li,Mn,Ni,Co]O_2$) have become appealing as they offer much higher capacities of above 250 mAh/g at a lower cost and better safety compared to $LiCoO_2$.[39-44] The high-capacity of these lithium-rich layered oxides is ascribed to the irreversible loss of oxygen from the lattice during the first charge, followed by a lowering of the oxidation state of the transition-metal ions at the end of first discharge.[44]

As shown in Figure 1.7, $Li[Li_{1/3}Mn_{2/3}]O_2$ has the layered rocksalt structure similar to $LiCoO_2$; however, 1/3 of the transition metal layer is occupied by Li^+ ions. Due to the ordering of the Li^+ and Mn^{4+} ions in the transition metal layer, the symmetry of $Li[Li_{1/3}Mn_{2/3}]O_2$ is reduced from *R3-m* to *C2/m*, as revealed by the existence of the superstructure reflections appearing in the XRD patterns. Solid solutions between $Li[Li_{1/3}Mn_{2/3}]O_2$ and $Li[Mn_{1-y-z}Ni_yCo_z]O_2$ are possible due to the structural compatibility. Although electrochemical and structural properties of $Li[Li,Mn,Ni,Co]O_2$ show characteristics of solid solution on a macroscopic scale, some studies have

reported that both $Li[Li_{1/3}Mn_{2/3}]O_2$ and $Li[Mn_{1-y-z}Ni_yCo_z]O_2$ nanodomains exist in the structure.[45, 46] However, this is controversial and single phase vs. two-phase mixture may depend on the composition and synthesis methods.

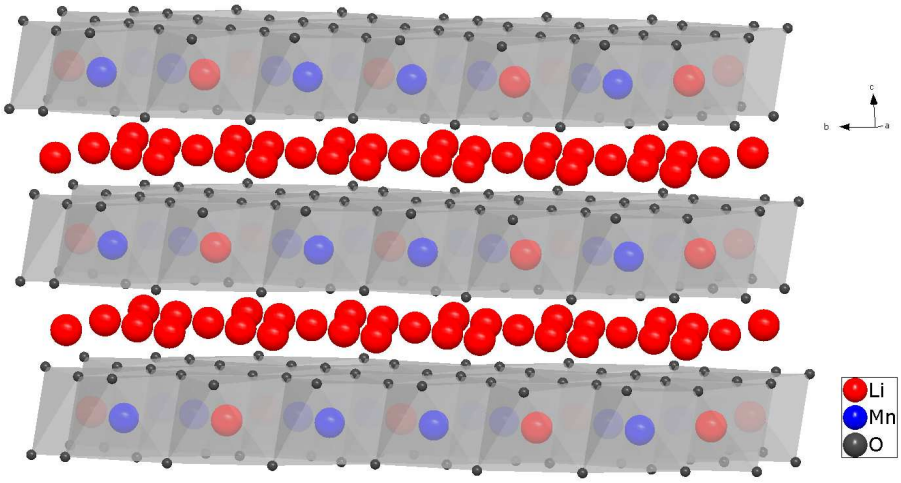

Figure 1.7. Crystal structure of $Li[Li_{1/3}Mn_{2/3}]O_2$.

The major issues with these lithium-rich layered oxide cathodes are huge irreversible capacity loss (C_{irr}) in the first cycle, electrolyte instability at the high operating voltage of up to 4.8, low rate capability, low tap density leading to low volumetric energy density, and decline in cell voltage during cycling. The inferior rate capability originates from defects formed by the release of oxygen from the lattice and the thick solid-electrolyte interphase (SEI) layer formation due to the high operating voltage (~ 4.8 V).[47] Additionally, the huge irreversible capacity loss is attributed to the elimination of oxide-ion vacancies and lithium sites at the end of the first charge and the subsequent inability to reinsert all of the lithium ions back into the layered oxide

lattice.[44, 48, 49] The voltage decay originates from the gradual phase transformation of the layered phase to a spinel-like phase.[50]

To overcome these drawbacks and improve the electrochemical performance of lithium-rich layered oxide cathodes, various strategies have been pursued. Surface coating with other materials such as Al_2O_3, $AlPO_4$, RuO_2, $LiNiPO_4$, C, and Al have been found to reduce the C_{irr} and increase the rate capability significantly, as the surface coating helps retain oxide-ion vacancies and lithium sites in the layered lattice after the first charge.[48, 49, 51-54] Similarly, surface treatment with mild acids has also been reported to reduce the C_{irr}.[55, 56] Aside from surface modification strategies, blending the lithium-rich layered oxide with other lithium-free insertion hosts such as V_2O_5, LiV_3O_8, and $Li_4Mn_5O_{12}$ has also been found as an effective method for eliminating the C_{irr}.[57, 58] The lithium-free insertion hosts provide the lithium sites for inserting the lithium ions that could not be inserted back into the layered oxide lattice. Recently, a completely new approach has been reported wherein electrochemical pre-treatment has also been shown to improve the cyclability of the lithium-rich layered oxides without any chemical processing.[59-61]

1.1.3.5 High-voltage spinel oxide

Originally, substitution of manganese ions in $LiMn_{2-x}M_xO_4$ (M = Cr^{3+}, Co^{3+}, Ni^{2+}, and Cu^{2+}) by other transition metal ions has been studied to improve the electrochemical performance of $LiMn_2O_4$ by increasing the average oxidation state of the manganese ion. Unexpectedly, cation substituted $LiMn_{2-x}M_xO_4$ (M = Cr^{3+}, Co^{3+}, Ni^{2+}, and Cu^{2+}) exhibited a plateau around 5 V in addition to the 4 V plateau.[32, 62] Both plateaus at 5 and 4 V correspond to lithium ion insertion into the 8a tetrahedral sites of the cubic spinel

structure. The 5 V plateau is attributed to the redox reaction of $M^{3+/4+}$ or $M^{2+/4+}$ through M^{3+}, while the plateau at 4 V originates from the redox reaction of $Mn^{3+/4+}$.

Among the cation substituted $LiMn_{2-x}M_xO_4$ (M = Cr^{3+}, Co^{3+}, $Ni^{2+}$and Cu^{2+}), $LiMn_{1.5}Ni_{0.5}O_4$ spinel is a promising cathode material because the presence of most of the manganese ions in the 4+ state during the high-voltage operation (> 3 V) suppresses both Jahn-Teller distortion and Mn dissolution.[32, 62-64] Due to the large ionic size difference between Mn^{4+} and Ni^{2+} and divalent oxidation state of Ni^{2+}, $LiMn_{1.5}Ni_{0.5}O_4$ spinel can have two different crystallographic structures depending on the preparation method: samples synthesized at high temperatures (>700 ^oC) with rapid cooling display the disordered phase with the space group *F*d-3*m*, while slow cooling and post annealing at 700 ^oC stabilizes the ordered phase (3:1 ordering of Mn^{4+} and Ni^{2+} ions in the 12d and 4b octahedral sites, respectively) belonging to the space group $P4_332$ as shown in Figure 1.8.[64-69] The challenges for the $LiMn_{1.5}Ni_{0.5}O_4$ spinel are the formation of $Li_xNi_{1-x}O$[31, 32, 70] impurity phase during the synthesis and capacity fade during cycling. It is believed that the capacity fade originates from the large lattice strain during the lithium ion insertion and the corrosion reactions between the electrolyte and cathode surface due to the higher operating voltage of 4.7 V.[71] It has been reported that partial substitutions of Mn and Ni by other cations such as Cr, Fe, Co, Zn, and Ga can suppress the formation of the impurity phases and improve cyclability.[72, 73] The improvement in cyclability with cation substitution was attributed to the smaller lattice strain during cycling and the stabilization of disordered phase.[71] It has also been found that surface modification can improve the electrochemical performance of the $LiMn_{1.5}Ni_{0.5}O_4$ spinel by suppressing the corrosion reaction.[47, 73]

However, most studies are about the structural and electrochemical characterization of $LiMn_{1.5}Ni_{0.5}O_4$ at high-voltage operation (> 3.5 V). Only a few studies

have focused on the structural and electrochemical characterizations when both the 8a tetrahedral sites and 16c octahedral sites are used for lithium ion insertion/extraction (5.0 – 2.0 V).[67, 69] Accordingly, structural and electrochemical investigations of $LiMn_{1.5}Ni_{0.5}O_4$ spinel during operation between 5.0 and 2.0 V could lead to further understanding of this material.

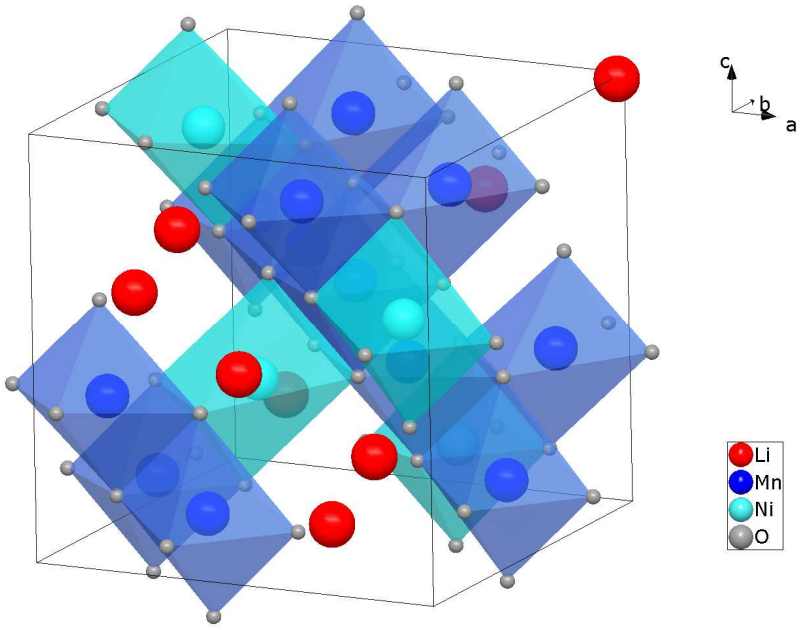

Figure 1.8. Crystal structure of the ordered spinel $LiMn_{1.5}Ni_{0.5}O_4$.

1.1.3.6 Layered-spinel composite oxide

As discussed earlier, high-capacity lithium-rich layered oxides $Li[Li,Mn,Ni,Co]O_2$ [solid solutions between layered $Li[Li_{1/3}Mn_{2/3}]O_2$ and $LiMO_2$ (M = Mn, Ni, and Co)] and high-voltage spinel oxides $LiMn_{1.5}Ni_{0.5}O_4$ have become attractive since they exhibit high energy density and high power density, respectively. One approach to realizing a combination of high energy and power density is to use a

composite that consists of the high-capacity lithium-rich layered oxide $Li[Li,Mn,Ni,Co]O_2$ and the high-voltage spinel oxide $LiMn_{1.5}Ni_{0.5}O_4$. The cubic-close packed oxygen arrays in both the layered and spinel oxides are structurally compatible.

Two layered-spinel composite systems have been investigated in the literature: $xLi_2MnO_3-(1-x)Li_{1+\delta}Mn_{2-\delta}O_4$ ($0 \leq \delta \leq 1/3$)[46, 74] and $x(Li_2MnO_3 \cdot Li[Mn_{0.5}Ni_{0.5}]O_2) - (1-x)Li[Mn_{1.5}Ni_{0.5}]O_4$ ($0 \leq x \leq 1$).[75-78] While the former system involves the 3 and 4 V spinels, the latter system involves the 5 V spinel. The performances of these layered-spinel composites exceed those of the individual layered or spinel oxides in terms of both specific capacity and cycle performance when cycled between 5 and 2 V at low current rates. In order to understand the structural complexity of the layered-spinel composite materials, various techniques such as XRD, X-ray absorption spectroscopy (XAS), and nuclear magnetic resonance (NMR) have been used both for the pristine state and during first cycle.[74, 76]

Although the electrochemical activities of the layered and spinel phases were confirmed with these techniques, the compositional variations of the layered and spinel phases in the composite sample were not available; because of the same basic cubic close packed oxygen array, the actual composition and content of the layered and spinel phases in the composite could be different from the nominal composition and content. In addition, previous studies have focused on the structural and electrochemical characteristics of the composite cathodes in the pristine state or during the first cycle. However, limited information is available on the structural and electrochemical characteristics during the extended cycling of these composite cathodes. In fact, these composite cathodes show a gradual increase in discharge capacity that is accompanied by significant changes in the charge/discharge profiles during extended electrochemical cycling, which is different from what is observed with either of the individual phases.

Accordingly, an investigation of the effect of synthesis condition on the compositional, structural, and electrochemical characteristics in the pristine state and during cycling of the layered-spinel composite oxides could lead to further understanding of these materials.

1.1.4 Anode materials

Due to the safety problem of the lithium metal, most commercial lithium ion batteries have used graphite as an anode material since their commercialization. Graphite has advantages such as long cycle life, abundance, and low cost. However, the low energy density and safety issues related to lithium plating on graphite have prompted further research for alternative anode materials with enhanced safety and high energy density.[79] The major anode materials are compared in Table 1.2.

Alloy anodes are the most promising anode materials for high energy density because the theoretical capacities of alloy anodes are 2 – 10 times higher than that of graphite. In addition, the operating voltages of some of the alloy anodes are 0.3 – 0.4 V higher than Li/Li^+. Higher operating voltage can mitigate both SEI layer formation and lithium plating. However, large volume change (100 – 300 %) during lithiation and delithiation reactions is the main challenge in the commercialization of alloy anodes. Their large volume changes lead to pulverization of active materials, which results in poor cycle life.[80, 81] Another challenge of alloy anodes is large first-cycle irreversible capacity loss. To overcome these two challenges, extensive research has been performed.[80-83] Sony successfully commercialized a new lithium ion battery, "Nexelion," with an amorphous tin-cobalt-carbon anode in 2005.[84] Recently, crystallographically aligned silicon nanowires have been found to exhibit enhanced cycle performance by mitigating the large volume change.[85] Dispersing silicon nanoparticles in the

electronically conductive binder has also improved the cycle performance by accommodating the volume change and retaining electronic conductivity.[86]

$Li_4Ti_5O_{12}$ spinel is another promising anode material especially for high power and long cycle life applications.[87-89] Because it exhibits high rate capability due to the three-dimensional diffusional path of lithium ions in the cubic spinel structure while operating at a high voltage of ~ 1.5 Vvs.Li/Li^+, lithium plating and SEI layer formation problems during operation are eliminated. Excellent cycle performance originates from the very small volume change (< 0.1 %) during the lithiation and delithiation reactions. However, the limited theoretical capacity of 175 mAh/g at a flat operating voltage of 1.5 V vs.Li/Li^+ significantly reduces the energy density of the cell and hinders the use of $Li_4Ti_5O_{12}$ spinel for high energy applications.

Table 1.2 Comparison of anode materials.[90]

Anode material	Lithiated phase	Theoretical capacity (mAh/g)	Volume change (%)
Li	Li	3862	100
Graphite	LiC_6	372	12
$Li_4Ti_5O_{12}$	$Li_7Ti_5O_{12}$	175	1
Si	$Li_{4.4}Si$	4200	320
Sn	$Li_{4.4}Sn$	994	260
Sb	Li_3Sb	660	200
Al	LiAl	993	96

1.1.5 Electrolytes

Electrolytes in lithium ion battery do not participate in redox reactions and serve only as a pathway for the lithium ions, which is different from other rechargeable system. Lithium ion batteries have used non-aqueous electrolytes since the operating voltage of lithium ion batteries is much higher (> 4 V) than the voltage window of aqueous electrolytes (~ 1.23 V). In addition to the wide voltage window (> 4 V), electrolytes should satisfy the following requirements:[2]

- High lithium-ion conductivity (>10^{-4} S/cm) in the battery operating temperature range
- Low electronic conductivity (<10^{-10} S/cm)
- Thermal and chemical stability in the battery operating and storage environments
- Chemical stability in contact with other cell components
- Non-toxic and low cost

Ethylene carbonate (EC) mixed with dimethyl carbonate (DMC) or diethyl carbonate (DEC) are widely used as the solvent for the electrolyte in lithium ion batteries. EC forms a stable passivating solid electrolyte layer on the surface of a graphite anode. For the lithium salt, $LiPF_6$ is most commonly used in lithium ion batteries because it shows high ionic conductivity in carbonate-based solvents. However, carbonate-based electrolytes are flammable, and undergo oxidation above 4.7 V. To overcome these drawbacks various alternative electrolytes such as ionic liquids,[91] solid polymer electrolytes,[92] inorganic solid electrolytes,[93] and hybrid electrolytes[94] have been investigated for next generation electrolytes.

1.1.6 Separators

Separators in lithium ion batteries do not participate in charge/discharge reactions but serve both as an electronic insulator and as lithium ion pathways between cathode and anode. Most commercial lithium ion batteries use polyethylene (PE) or polypropylene (PP) films as a separator due to the advantages such as good mechanical properties and chemical stability. Recently, ceramic-coated PE and PP separators are being used for high-capacity cells for vehicle applications to improve the safety.

1.2 OBJECTIVE

The primary objective of my dissertation is to develop a firm understanding of the unique structural and electrochemical characteristics of the layered-spinel composite oxide cathodes along with their component phases, the high-capacity lithium-rich layered oxide $Li[Li,Mn,Ni,Co]O_2$ and the high-voltage spinel oxide $LiMn_{1.5}Ni_{0.5}O_4$. To accomplish this, the structural and electrochemical characterizations of the high-voltage spinel $LiMn_{1.5}Ni_{0.5}O_4$ samples with different degrees of transition metal ordering during operation between 5.0 and 2.0 V are systematically carried out and presented in Chapter 3 by an analysis of *ex-situ* XRD including synchrotron data of the pristine samples and various electrochemical measurements. With the obtained understandings in Chapter 3, the effect of doping on the cation ordering and the charge-discharge behavior of $LiMn_{1.5}Ni_{0.5-x}M_xO_4$ (M = Cr, Fe, Co, and Ga) spinel between 5.0 and 2.0 V are studied in Chapter 4.

In Chapter 5, the compositional and wt. % variations of the layered and spinel phases from the nominal values in the layered-spinel system $xLi[Li_{0.2}Mn_{0.6}Ni_{0.17}Co_{0.03}]O_2 - (1-x)Li[Mn_{1.5}Ni_{0.425}Co_{0.075}]O_4$ ($0 \leq x \leq 1$) are obtained by employing a joint XRD and

neutron diffraction (ND) Rietveld refinement method. Based on the obtained composition and *ex-situ* XRD data, the mechanism for the increase in capacity and the facile phase transformation of the layered phase in the composite cathodes to a cubic spinel phase during extended electrochemical cycling are proposed.

In Chapter 6, the effect of synthesis temperature on the structural and electrochemical characteristics of the layered-spinel composite system xLi[$Li_{0.2}Mn_{0.6}Ni_{0.2}$]O_2–(1-x)Li[$Mn_{1.5}Ni_{0.5}$]O_4 ($0 \leq x \leq 1$) is presented by employing XRD, ND, and electrochemical analysis with the obtained understandings in Chapters 3 – 5.

In addition, improving the electrochemical performance of the lithium-rich layered oxide Li[Li,Mn,Ni,Co]O_2 is pursued in Chapters 7 and 8 by blending with the lithium-free insertion host VO_2(B) and controlling the amount of lithium ions extracted from the layered lattice during the first charge process.

Chapter 2: General experimental procedures

2.1 MATERIAL SYNTHESIS

All the high-capacity lithium-rich layered oxide, high-voltage spinel oxide, and layered-spinel composite oxide cathodes were synthesized by heating a required amount of mixed metal hydroxides with lithium hydroxide at various temperature (700 - 900 ^{o}C) in air. The mixed metal hydroxides were obtained by a co-precipitation method, involving a drop wise addition of required amounts of the aqueous metal acetate solution into a 2 M KOH solution under continuous stirring. The co-precipitated mixed metal hydroxide powders were then washed with distilled water and dried in an air oven at 100 ^{o}C. The detailed synthesis procedures will be described in the respective chapters.

2.2 MATERIAL CHARACTERIZATION

The materials synthesized were characterized by the following techniques. The specific characterization procedures will be described in the respective chapters.

2.2.1 X-ray diffraction (XRD)

XRD data were collected with a Rigaku Ultima-IV system (Cu Kα radiation) and Philips X-ray diffractometer 3550 (Cu Kα radiation). Synchrotron XRD measurement were carried out with the beamline X14A by a linear position-sensitive silicon detector at the National Synchrotron Light Source (NSLS) at Brookhaven National Laboratory (λ = 0.77376 Å). The phase in the collected XRD data was identified with the JCPDS files by using the Rigaku PDXL commercial software.[95] Rietveld refinements with the Rigaku PDXL commercial software and the software package GSAS and the EXPGUI interface[96, 97] were used to characterize the detailed structures.

2.2.2 Neutron diffraction (ND)

ND measurements were carried out with the general purpose powder diffraction beamline POWGEN at the Spallation Neutron Source.[98] The samples were loaded in Vanadium cans and the 24 sample changer was used to collect the room-temperature patterns at wavelengths of 1.066 and 2.665 Å, which cover a d spacing range of 0.3 to 6.2 Å. Rietveld refinements with the software package GSAS and the EXPGUI interface[98, 99] were used to characterize the detailed structures.

2.2.3 Inductively coupled plasma – atomic emission spectrometer (ICP-AES)

The Li, Mn, Ni, and Co molar ratios in the synthesized samples were analyzed with a Varian 715-ES inductively coupled plasma – atomic emission spectrometer (ICP-AES). The samples were first dissolved in concentrated acid (HCl : HNO_3 = 3 : 1) for complete dissolution. The dissolved solutions were diluted with the deionized water to match the concentration ranges of standard solutions. The instrument was calibrated with four different concentrations of standard solutions for each element.

2.2.4 Scanning electron microscopy (SEM) and Transmission electron microscopy (TEM)

The morphology of the synthesized samples was investigated with a JEOL LSM-5610 scanning electron microscope and JEOL 2010F high-resolution transmission electron microscope.

2.2.5 Surface area measurement

Multi-point Brunauer−Emmett−Teller (BET) surface area data of the samples were collected with an automatic nitrogen gas sorption analyzer (NOVA 2000, Quantachrome) using physical adsorption at 77 K.

2.2.6 Fourier transform infrared (FTIR) spectroscopy

Fourier transform infrared (FTIR) spectroscopy data were obtained with KBr pellets with a PerkinElmer IR spectrometer.

2.3 ELECTROCHEMICAL CHARACTERIZATION

2.3.1 Cell construction

Electrochemical properties of the synthesized samples were evaluated with 2032-type coin cells with lithium metal as a counter electrode. The cathodes consisted of a mixture of 80 wt. % active material, 10 wt. % Super P conductive carbon additive, and 10 wt. % polyvinylidene fluoride (PVDF) binder. Coin cells were assembled in an Ar-filled glove box with 1 M $LiPF_6$ in ethylene carbonate (EC)/ diethyl carbonate (DEC) (1:1 v/v) as the electrolyte and Celgard polypropylene as the separator.

2.3.2 Cycle performance and rate capability test

All electrochemical tests were performed with an Arbin battery cycler. Different voltage window and current rate were used depending on the samples. Cycle performances were evaluated by charging and discharging at a fixed current density in a fixed voltage window. Rate capabilities were evaluated by charging at a fixed current density and discharging at various C rates in the fixed voltage window.

Chapter 3: Influence of cation ordering and lattice distortion on the charge-discharge behavior of $LiMn_{1.5}Ni_{0.5}O_4$ spinel between 5 and 2 V

3.1 INTRODUCTION

Lithium-ion batteries are being employed as a power source for EVs and PHEVs. However, the limited energy density of lithium-ion batteries restricts the driving range, and it is one of the main obstacles of a widespread adoption of EVs and PHEVs in addition to the cost and safety concerns. The energy density of commercial lithium-ion batteries is mainly limited by the operating voltage and the capacity of the cathode material, so recent efforts are focused on new cathodes with a higher operating voltage or higher capacity.[38] In this regard, $LiMn_{1.5}Ni_{0.5}O_4$ spinel is a promising cathode material because it operates at a high voltage of ~ 4.7 V while exhibiting high rate capability due to the three-dimensional diffusional path of lithium ions in the cubic spinel structure.[32, 62] In addition, the presence of most of the manganese ions in the 4+ state during the high-voltage operation (> 3 V) suppresses both Jahn-Teller distortion and Mn dissolution.[63, 64] However, the limited capacity of ~ 140 mAh/g above 3 V hinders the use of $LiMn_{1.5}Ni_{0.5}O_4$ for high energy applications. Theoretically, $LiMn_{1.5}Ni_{0.5}O_4$ can exhibit a capacity of ~ 294 mAh/g when lithium ions are inserted/extracted into/from both 8a tetrahedral and 16c octahedral sites of the spinel lattice at the voltages of, respectively, ~ 4.7 and ~ 2.7 V.[67]

As mentioned in section 1.1.3.5 of Introduction, it is known that $LiMn_{1.5}Ni_{0.5}O_4$ can have two different crystallographic structures depending on the preparation method: samples synthesized at high temperatures with rapid cooling display the disordered phase with the space group *F*d-3*m*, while slow cooling and post annealing at 700 ^oC stabilizes the ordered phase (3:1 ordering of Mn^{4+} and Ni^{2+} ions in the 12d and 4b octahedral sites,

respectively) belonging to the space group $P4_332$.[64-69] Despite many reports about the transition metal ordering effect on the structural transitions and electrochemical performance of $LiMn_{1.5}Ni_{0.5}O_4$ at high voltages (> 3.5 V),[64, 99-104] only a few studies have focused on the structural and electrochemical characterizations when both the 8a tetrahedral sites and 16c octahedral sites are used for lithium ion insertion/extraction (5.0 – 2.0 V).[67, 69]

Accordingly, we present here the structural and electrochemical characterization of the $LiMn_{1.5}Ni_{0.5}O_4$ samples with different degrees of transition metal ordering during operation between 5.0 and 2.0 V. We synthesized four different samples by controlling the cooling rate and applying different post-annealing conditions. The effects of transition metal ordering on the electrochemical performance in the wide operating voltage of 5.0 – 2.0 V are investigated by a careful analysis of *ex-situ* XRD including synchrotron data of the pristine samples and various electrochemical measurements.

3.2 EXPERIMENTAL

3.2.1 Synthesis

The mixed metal hydroxide precursor $Mn_{0.75}Ni_{0.25}(OH)_2$ was obtained via a co-precipitation method as described in Chapter 2. The four different $LiMn_{1.5}Ni_{0.5}O_4$ samples were prepared by controlling the heat treatment condition of the hydroxide mixtures of $Mn_{0.75}Ni_{0.25}(OH)_2$ and LiOH. The first $LiMn_{1.5}Ni_{0.5}O_4$ sample was obtained by heating the hydroxide mixture at 900 ^oC for 12 h in air with a 5 ^oC/min cooling rate, which is hereafter referred to as highly disordered spinel (HDS). The second $LiMn_{1.5}Ni_{0.5}O_4$ sample was obtained by heating the hydroxide mixture at 900 ^oC for 12 h in air with a 1 ^oC/min cooling rate, which is hereafter referred to as disordered spinel (DS). The third sample was obtained by post annealing the DS sample at 700 ^oC for 48 h

in air with a 1 ^{o}C/min cooling rate, which is hereafter referred to as annealed disordered spinel (ADS). The fourth sample was obtained by post annealing the DS sample at 700 ^{o}C for 96 h in air with a 1 ^{o}C/min cooling rate, which is hereafter referred to as highly ordered spinel (HOS).

3.2.2 Characterization

The Li, Mn, and Ni molar ratios in the synthesized samples were analyzed with a ICP-AES analysis. XRD data were collected with a Rigaku Ultima-IV system (Cu Kα radiation). Synchrotron XRD measurement were carried out with the beamline X14A by a linear position-sensitive silicon detector at the National Synchrotron Light Source (NSLS) at Brookhaven National Laboratory (λ = 0.77376 Å). For the *ex-situ* XRD analysis, coin cells were disassembled in an Ar-filled glove box just after the intended state of charge was reached. The cathode materials were gently washed with diethyl carbonate (DEC), dried at room temperature, and finally attached to a Kapton film in order to minimize contact with air. XRD Rietveld refinements with the software package GSAS and the EXPGUI interface[98, 99] were used to characterize the pristine samples. The lattice parameters of each phase in the *ex-situ* samples were obtained by the Rietveld refinement with Rigaku PDXL commercial software. Fourier transform infrared spectroscopy (FTIR) data were obtained with KBr pellets.

Electrochemical properties of the $LiMn_{1.5}Ni_{0.5}O_4$ cathodes were evaluated with 2032-type coin cells. The coin cells were assembled as described in Chapter 2.

3.3 RESULTS AND DISCUSSION

3.3.1 Chemical and structural analysis

ICP-AES analysis of the metal ion contents in the four $LiMn_{1.5}Ni_{0.5}O_4$ samples indicates that the contents are close to the nominal composition; the presence of small amounts of $Li_xNi_{1-x}O$ or Ni_6MnO_8 impurity phases (see later) makes precise analysis of the metal contents in the spinel phase difficult. The FTIR spectra of the four pristine $LiMn_{1.5}Ni_{0.5}O_4$ samples are shown in Figure 3.1. The ordering in 16d octahedral sites can be qualitatively determined by the intensity ratio between the peaks at 590 and 621 cm^{-1}.[104] Specifically, the intensity of the 590 cm^{-1} Ni-O band increases compared to that of 621 cm^{-1} Mn-O band as the degree of ordering in the 16d sites increases. As we can see in Figure 3.1, the relative intensity of the 590 cm^{-1} Ni-O band gradually increases with a slower cooling rate and longer post annealing time, indicating an increase in the degree of cation ordering in the 16d octahedral sites.

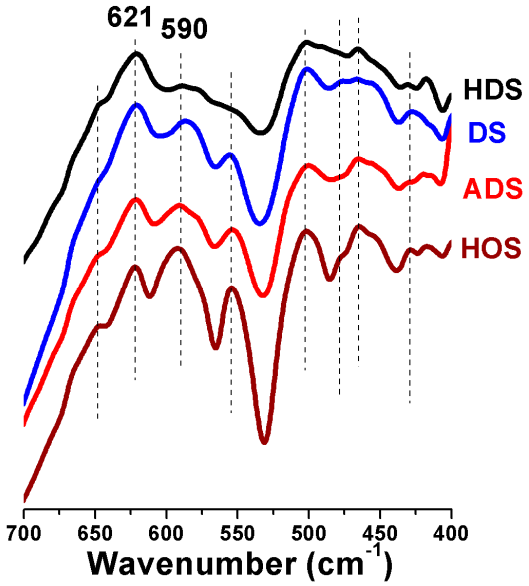

Figure 3.1. Infrared spectra of the four pristine $LiMn_{1.5}Ni_{0.5}O_4$ samples.

The XRD patterns of the four pristine $LiMn_{1.5}Ni_{0.5}O_4$ samples are shown in Figure 3.2. The XRD patterns of three of the samples (HDS, DS, and ADS) fit well to the space group *F*d-3*m*. The absence of any superstructure reflections, which originates from the ordering of Mn^{4+} and Ni^{2+} ions in the 16d octahedral sites, reveals that these three $LiMn_{1.5}Ni_{0.5}O_4$ samples have a disordered spinel structure without any long-range ordering. However, annealing at 700°C for 96 h in air changes the structure of the DS sample to the highly ordered spinel phase (HOS) with the space group $P4_332$, as revealed by the existence of superstructure reflections in the XRD pattern.[104-106] The weak reflections possibly from a $Li_xNi_{1-x}O$[31, 32, 70] or Ni_6MnO_8[107] impurity phase are observed in all four samples, but the relative intensity of the impurity phase is much lower in the HOS sample.

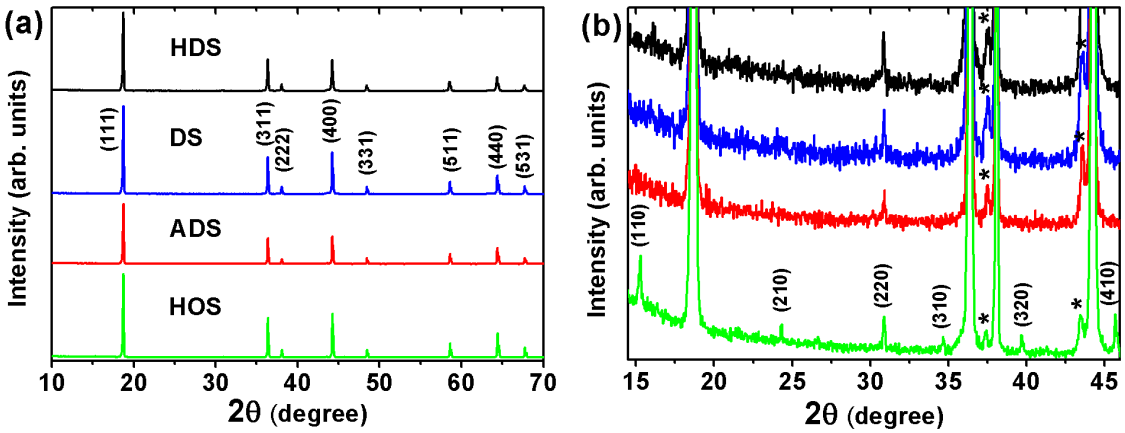

Figure 3.2. XRD patterns of the four pristine $LiMn_{1.5}Ni_{0.5}O_4$ samples: (a) full range and (b) enlarged region to show the superstructure reflections arising from the Mn^{4+} and Ni^{2+} ordering in the 16d octahedral sites. Asterisks refer to the reflections arising from $Li_xNi_{1-x}O$ or Ni_6MnO_8 impurity phases.

To identify the structure of the four pristine $LiMn_{1.5}Ni_{0.5}O_4$ samples, Rietveld refinements were performed with the synchrotron XRD data and the results are shown in Table 3.1. The Rietveld refinement results of the representative disordered (HDS) and ordered (HOS) spinel samples are shown in Figure 3.3. The weight percentages of the impurity phase in the samples are also given in Table 3.1. The weight percentage of the impurity phase decreases gradually with decreasing cooling rate and longer post annealing time as expected from Figure 3.2. As seen in Table 3.1, the lattice constant decreases with a slower cooling rate and longer post annealing time due to both an oxidation of the larger Mn^{3+} ions into the smaller Mn^{4+} ions and an optimization of the space occupation in the lattice through the increased degree of ordering in the 16d sites. In the ordered spinel phase ($P4_332$), the larger Ni^{2+} ions and the smaller Mn^{4+} ions occupy, respectively, the larger 4b sites and smaller 12d sites, which results in a reduced lattice volume.[66] Therefore, ordering in the 16d sites could relax the lattice strain in $LiMn_{1.5}Ni_{0.5}O_4$.[66]

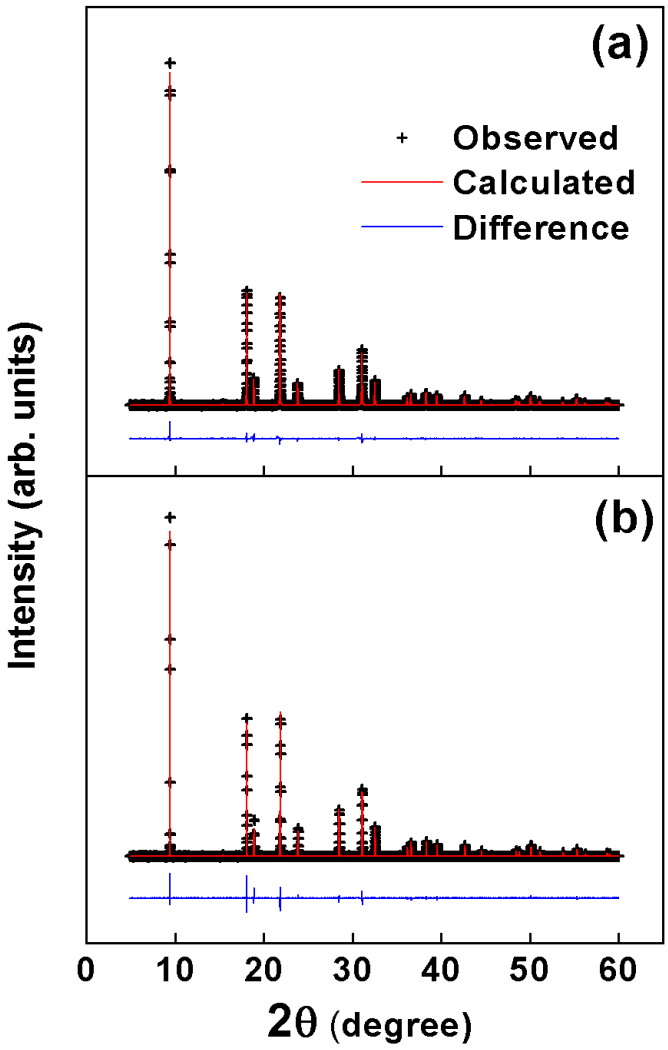

Figure 3.3. Synchrotron XRD Rietveld refinement results of the (a) HDS sample and (b) HOS sample.

Table 3.1 Structural parameters of the pristine $LiMn_{1.5}Ni_{0.5}O_4$ samples by synchrotron XRD Rietveld refinements.

Sample	*a* (Å)	Atom	Wyckoff position	*x*	*y*	*z*	Occupancy	U_{iso} ($Å^2 \times 10^2$)	R_p (%)	R_{wp} (%)	Weight percent of impurity (wt. %)
HDS (*Fd*-3*m*)	8.1858(2)	Li	8a	1/8	1/8	1/8	1	0.8	5.7	7.3	2.90
		Mn	16d	1/2	1/2	1/2	0.75	0.646(13)			
		Ni	16d	1/2	1/2	1/2	0.25	0.646(13)			
		O	32e	0.2622(1)	0.2622(1)	0.2622(1)	0.934(4)	1.017(27)			
DS (*Fd*-3*m*)	8.1790(1)	Li	8a	1/8	1/8	1/8	1	1.5	6.2	7.6	2.72
		Mn	16d	1/2	1/2	1/2	0.75	0.948(14)			
		Ni	16d	1/2	1/2	1/2	0.25	0.948(14)			
		O	32e	0.2640(1)	0.2640(1)	0.2640(1)	0.942(4)	1.204(66)			
ADS (*Fd*-3*m*)	8.1780(1)	Li	8a	1/8	1/8	1/8	1	0.55	8.2	10.5	2.29
		Mn	16d	1/2	1/2	1/2	0.75	0.853(14)			
		Ni	16d	1/2	1/2	1/2	0.25	0.853(14)			
		O	32e	0.2647(1)	0.2647(1)	0.2647(1)	0.947(4)	1.241(16)			
HOS ($P4_332$)	8.1731(1)	Li	8c	0.003	0.003	0.003	1	0.8	9.3	12.7	0.49
		Ni1	4b	5/8	5/8	5/8	0.691(15)	0.502(11)			
		Mn1	4b	5/8	5/8	5/8	0.309(15)	0.502(11)			
		Mn2	12d	1/8	0.3790(17)	-0.1291(2)	0.897(6)	0.618(25)			
		Ni2	12d	1/8	0.3790(17)	-0.1291(2)	0.103(6)	0.618(25)			
		O1	8c	0.3862(7)	0.3862(7)	0.3862(7)	1	0.9			
		O2	24e	0.1479(6)	-0.1428(6)	0.1281(5)	1	1.11			

The variations of the microstrain in the four pristine $LiMn_{1.5}Ni_{0.5}O_4$ samples are compared in the Williamson-Hall plot[108] in Figure 3.4. The Williamson-Hall method considers the combined effect of microstrain and crystallite size on the broadening of peaks in XRD. Combining Scherrer's equation for the crystallite size and Bragg's law for the microstrain yields the following relation:

$$B \cos\theta = K\lambda / t + k\varepsilon \sin\theta \qquad (1)$$

where B is the full width at half maximum (FWHM), θ is a diffraction angle, K is a constant, λ is the wavelength of the incident X-ray, t is the crystallite size, k is a constant, and ε is the microstrain. Using the Williamson-Hall plot, the microstrain can be extracted from the slope $k\varepsilon$. The instrumental broadening effect was not calibrated because the purpose of this Williamson-Hall plot is to understand the qualitative differences in microstrain between the samples. As seen in Figure 3.4, the slope decreases gradually with slower cooling rate and longer post annealing time due to increased ordering in the 16d sites.

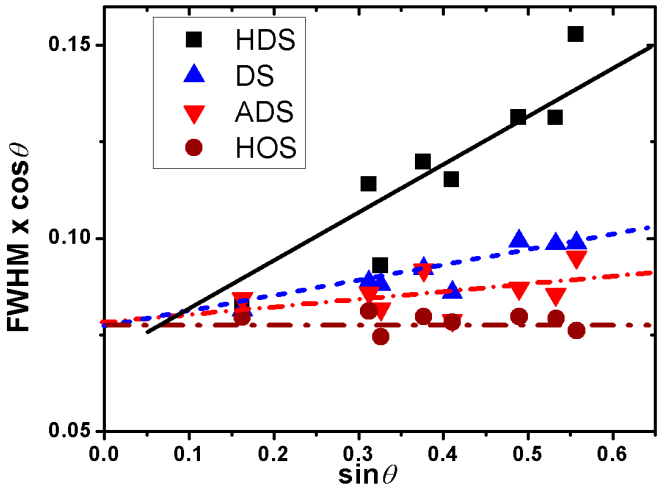

Figure 3.4. Williamson-Hall plot based on the XRD patterns of the four pristine $LiMn_{1.5}Ni_{0.5}O_4$ samples, revealing the lattice strain.

From the infrared spectroscopy data, refined lattice constants, existence of superstructure reflections, and appearance of microstrain variation, it is confirmed that slow cooling rates and post annealing processes increase the degree of ordering in the sample as reported in the literature.[64, 67, 69, 103]

3.3.2 First discharge and second charge profiles at 5.0 – 2.0 V

The first discharge and second charge profiles of the four different $LiMn_{1.5}Ni_{0.5}O_4$ samples at a current density of 10 mA/g are shown in Figure 3.5. All four samples were first charged to 5.0 V from the OCV state at a current density of 10 mA/g before discharging. As previously reported, all samples show five distinctive plateaus during discharge to 2 V.[67, 69] The two plateaus at ~ 4.7 V and one plateau at ~ 4 V correspond to lithium ion insertion into the 8a tetrahedral sites of the cubic spinel structure. The upper plateau and lower plateau at ~ 4.7 V are attributed to the reduction of, respectively, Ni^{4+} to Ni^{3+} and Ni^{3+} to Ni^{2+}.[103, 109] The plateau at ~ 4.0 V originates from the reduction of Mn^{4+} to Mn^{3+} involving the insertion of lithium ions into 8a tetrahedral sites due to the presence of a small amount of Mn^{3+} in the pristine samples.[32, 104] During discharge, both the voltage gap between the two plateaus at ~ 4.7 V and the plateau length at ~ 4.0 V decrease with a slow cooling rate and longer post annealing time due to the increase in the degree of cation ordering in the spinel phase.[103] The two plateaus (~ 2.7 and ~ 2.1 V) below 3 V are attributed to the reduction of Mn^{4+} to Mn^{3+} involving lithium ion insertion into 16c octahedral sites of the spinel structure, which is associated with a cubic to tetragonal phase transition.[67-69, 110] It should be noted that the appearance of two plateaus (~ 2.7 and ~ 2.1 V) corresponding to the lithium ion insertion into 16c octahedral sites is not an expected result because only one plateau at ~ 2.86 V is observed in the case of $LiMn_2O_4$.[24] The two plateaus at ~2.7 and ~2.1 V have also been observed in previous

work by Ariyoshi and Park,[67, 68] but the reason for the appearance of these two distinct plateaus was not provided. The structural changes associated with the two voltage plateaus at ~ 2.7 and ~ 2.1 V will be discussed in a later section detailing the *ex-situ* XRD and open-circuit voltage (OCV) data. All the samples display similar capacity values below 3 V even though the individual capacity values at the ~ 2.7 and 2.1 V plateaus vary. Interestingly, the capacity of the ~ 2.1 V plateau decreases while that of the ~ 2.7 V plateau increases with an increasing degree of cation ordering. The first discharge capacities are compared in Table 3.2.

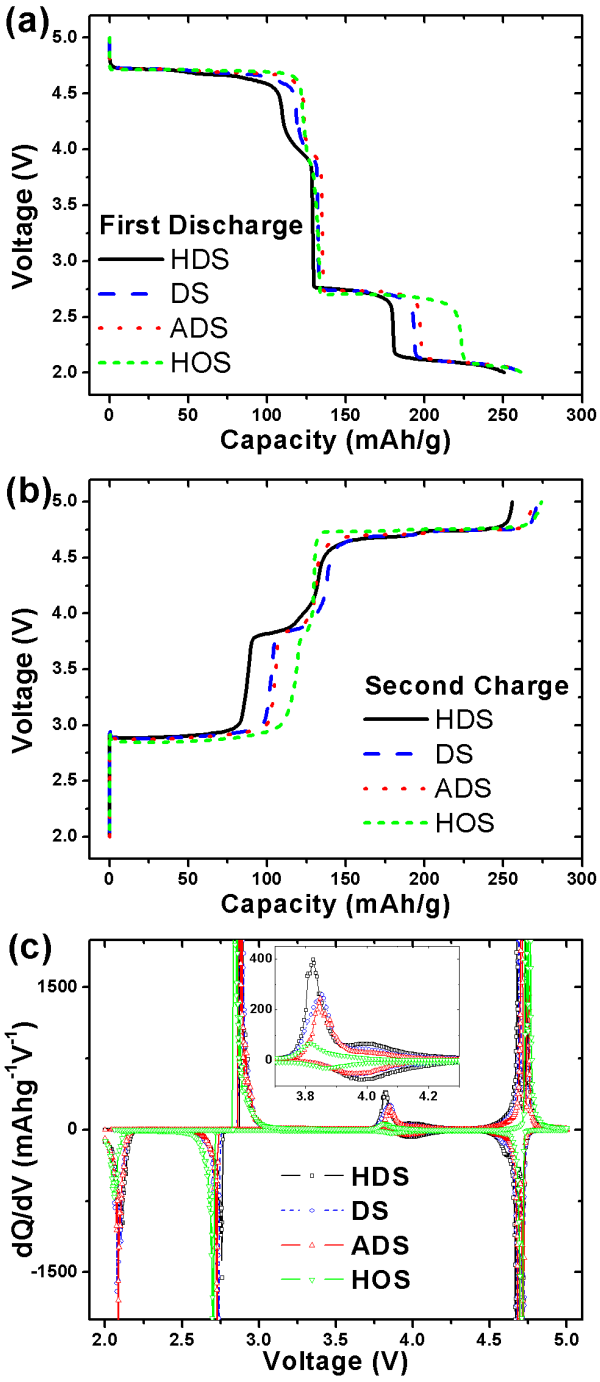

Figure 3.5. (a) first discharge profiles, (b) second charge profiles, and (c) differential capacity (dQ/dV) plots of the four $LiMn_{1.5}Ni_{0.5}O_4$ samples when cycled between 5 and 2 V at 10 mA/g.

Table 3.2 First discharge and second charge capacities of the $LiMn_{1.5}Ni_{0.5}O_4$ samples.

Sample	First discharge capacity (mAh/g)					Second charge capacity (mAh/g)					Voltage after all Li^+ removed from the16c octahedral site (V)
	Total	Capacity above 3 V	Capacity below 3 V			Total	Capacity above 3.95 V	Capacity below 3.95 V			
			Total	~ 2.7 V plateau	~ 2.1 V plateau			Total	~ 2.9 V plateau	~ 3.82 V plateau	
HDS	250.6	129.5	121.1	50.6	70.5	255.8	135.6	120.2	81.8	38.4	3.97
DS	261.9	132.7	129.2	60.6	68.6	271.8	142.3	129.5	97.9	31.6	3.95
ADS	262.3	135.4	126.9	62.0	64.9	268.5	142.9	125.6	99.3	26.3	3.98
HOS	262.2	133.1	129.1	89.3	39.8	274.2	146.1	128.1	109.2	18.9	4.05

To understand the relative capacity changes between the ~ 2.7 and ~ 2.1 V plateaus in different samples, we consider the structural differences between the disordered and ordered phases. As we discussed earlier, the microstrain can be relaxed with an increase in cation ordering. More importantly, there is difference between the size of the empty octahedral sites in the ordered and disordered phases. In the completely disordered phase (*F*d-3*m*), there is only one type of empty octahedral site (16c Wyckoff position), which is surrounded by six oxide ions in the 32e sites. On the other hand, there are two different types of empty octahedral sites (4a and 12d Wyckoff position) in the completely ordered phase ($P4_332$). The empty 4a site is surrounded by six oxide ions in the 24e sites, while the empty 12d site is surrounded by two oxide ions in the 8c sites and four oxide ions in the 24e sites. Using the refined structural data in Table 3.1, the sizes of the empty octahedral sites (distance between empty octahedral site and coordinated oxide ion) in the HDS and HOS samples were calculated with the DIAMOND program[111] and are listed in Table 3.3. For the 12d empty octahedral site of the HOS sample, the average distance between the octahedral site and the coordinated oxide ion was used. As seen in Table 3.3, the size of the empty 4a octahedral site (2.20 Å) in the ordered phase is larger than the sum of the ionic radii of the lithium and oxide ions (0.90 + 1.26 = 2.16 Å). In contrast, the empty 16c octahedral site in the disordered phase has a smaller size (2.15 Å) than the sum of the ionic radii of the lithium and oxide ions (2.16 Å). From the above analysis, we conclude that the longer ~ 2.7 V plateau displayed by the ordered sample is due to the larger empty octahedral sites (4a site) and the consequent little lattice distortion during lithium ion insertion into empty octahedral sites. On the other hand, the smaller ~ 2.7 V plateau and the longer ~ 2.1 V plateau displayed by the disordered sample is due to the smaller empty octahedral sites (16c site) compared to the size of lithium ions and the

consequent lattice distortion when lithium ions are inserted into the empty octahedral sites.

Table 3.3 Structural parameters of empty octahedral sites in the $LiMn_{1.5}Ni_{0.5}O_4$ samples.

Sample	Lattice constant (Å)	Distance between empty octahedral site and coordinated oxygen		
		16c – O (Å)	4a – O (Å)	12d – O (Å)
HDS	8.1858(2)	2.15		
HOS	8.1731(1)		2.20	< 2.15 >

During second charge, the cell voltage abruptly increases from 2.0 to ~ 2.9 V with an initial voltage overshoot. This noticeable difference between the charge and discharge voltages and the presence of a voltage overshoot are characteristics of two-phase reactions.[24, 67] After a long plateau at ~ 2.9 V, a relatively short plateau at ~ 3.82 V (new peak at ~ 3.82 V in Figure 3.5(C)) is observed that was not seen in the first discharge. Interestingly, the capacity from the ~ 3.82 V plateau decreases and that of the ~ 2.9 V plateau increases as the cation ordering increases. The variations in the capacity at ~ 2.9 and ~ 3.82 V during the second charge are summarized in Table 3.2. If an assumption is made that all lithium ions inserted into the 16c octahedral sites during discharge can be removed during the charge process, we can locate the voltage at which all lithium ions have been removed from the 16c octahedral sites. These voltage values are ~ 4 V in all samples as tabulated in Table 3.2. From this analysis, we can expect that the ~ 3.82 V

plateau is associated with a tetragonal to cubic phase transition, which is also confirmed by the *ex-situ* XRD analysis that will be discussed later. The three remaining plateaus, one at ~ 4.0 V and two at ~ 4.7 V, originate from lithium ion removal from the 8a tetrahedral sites corresponding to the oxidation of Mn^{3+} to Mn^{4+} and Ni^{2+} to Ni^{4+}, respectively.

3.3.3 Open-circuit voltage (OCV) profiles

Ariyoshi et al.[67] reported that ordered $LiMn_{1.5}Ni_{0.5}O_4$ ($P4_332$) shows a flat OCV of ~ 2.8 V when lithium ions are inserted into the 16c octahedral sites even though there are two plateaus (~ 2.7 and ~ 2.1 V) under constant current conditions. To examine the effect of cation ordering on the OCV of $LiMn_{1.5}Ni_{0.5}O_4$, we compared the OCVs of the HDS and HOS samples. Both samples were intermittently charged and discharged at a current density of 10 mA/g. Two different conditions were used to measure the OCVs between 5.0 and 2.0 V. Above 4.3 V, the current was applied for 1 h and then the cell was allowed to rest for 5 h. Below 4.3 V, a longer rest period (11 h) was employed due to the longer relaxation time.[67] Figure 3.6 compares the measured OCVs with a voltage profile at constant current as a function of cumulative capacity for both the HDS and HOS samples. The capacity values obtained from the OCV plots are similar to those obtained from the constant-current plots for both the HDS and HOS samples as the $LiMn_{1.5}Ni_{0.5}O_4$ spinel has fast lithium-ion diffusion rate. We can refer to the measured OCVs as reversible potentials.[67, 112, 113] During the insertion/extraction of lithium ions into/from the 8a tetrahedral sites, the reversible potential of both samples are similar to the voltage under constant current. It is noted that the difference between the reversible potential and the constant current voltage profile are clearly seen during insertion/extraction of lithium ions into/from the 16c octahedral sites in both the samples. The HDS and HOS samples

show very flat reversible potentials at ~ 2.8 V upon lithium ion insertion or removal from the 16c octahedral sites. However, both the samples show two distinctive plateaus at ~ 2.7 and ~ 2.1 V (during discharge) and at ~ 2.9 and ~ 3.82 V (during charge) under constant current.

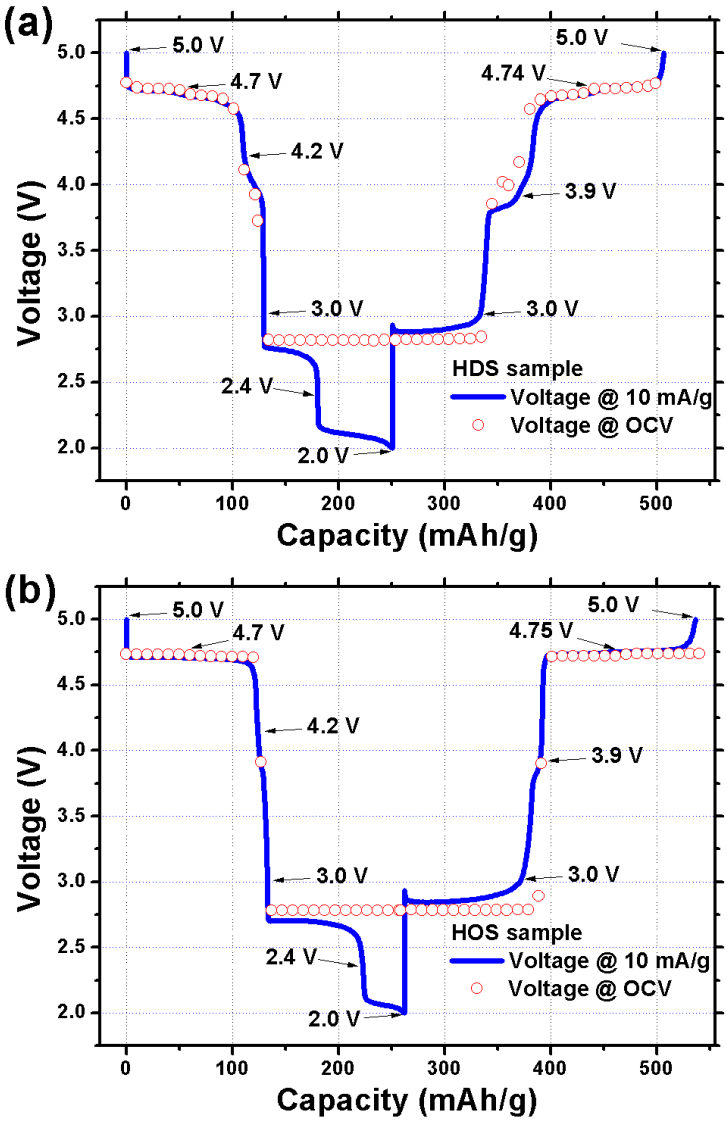

Figure 3.6. Comparison of the measured OCVs with a constant current voltage profile as a function of cumulative capacity: (a) HDS sample and (b) HOS sample.

To investigate the origin of the flat reversible potential at ~ 2.8 V, we carefully examined how the cell voltage changes throughout the OCV experiment. Selected segments of the voltage profiles of the HDS sample during the OCV experiment are shown in Figure 3.7. An ~ 2.1 V plateau (during discharge) and an ~ 3.82 V plateau (during charge) are observed when the current is applied. However, the voltages slowly increase from 2.1 to 2.82 V in Figure 3.7(a) and decrease from 3.82 to 2.82 V in Figure 3.7(b) during the rest period. This suggests that the flat reversible potential at ~ 2.8 V seen in the OCV experiment is not due to the absence of voltage splitting, but due to the change in voltage during the rest period. To examine why the voltage splits into two plateaus at ~ 2.7 and ~ 2.1 V during lithium ion insertion into 16c octahedral sites, *ex-situ* XRD data were collected for the HDS and HOS samples, and the results are discussed in the following section.

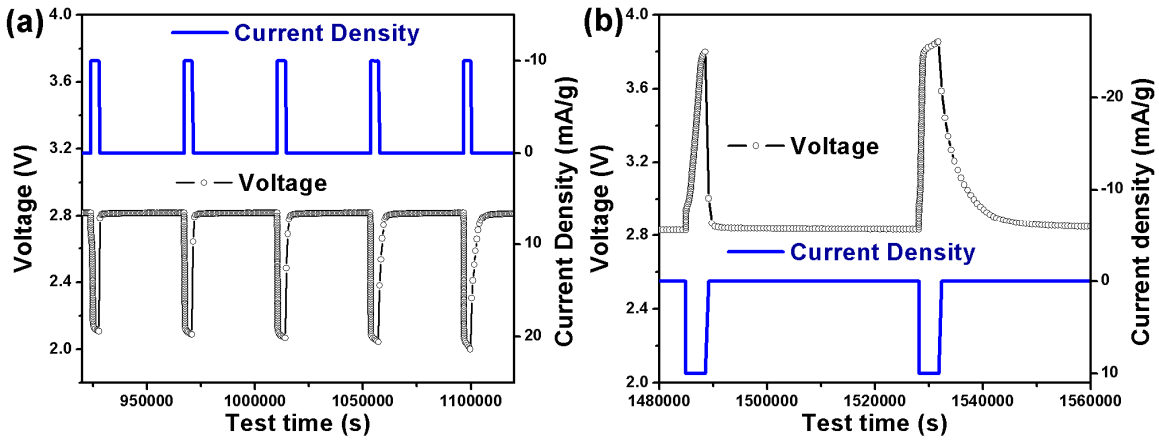

Figure 3.7. Selected segment of the voltage profiles of the HDS sample from the OCV experiment: (a) ~ 2.1 V plateau and (b) ~ 3.82 V plateau.

3.3.4 *Ex-situ* XRD data analysis

Figure 3.8 shows the *ex-situ* XRD patterns of the HDS and HOS samples during first discharge. *Ex-situ* XRD patterns were collected before and after each of the five plateaus (upper ~ 4.7 V, lower ~ 4.7 V, ~ 4 V, ~ 2.7 V, and ~ 2.1 V) as well as at points denoted by the arrows in Figure 3.6. From 5 to 3 V, both samples show three distinct cubic phases (C, C', and C'' in Figure 3.8) as lithium ions are inserted into the 8a tetrahedral sites.[104] In the HDS sample, the peaks of the cubic phases (C, C', and C") are gradually shifted to lower angles while the same peaks remain constant in the HOS sample, regardless of lithium content. This result is consistent with previous reports.[64, 67, 104] As mentioned earlier, the remaining two plateaus (~ 2.7 and ~ 2.1 V) are related to a cubic to tetragonal phase transition involving lithium ion insertion into the 16c octahedral sites.[67-69] After the ~ 2.7 V plateau, both samples display features of the tetragonal phase (T1) belonging to the $I4_1/amd$ space group as expected from the Jahn-Teller distortion of Mn^{3+} ion. However, clearly different behaviors between the two samples are observed after the ~ 2.1 V plateau. A new tetragonal phase (T2) with lower diffraction angles than the T1 phase are observed in the HDS sample, while the T2 phase is not detected in the HOS sample. The *ex-situ* XRD analysis of the HDS sample reveals that the formation of the new tetragonal phase (T2) is related to the ~ 2.1 V plateau. By combining the above analysis with the consideration of the empty octahedral-site size in the HDS sample in Table 3.3, we conclude that the evolution of the new tetragonal phase (T2) in the HDS sample is due to the additional lattice strain/distortion caused by the lithium ion insertion into 16c octahedral sites in addition to the lattice distortion caused by the Jahn-Teller distortion of Mn^{3+} ions as the 16c sites in the disordered phase are smaller than the lithium ions.

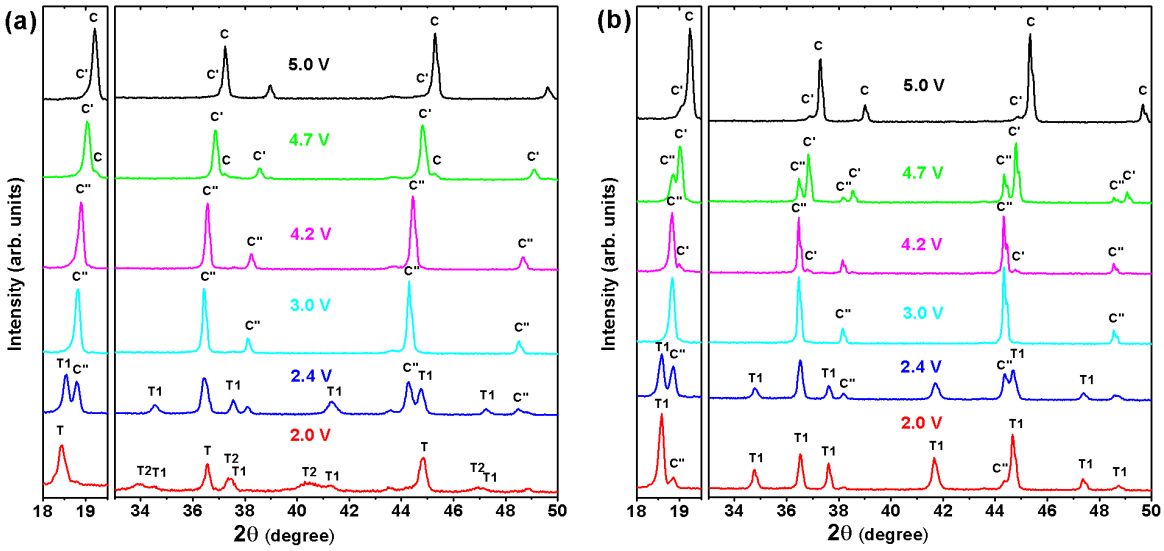

Figure 3.8. *ex-situ* XRD patterns throughout first discharge: (a) HDS sample and (b) HOS sample. C and T refer, respectively, to the cubic spinel and tetragonal spinel phases.

The above observations raise an important question: why is the second tetragonal phase (T2) observed only in the case of HDS sample but not in the case of HOS sample? To understand this issue, we performed four consecutive XRD scans on the HDS sample after it had been discharged to 2 V to see how the spinel structure transformed during the relaxation period. The results can be seen in Figure 3.9. Two distinct tetragonal phases (T1 and T2) with different lattice parameters can be seen in the initial scan. It should be noted that the intensity of the T2 phase is greater compared to that of T1, which is consistent with a larger capacity associated with the ~ 2.1 V plateau compared to that with the ~2.8 V plateau, as can be seen in Figure 3.5(a). Interestingly, after a one hour of rest period without any load, the reflections corresponding to the T2 phase have almost vanished, while the intensity of the T1 phase has increased. After 4 hours of rest period, only traces of the reflections corresponding to the T2 phase can be seen. This suggests

that the T2 phase, which is evolved by the ~ 2.1 V plateau, completely transforms to the T1 phase after 4 hours. From the foregoing analysis, we can finally understand why the T2 phase is not detected in the *ex-situ* XRD data of the HOS sample. As we can see in Figure 3.5(a), the HOS sample shows a much longer ~ 2.7 V plateau and much shorter ~ 2.1 V plateau compared to those of the HDS sample. In other words, the T2 phase content is much lower than the T1 phase content after discharging down to 2 V in the HOS sample. Both the low T2 phase content and the phase transformation of the T2 phase to the T1 phase over time explain the difficulty of detecting the T2 phase in the *ex-situ* XRD data of the HOS sample.

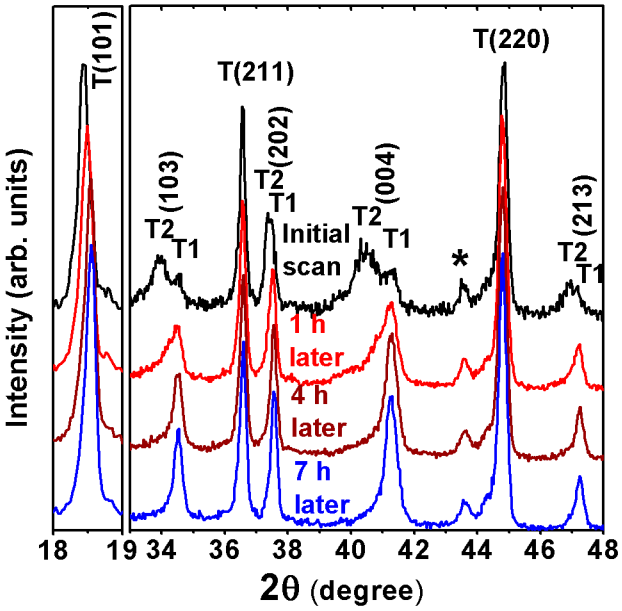

Figure 3.9. Four consecutive *ex-situ* XRD patterns of the HDS sample after discharging down to 2 V.

In order to investigate the structural parameter changes during the discharge process, the lattice parameters of the phases present at each voltage plateau were refined.

For direct comparison, the cubic phase (*Fd*-3*m*) parameters are converted to those of the tetragonal phase ($I4_1/amd$) by the conversion, $a_T = a_C/\sqrt{2}$ and $c_T = a_C$, where *T* and *C* refer, respectively, to tetragonal and cubic structures.[67] The differences in the lattice parameters between the phases are shown in Figure 3.10. Among them, we particularly calculate the changes of two values (c_T/a_T and unit cell volume) between the initial cubic phase (C) and the final tetragonal phases (T1 and T2). In the case of HDS sample, the T1 and T2 phases have higher c_T/a_T values of, respectively, 1.53 and 1.56 compared to that of the initial cubic phase C (1.41). The T1 and T2 phases also have larger unit cell volumes of, respectively, 287 and 292 $Å^3$ compared to that of the initial cubic phase C (257 $Å^3$). In short, the c_T/a_T and unit cell volume increase, respectively, by 8.32 and 11.85 % upon transformation from the C to T1 phase, while the c_T/a_T and the unit cell volume increase, respectively, by 10.25 and 13.75 % upon transformation from the C to T2 phase. In the case of HOS sample, we can only calculate the changes of c_T/a_T and unit cell volume values from C to T1 phase due to the difficulty of detecting the unstable T2 phase. In keeping with the results from experiments on the HDS sample, the c_T/a_T and the unit cell volume values are also larger in the T1 phase relative to the C phase for the HOS sample. The T1 phase has a larger c_T/a_T value and unit cell volume of, respectively, 1.51 and 285 $Å^3$ compared to the c_T/a_T value and unit cell volume of the C phase (1.41 and 256 $Å^3$). This corresponds to a 6.85 % increase in c_T/a_T and a 11.56 % increase in unit cell volume upon transformation from C to T1 phase. It should be noted that the cubic to T2 phase transformation corresponds to a greater structural change than the cubic to T1 phase transformation. In other words, the HDS sample undergoes more drastic structural changes than the HOS sample due to the higher T2 phase content after discharging down to 2 V.

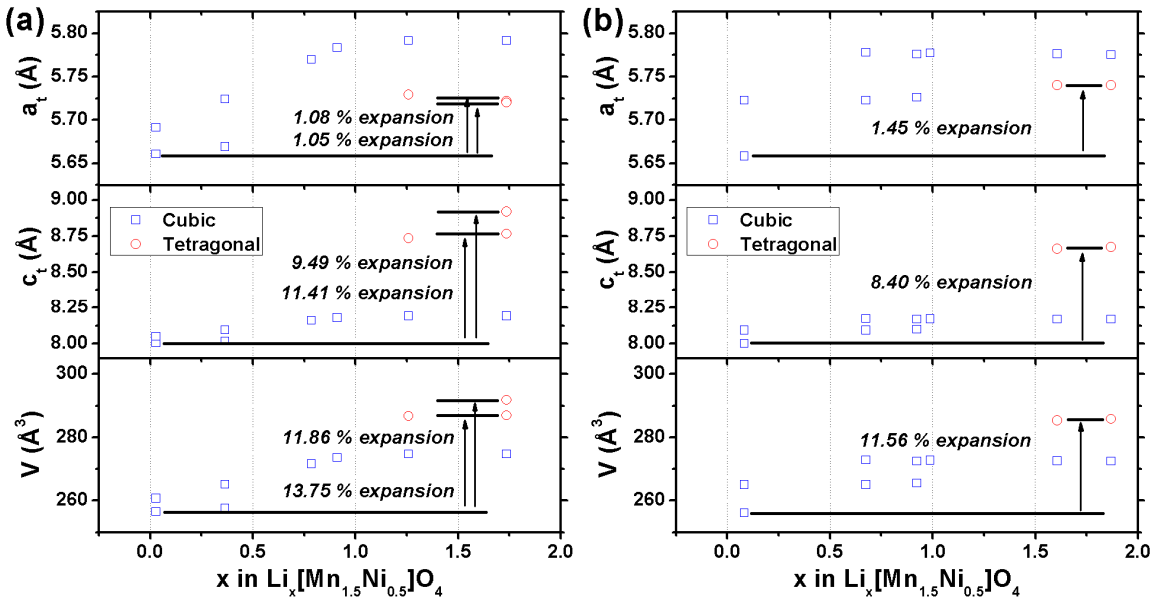

Figure 3.10. Lattice parameter variation during first discharge: (a) HDS sample and (b) HOS sample.

To investigate whether structural changes are reversible or not, *ex-situ* XRD patterns were also obtained for the HDS and HOS samples after charging to each of the five voltage plateaus (~ 2.9 V, ~ 3.82 V, ~ 4 V, lower ~ 4.7 V, and upper ~ 4.7 V). Figure 3.11 shows the *ex-situ* XRD patterns obtained during second charge. After the ~ 2.9 V plateau, T2 phases are not observed in either sample and intensities of the reflections from the tetragonal phase are reduced as those from the cubic phase (C") are increased. No reflections from the tetragonal phases are observed in either sample after they have been charged to ~ 3.9 V. This supports the assertion from the electrochemical analysis that the ~ 3.82 V plateau is attributed to the tetragonal to cubic transition. In short, lithium ions can reversibly insert into the 16c octahedral sites in both the samples. This result is in contrast to Park et al.'s[69] report that the tetragonal to cubic transition is only reversible in ordered $LiMn_{1.5}Ni_{0.5}O_4$ spinel ($P4_332$).

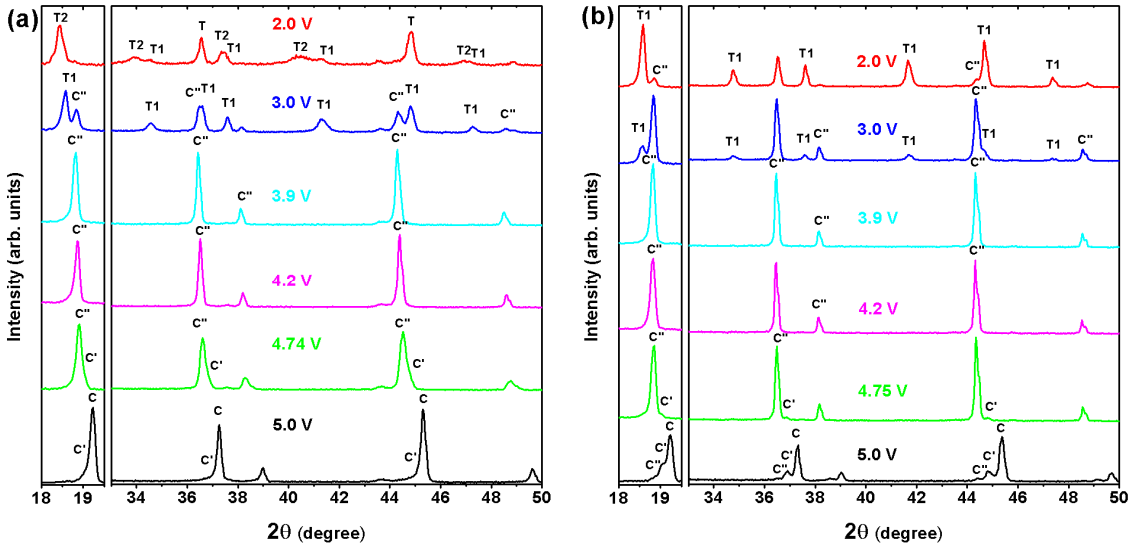

Figure 3.11. *ex-situ* XRD patterns throughout second charge: (a) HDS sample and (b) HOS sample. C and T refer, respectively, to the cubic spinel and tetragonal spinel phases.

Between 3.9 and 5 V, both the samples show three distinct cubic phases (C", C', and C in Figure 3.11) upon lithium removal from the 8a tetrahedral sites. A similar transformation is seen during the discharge process where the peaks of the cubic phases (C' and C") in the HDS sample are gradually shifted to a higher angle, while the peaks of the cubic phases (C' and C") in the HOS sample remain constant. The changes in structural parameters during the charge process are summarized in Figure 3.12. Similar to the results found during discharge, the HDS sample undergoes more drastic structural changes than the HOS sample during the charge process due to a higher content of the T2 phase at the discharged state. In the HDS sample, c_T/a_T and the unit cell volume decrease by, respectively, 7.68 and 10.54 % upon transformation from T1 to C phase, while the c_T/a_T and the unit cell volume decrease, respectively, by 9.30 and 12.03 % from T2 to C phase. In the HOS sample, the c_T/a_T and the unit cell volume decrease by, respectively, 6.41 and 10.48 % from T1 to C phase.

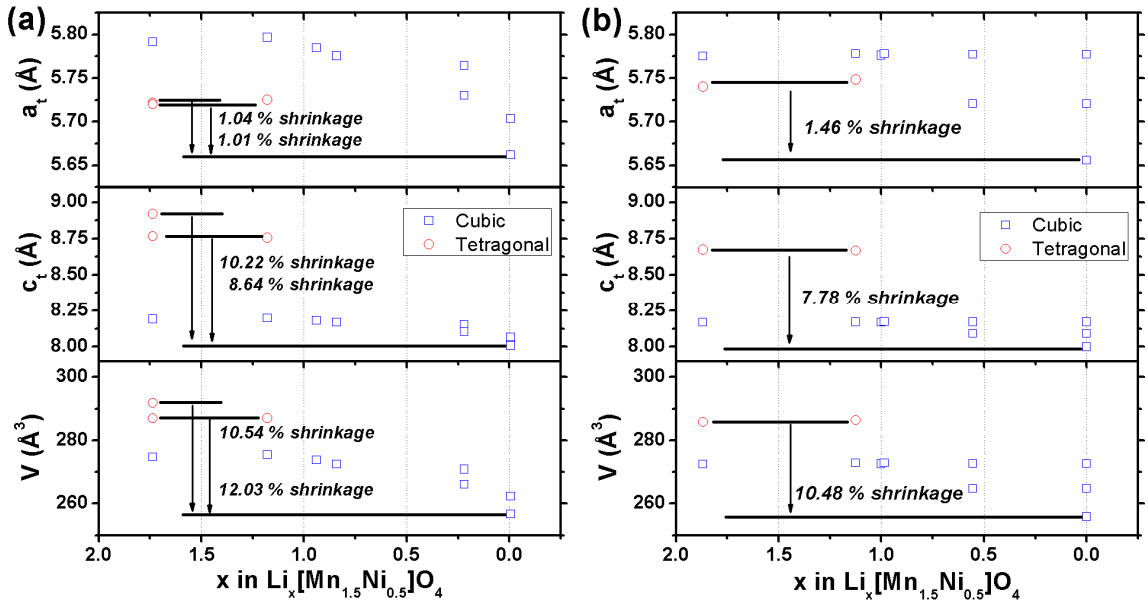

Figure 3.12. Lattice parameter variation during second charge: (a) HDS sample and (b) HOS sample.

In summary, *ex-situ* XRD data analysis confirms the following: (i) lithium ions can reversibly insert into the 8a tetrahedral and16c octahedral sites in both the ordered and disordered samples; (ii) two tetragonal phases (T1 and T2) evolve during lithium ion insertion into 16c octahedral sites; (iii) the HDS sample undergoes more drastic structural changes than the HOS sample due to a larger lattice distortion; and (iv) the unstable T2 phase spontaneously transforms to the T1 phase over time when the load is removed.

3.3.5 Effect of the evolution of two tetragonal phases on the capacity fade of $LiMn_{1.5}Ni_{0.5}O_4$ upon cycling between 5.0 and 2.0 V

To investigate the effect of the evolution of each tetragonal phase on the capacity fade of $LiMn_{1.5}Ni_{0.5}O_4$, cycle performances of $LiMn_{1.5}Ni_{0.5}O_4$ with three different voltage windows (5.0 – 3.5 V, 5.0 – 2.5 V and 5.0 – 2.0 V) were compared. From the cycle performances between 5.0 and 3.5 V, the effect of structural changes arising from cubic

to tetragonal transformations can be excluded due to the absence of tetragonal phase formation above 3.0 V. From the cycle performances between 5.0 and 2.5 V, the effect of the structural change from cubic to T1 phase on the capacity fade can be obtained due to the absence of T2 phase above 2.5 V. And finally, from the cycle performances between 5.0 and 2.0 V, the effect of the structural changes from cubic to T1 and T2 on the capacity fade can be obtained.

As we can see in Figure 3.13, capacity fade trends are different depending on the cycling voltage window. Between 5 and 3.5 V, all samples show a similar first discharge capacity of about 130 mAh/g. After the 50^{th} cycle, all samples show a similar capacity retention of 85 %. However, the capacity fade trend changes when the cycling voltage window is extended to 5 – 2.5 V. All samples show higher capacity fade when cycled between 5 - 2.5 V. The HOS sample shows the highest capacity (203 mAh/g) in the first cycle, but exhibits larger capacity fade than the other samples due to the extensive cubic to T1 phase transformation. After 50 cycles, the HOS sample shows a capacity retention value of about 57 % while the other three samples show capacity retention values of ~ 70 %. Finally, all samples suffer from significantly larger capacity fade when the cycling voltage window is extended to 5 - 2 V. It is noted that the capacity fade rate is higher during initial ten cycles in the more disordered samples. This can be explained by the increase in the capacity in the ~ 2.1 V plateau at the expense of ~ 2.7 V plateau as the ordering in the sample decreases (as can be seen in Figure 3.5(a)). According to *ex-situ* XRD data, the ~ 2.1 V plateau is related to the cubic to T2 phase transition, which exhibits a more drastic change in cell volume and *c/a* ratio compared to the cubic to T1 phase transition. Therefore, the HOS sample shows the lowest capacity fade rate and the HDS sample shows the highest capacity fade rate during cycling. Thus, it can be concluded that the severe structural changes that are associated with the cubic to

tetragonal phase transitions limit the reversibility of $LiMn_{1.5}Ni_{0.5}O_4$ below 3 V, but the HDS sample is more severely affected than the HOS sample.

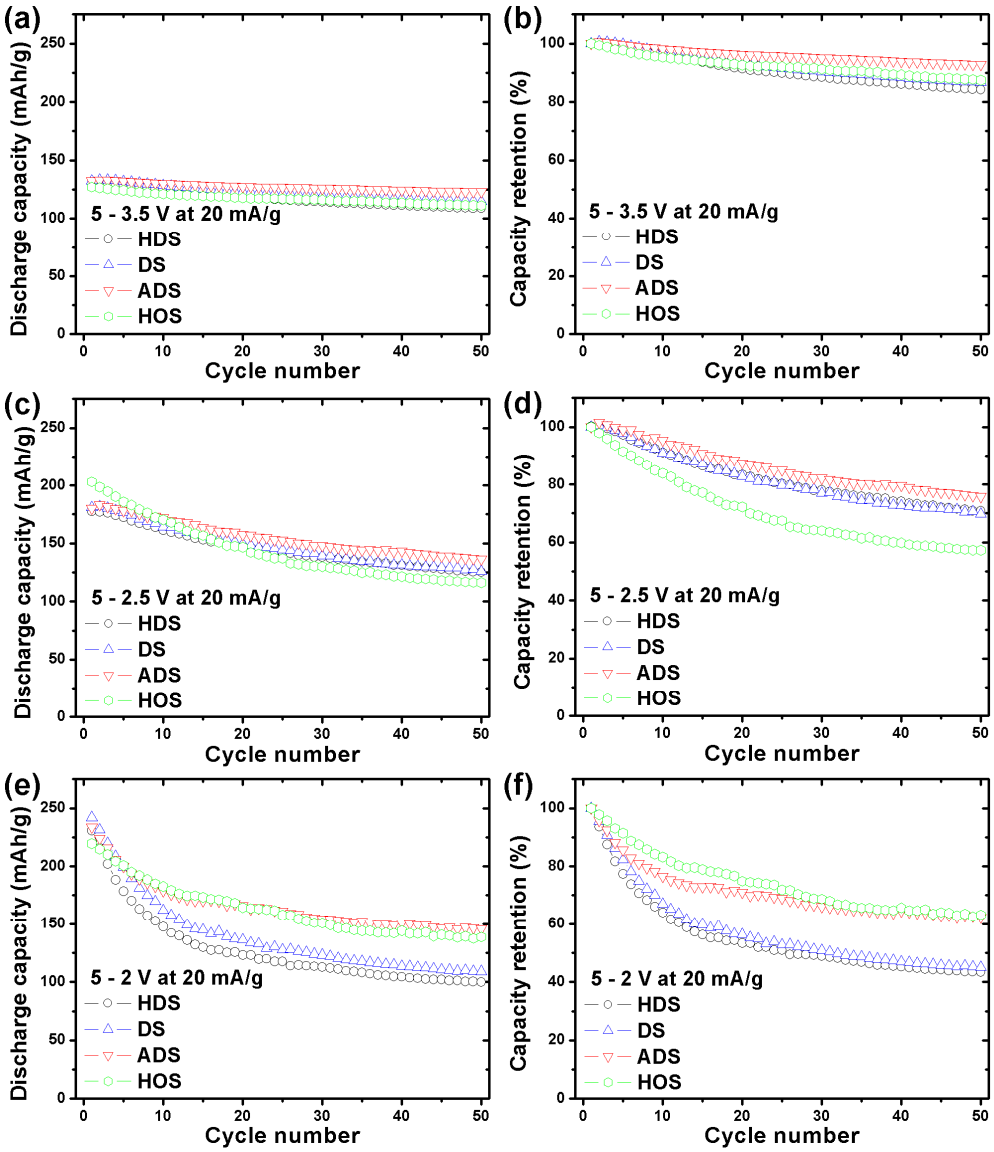

Figure 3.13. Cyclability data of the four samples operated within three different voltage windows: discharge capacity at (a) 5.0 – 3.5 V, (c) 5.0 – 2.5 V, and (e) 5.0 – 2.0 V at 20 mA/g and capacity retention at (b) 5.0 – 3.5 V, (d) 5.0 – 2.5 V, and (f) 5.0 – 2.0 V at 20 mA/g.

3.4 CONCLUSIONS

The transition-metal ion ordering affects both the electrochemical and structural characteristics of $LiMn_{1.5}Ni_{0.5}O_4$ when operated between 5.0 and 2.0 V. Two plateaus at ~ 2.7 and ~ 2.1 V during discharge and at ~ 2.9 and ~ 3.82 V during charge appear when lithium ions are reversibly inserted/extracted into/from the 16c octahedral sites. From structural studies, it is understood that the larger empty octahedral sites available in the cation-ordered spinel phase explain why longer ~ 2.7 V plateau during discharge and ~ 2.9 V plateau during charge are displayed by the more ordered spinel. *Ex-situ* XRD analysis confirms that the evolution of two tetragonal phases (T1 and T2) is linked with the two distinct ~ 2.7 and ~ 2.1 V plateaus corresponding to the insertion of lithium ions into the 16c octahedral sites. The evolution of the first tetragonal phase (T1) is attributed to the Jahn-Teller distortion of Mn^{3+} ions. The evolution of the second tetragonal phase (T2) originates from the additional lattice distortion caused by the insertion of larger lithium ions into smaller 16c octahedral sites in the disordered phase. The gradual increase in OCV from 2.0 to 2.8 V over time when the load is removed is attributed to the spontaneous transformation of the unstable T2 phase to the T1 phase. Finally, a comparison of the performances of each sample when cycled within different voltage windows reveals that both the volume and *c/a* ratio changes associated with the cubic to T1 and T2 phase transitions cause unacceptable capacity fade when $LiMn_{1.5}Ni_{0.5}O_4$ is cycled between 5.0 – 2.0 V. This restricts its potential use as a high energy cathode in the entire 5.0 – 2.0 V range despite its impressive theoretical capacity of ~ 294 mAh/g. Nevertheless, it exhibits good capacity retention when cycled above 3 V.

Chapter 4: Effect of doping on the cation ordering and the charge-discharge behavior of $LiMn_{1.5}Ni_{0.5-x}M_xO_4$ (M = Cr, Fe, Co, and Ga) spinels between 5 and 2 V

4.1 INTRODUCTION

It has been reported in the literature that partial substitutions of Mn or Ni by other cations such as Cr, Fe, Co, Zn, and Ga can improve the electrochemical performance of $LiMn_{1.5}Ni_{0.5}O_4$ spinels by stabilizing the disordered phase, suppressing the formation of the rocksalt impurity phase, and establishing a stable electrode-electrolyte interface.[71-73, 114-116] As we revealed in Chapter 3, differences in cation ordering affects the charge-discharge behavior of $LiMn_{1.5}Ni_{0.5}O_4$ spinels during operation between 5.0 and 2.0 V, especially below 3 V when lithium ions are inserted into empty 16c octahedral sites.

For that reason, the degree of cation ordering could be compared by examining the lithium insertion reaction below 3 V into the empty 16c sites. It is expected that different dopant ions can also affect the degree of ordering of $LiMn_{1.5}Ni_{0.5-x}M_xO_4$ spinels and consequently influence the lithium insertion reaction below 3 V. Despite many reports investigating the effect of cation doping on the electrochemical performance of $LiMn_{1.5}Ni_{0.5-x}M_xO_4$ spinels at operating high-voltages (> 3.5 V),[71-73, 114-116] to our best knowledge, no studies have focused on the effect of cation doping on the degree of ordering variations of the $LiMn_{1.5}Ni_{0.5-x}M_xO_4$ spinels. Accordingly, we synthesized various doped $LiMn_{1.5}Ni_{0.5-x}M_xO_4$ (M = Cr, Fe, Co, and Ga) spinels by varying dopant ions and compositions and the effects of doping on the degree of cation ordering in $LiMn_{1.5}Ni_{0.5-x}M_xO_4$ (M = Cr, Fe, Co, and Ga) spinels are investigated by the analysis of the charge-discharge behavior in the wide operating voltage of 5.0 – 2.0 V.

4.2 EXPERIMENTAL

4.2.1 Synthesis

The mixed metal hydroxide precursor $Mn_{0.75}Ni_{0.25-x}M_x(OH)_2$ (M = Cr, Fe, Co, and Ga, x = 0.08 or 0.16) was obtained via a co-precipitation method as presented in Chapter 2 by a dropwise addition of the aqueous solution containing required amounts of metal acetate or nitrate (Mn : Ni : M = 0.75 : 0.25-x : x) into a 2 M KOH solution under continuous stirring. Chromium nitrate, iron acetate, cobalt acetate, and gallium nitrate were used for dopant source of M = Cr, Fe, Co, and Ga, respectively. Final $LiMn_{1.5}Ni_{0.5-x}M_xO_4$ (M = Cr, Fe, Co, and Ga, x = 0.08 or 0.16) spinel samples were prepared by mixing $Mn_{0.75}Ni_{0.25-x}M_x(OH)_2$ with required amount of lithium hydroxide, followed by heating the hydroxide mixture at 900 ^oC for 12 h in air with a 1 ^oC/min cooling rate, which are hereafter referred to as "900M8" for $LiMn_{1.5}Ni_{0.42}M_{0.08}O_4$ and "900M16" for $LiMn_{1.5}Ni_{0.34}M_{0.16}O_4$. Double-doped $LiMn_{1.5}Ni_{0.42}Fe_{0.08}Co_{0.08}O_4$ was prepared by the same heating conditions as the 900M8 samples, which is hereafter referred to as "900Fe8Co8". For a portion of the 900M8 samples, post annealing was applied by heating at 700 ^oC for 96 h in air with a 1 ^oC/min cooling rate, which is hereafter referred to as "700M8". For a comparison, two kinds of undoped $LiMn_{1.5}Ni_{0.5}O_4$ samples were also synthesized by controlling the heat treatment condition as described in Chapter 3. The first $LiMn_{1.5}Ni_{0.5}O_4$ sample was obtained by the same heating condition as for the 900M8 samples, which is hereafter referred to as "900LMNO". The second $LiMn_{1.5}Ni_{0.5}O_4$ sample was obtained by post annealing the 900LMNO sample at 700 ^oC for 96 h in air with a 1 ^oC/min cooling rate, which is hereafter referred to as "700LMNO".

4.2.2 Characterization

XRD data were collected with a Rigaku Ultima-IV system (Cu Kα radiation). The lattice parameters of pristine samples were obtained with Rigaku PDXL software. Electrochemical properties of the $LiMn_{1.5}Ni_{0.5-x}M_xO_4$ (M = Cr, Fe, Co, and Ga) spinel samples were evaluated with 2032-type coin cells. The coin cells were assembled as described in Chapter 2.

4.3 RESULT AND DISCUSSION

4.3.1 Structural analysis

The XRD patterns of the pristine $LiMn_{1.5}Ni_{0.5-x}M_xO_4$ (M = Cr, Fe, Co, and Ga; x = 0, 0.08) samples are shown in Figure 4.1. As reported,[72] all $LiMn_{1.5}Ni_{0.5-x}M_xO_4$ (M = Cr, Fe, Co, and Ga; x = 0, 0.08) samples synthesized at 900 ^oC show the disordered spinel phase with space group *F*d-3*m*, indicating the absence of long-range order in the samples. As seen in Chapter 3, 900LMNO samples exhibit weak reflections possibly from a $Li_xNi_{1-x}O$[31, 32, 70] or Ni_6MnO_8[107] impurity phase. However, the relative intensity of the impurity phase is almost negligible in the XRD data of the 900M8 samples. As described in Chapter 3, the 700LMNO sample has the ordered spinel phase with the space group $P4_332$, as indicated by the existence of superstructure reflections in the XRD pattern.[104-106] The relative amount of the impurity phase is dramatically decreased in the 700LMNO sample, as compared to that of the 900LMNO sample refined in Chapter 3. For all the 700M8 samples, disordered spinel phases are maintained because M^{3+} dopant ions stabilize the disordered phase.

To identify the effect of the doping and post annealing on the lattice parameter of $LiMn_{1.5}Ni_{0.5-x}M_xO_4$ (M = Cr, Fe, Co, and Ga; x = 0, 0.08) samples, refined lattice parameters before and after post-annealing at 700 ^oC are listed in Table 4.1. We showed

in Chapter 3 with undoped $LiMn_{1.5}Ni_{0.5}O_4$ samples that the lattice parameter decreases with increasing degree of ordering in the samples due to the optimization of the space occupation in the lattice, through larger Ni^{2+} ions and smaller Mn^{4+} ions, respectively, occupying the larger 4b sites and smaller 12d sites.[66] Otherwise, lattice parameter differences between $LiMn_{1.5}Ni_{0.5-x}M_xO_4$ samples with different dopant ions cannot be used for comparing the relative degree of ordering between samples because different ionic radii of dopant ions also affect the lattice parameter changes of $LiMn_{1.5}Ni_{0.5-x}M_xO_4$ samples. However, the lattice parameter changes of each 900M8 sample after post-annealing at 700 ^oC can be used to determine whether there is a further increase in the degree of ordering with post-annealing at 700 ^oC. In addition to the undoped sample, the lattice parameters of Fe and Ga-doped samples decrease after post-annealing at 700 ^oC possibly due to both an oxidation of the larger Mn^{3+} ions into the smaller Mn^{4+} ions and an optimization of the space occupation in the lattice through an increased degree of ordering in the 16d sites. This is also supported by microstrain analysis and electrochemical testing that will be discussed later (microstrain and electrochemical analysis in later discussions reveal that the lattice parameter decrease of Ga-doped sample can be mainly attributed to the oxidation of Mn^{3+} to Mn^{4+}). Cr and Co-doped samples do not show noticeable lattice parameter changes after post-annealing at 700 ^oC, indicating there is no further increase of cation ordering in the 16d sites.

In Chapter 3, we demonstrated that the microstrain differences of the $LiMn_{1.5}Ni_{0.5}O_4$ samples can be used to determine the qualitative variation of the degree of cation ordering in the samples because ordering in the 16d sites relaxes the lattice strain in $LiMn_{1.5}Ni_{0.5}O_4$ by space optimization.[66] The variations of the microstrain in each $LiMn_{1.5}Ni_{0.5-x}M_xO_4$ (M = Cr, Fe, Co, and Ga; x = 0, 0.08) sample after post annealing are compared with the Williamson-Hall plot[108] in Figure 4.2. As expected from the results of

lattice parameter changes, undoped and Fe-doped samples show noticeably decreased microstrain after post annealing as shown by a decrease in the slope of the plot, possibly due to the increased ordering in the 16d sites, which is also supported by electrochemical data analyses that will be discussed later. Cr, Co, and Ga-doped samples do not show noticeable microstrain changes after post-annealing at 700 ^{o}C, indicating no further increase of cation ordering in the 16d sites. The comparison of the microstrain between the $LiMn_{1.5}Ni_{0.5-x}M_xO_4$ (M = Cr, Fe, Co, and Ga; x = 0, 0.08) samples before and after post-annealing at 700 ^{o}C are shown with the Williamson-Hall plot in Figure 4.3. Before post annealing, microstrain decreases in the following order: Co-doped ≈ Fe-doped > Ga-doped > undoped > Cr-doped. After post-annealing at 700 ^{o}C, the order of the relative microstrain values is changed due to the significant decrease of micorstrain in the undoped sample: Co-doped > Fe-doped ≈ Ga-doped > Cr-doped > undoped. However, microstrain differences between the $LiMn_{1.5}Ni_{0.5-x}M_xO_4$ samples with different dopant ions might not originate solely from the difference of the relative degree of ordering between samples; differences in the ionic radii of dopant ions affect the lattice parameter changes, and could also impact the microstrain changes of the samples.[117]

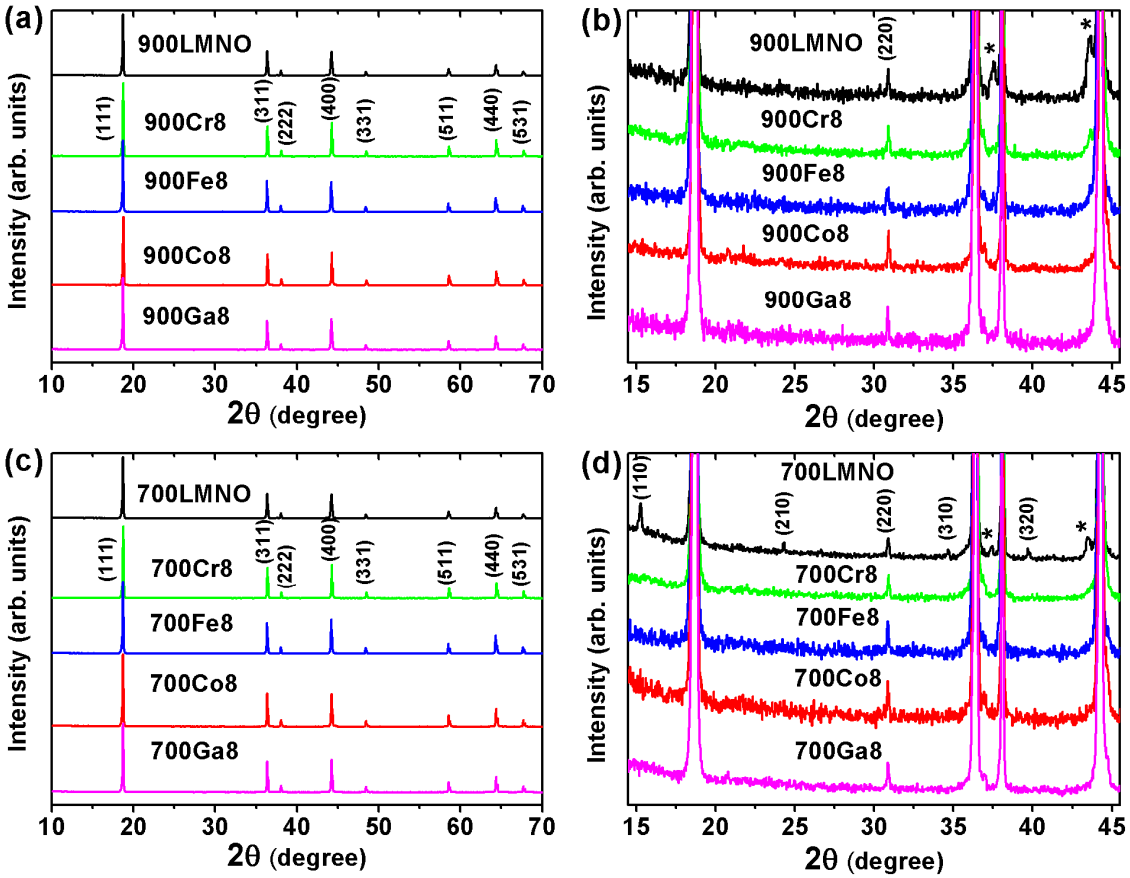

Figure 4.1. XRD patterns of $LiMn_{1.5}Ni_{0.5-x}M_xO_4$ (M = Cr, Fe, Co, and Ga; x = 0, 0.08) samples before and after post-annealing at 700 ^oC: full range (a and c) and enlarged region (b and d) to show the superstructure reflections arising from the Mn^{4+} and Ni^{2+} ordering in the 16d octahedral sites. Asterisks refer to the reflections arising from $Li_xNi_{1-x}O$ or Ni_6MnO_8 impurity phases.

Table 4.1 Refined lattice parameter of $LiMn_{1.5}Ni_{0.5-x}M_xO_4$ (M = Cr, Fe, Co, and Ga; x = 0, 0.08) samples before and after post-annealing at 700 ^oC

Sample	Lattice constant (Å)	
	Before post-annealing at 700 ^oC	After post-annealing at 700 ^oC
$LiMn_{1.5}Ni_{0.5}O_4$	8.1799(1)	8.1733(1)
$LiMn_{1.5}Ni_{0.42}Cr_{0.08}O_4$	8.1790(1)	8.1790(1)
$LiMn_{1.5}Ni_{0.42}Fe_{0.08}O_4$	8.1924(1)	8.1891(1)
$LiMn_{1.5}Ni_{0.42}Co_{0.08}O_4$	8.1784(1)	8.1785(1)
$LiMn_{1.5}Ni_{0.42}Ga_{0.08}O_4$	8.1849(1)	8.1839(1)

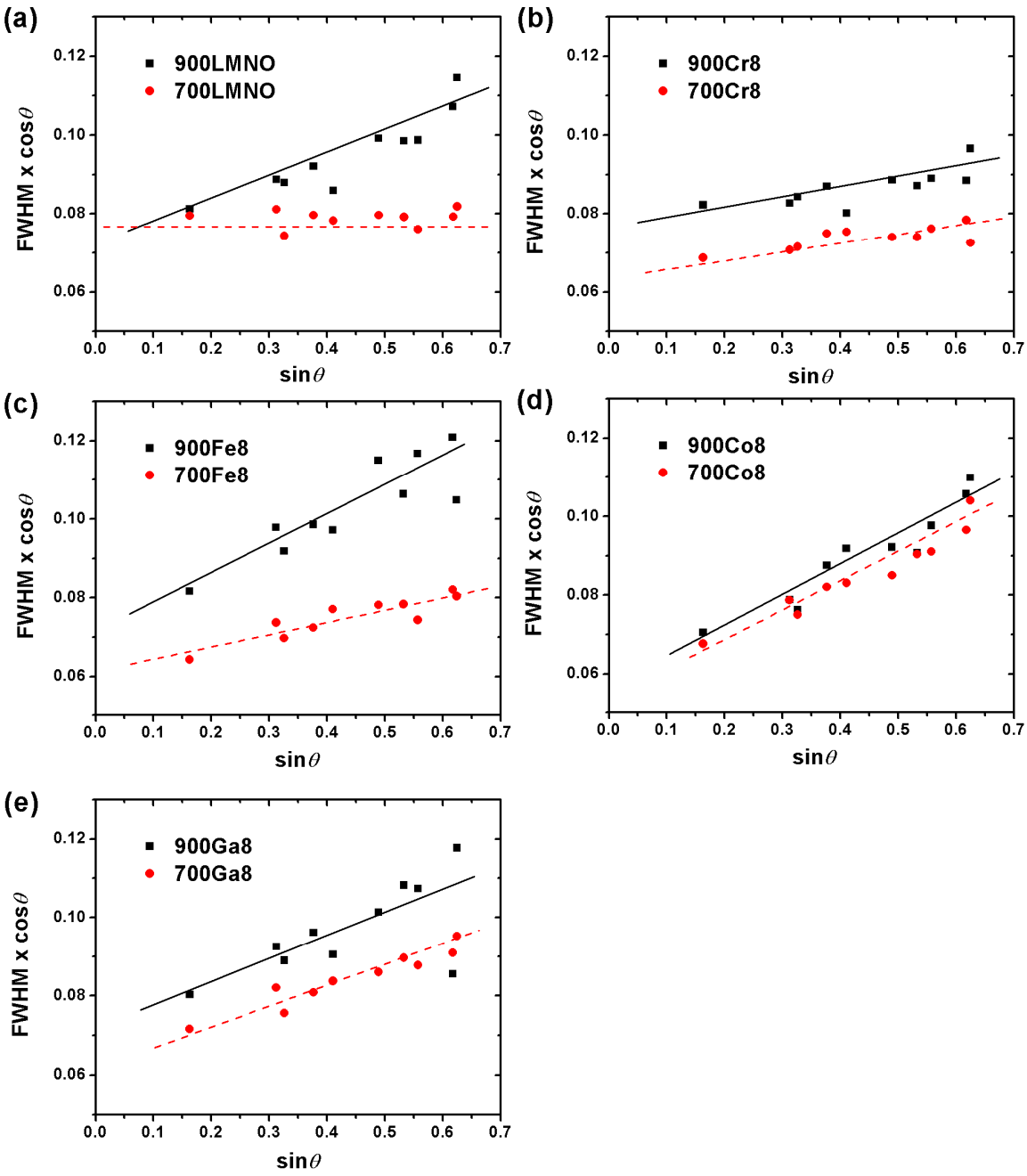

Figure 4.2. Williamson-Hall plot of $LiMn_{1.5}Ni_{0.5-x}M_xO_4$ (M = Cr, Fe, Co, and Ga; x = 0, 0.08) samples before and after post-annealing at 700 ^{o}C based on the XRD patterns in Figure 4.1, revealing the lattice strain variation: (a) undoped, (b) Cr-doped, (c) Fe-doped, (d) Co-doped, and (e) Ga-doped.

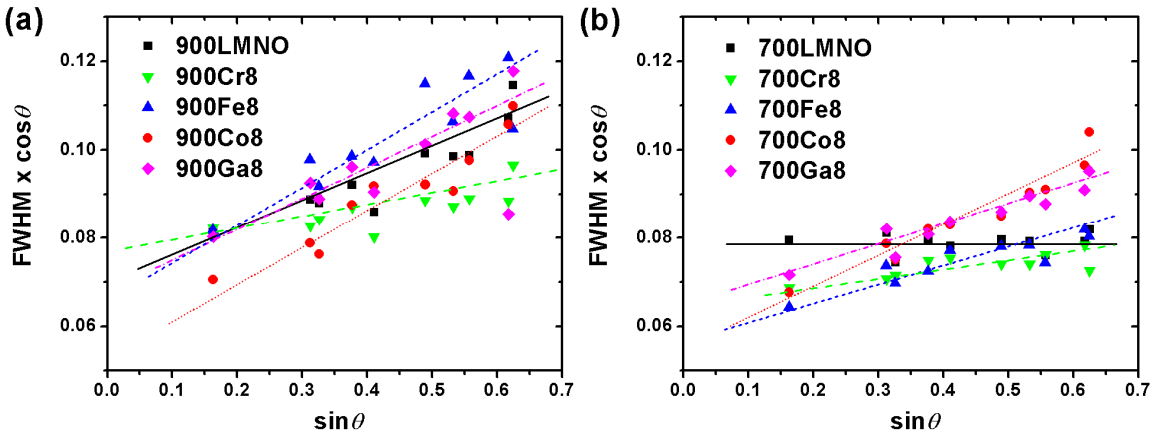

Figure 4.3. Williamson-Hall plot of $LiMn_{1.5}Ni_{0.5-x}M_xO_4$ (M = Cr, Fe, Co, and Ga; x = 0, 0.08) samples before and after post annealing at 700 ^oC based on the XRD patterns in Figure 4.1, revealing the lattice strain variation: (a) before post-annealing at 700 ^oC and (b) after post-annealing at 700 ^oC.

4.3.2 First discharge and second charge profiles at 5.0 – 2.0 V

4.3.2.1 Effect of different dopant ions

The first discharge and second charge profiles, along with differential capacity plots of the $LiMn_{1.5}Ni_{0.5-x}M_xO_4$ (M = Cr, Fe, Co, and Ga; x = 0, 0.08) samples before and after post-annealing at 700 ^oC at a current density of 10 mA/g are shown in Figure 4.3. The first discharge profile variations of each sample after post-annealing at 700 ^oC are also compared in Figure 4.4 to clearly show the effect of annealing on each sample. All samples were first charged to 5.0 V from the OCV state at a current density of 10 mA/g before discharging to 2.0 V. Due to the higher polarization of the Fe, Co and Ga-doped samples at low voltages below 2.5 V, those samples were discharged below 2 V until discharge capacity reached twice the value of the discharge capacity value at 3.5 V to equally utilize both the 8a tetrahedral sites and 16c octahedral sites of the spinel structure.

As seen in Chapter 3, all samples show three distinctive plateaus (two at ~ 4.7 and one at ~ 4.0 V) during lithium ion insertion into the 8a tetrahedral sites. Cr-doped samples show an additional short plateau at ~ 4.9 V (small peak at ~ 4.9 V in Figure 4.4(c and f)) during lithium ion insertion into the 8a sites due to the reduction of Cr^{4+} to Cr^{3+}.[118] All doped samples exhibit a longer ~ 4.0 V plateau length compared to that of the undoped sample due to an increase of Mn^{3+} content resulting from a substitution of M^{3+} for Ni^{2+}.[103]

As confirmed in Chapter 3, the two plateaus (~ 2.7 and ~ 2.1 V) shown below 3 V are attributed to the reduction of Mn^{4+} to Mn^{3+} involving lithium ion insertion into empty 16c octahedral sites of the spinel structure, which is associated with the evolution of two tetragonal phases (T1 and T2) from the cubic phase. It was demonstrated in Chapter 3 that the relative capacity variation at the ~ 2.7 and ~2.1 V can be used to determine qualitatively the relative degree of ordering in the samples. As the degree of ordering in the spinel phase increases, the capacity at the ~ 2.7 V plateau increases at the expense of the capacity at the ~ 2.1 V plateau. The facile lithium-ion insertion into the larger empty octahedral sites (4a sites) in the ordered spinel phase explains why a longer ~ 2.7 V plateau is displayed by the more ordered spinel. In the disordered spinel phase, the empty octahedral sites (16c sites) are smaller than the size of lithium ion, resulting in a voltage polarization (from ~ 2.7 V to ~ 2.1 V plateau) during lithium ion insertion into the empty octahedral sites (16c sites). The first discharge capacity variations of all the samples between the ~ 2.7 V to ~ 2.1 V plateaus are compared in Table 4.2. In this regard, the relative degree of ordering in the samples before post-annealing at 700 ^{o}C can be qualitatively determined. (Relative degree of ordering of the samples before post-annealing at 700 ^{o}C: Cr-doped > undoped > Ga-doped > Fe-doped > Co-doped.) As expected from the lattice parameter and microstrain changes mentioned earlier (Table 4.1 and Figure 4.2), the degree of ordering in the undoped and Fe-doped samples increases

after post-annealing at 700 ^{o}C as shown by the increase in the length of the ~ 2.7 V plateau. The Ga-doped sample shows a slightly decreased ~ 4.0 V plateau without any change in the ~ 2.7 V plateau, indicating that the slight decrease in lattice parameter after post-annealing at 700 ^{o}C originates mainly from the oxidation of Mn^{3+} to Mn^{4+}. After post-annealing at 700 ^{o}C, the relative degree of ordering of the samples is changed to the following order: undoped > Cr-doped > Ga-doped > Fe-doped > Co-doped. It is noted that Co-doped and Fe-doped samples show a higher degree of disordering than the other samples irrespective of post-annealing at 700 ^{o}C. This result may be helpful to explain why Co-doped and Fe-doped samples show superior electrochemical performance compared to other cation doped samples in the literature[47, 71, 72] since it has been reported that the disordered spinels exhibit better electrochemical performance due to their high electronic and lithium ion conductivity.[104, 119] In summary, the different dopant ions affect the degree of ordering differently in the $LiMn_{1.5}Ni_{0.5-x}M_xO_4$ samples as revealed by first discharge profile analysis.

As seen in Chapter 3, two plateaus (~ 2.9 and ~ 3.8 V) appear during the second charge when lithium ions are removed from the 16c octahedral sites. The capacity at the ~ 3.8 V plateau increases at the expense of the capacity at the ~ 2.9 V plateau as the degree of ordering in the spinel phase decreases. (As seen in the variation of the intensity of the peak at ~ 3.8 V in Figure 4.4 (c and f)). The three plateaus (one at ~ 4.0 V and two at ~ 4.7 V) are observed following lithium ion removal from the 8a tetrahedral sites. Cr-doped samples show an additional short plateau at ~ 4.9 V (small peak at ~ 4.9 V in Figure 4.4(c and f)) due to the oxidation of Cr^{3+} to Cr^{4+} during charge.

Table 4.2 Comparison of the first discharge capacity of the $LiMn_{1.5}Ni_{0.5-x}M_xO_4$ (M = Cr, Fe, Co, and Ga; x = 0, 0.08) samples.

Sample	First discharge capacity (mAh/g)				
	Total	Capacity above 3 V	Capacity below 3 V		
			Total	~ 2.7 V plateau	~ 2.1 V plateau
900LMNO	261.9	132.7	129.2	60.6	68.6
700LMNO	262.2	133.1	129.1	89.3	39.8
900Cr8	259.6	132.5	127.1	79.2	47.9
700Cr8	260.5	132.1	128.4	77.5	50.9
900Fe8	259.8	130.3	129.5	39.3	90.2
700Fe8	267.3	134.7	132.6	43.6	89.0
900Co8	257.5	129.1	128.4	29.3	99.1
700Co8	260.9	130.9	130.0	27.7	102.3
900Ga8	257.8	129.5	128.3	55.1	73.2
700Ga8	259.5	130.9	128.6	54.8	73.8

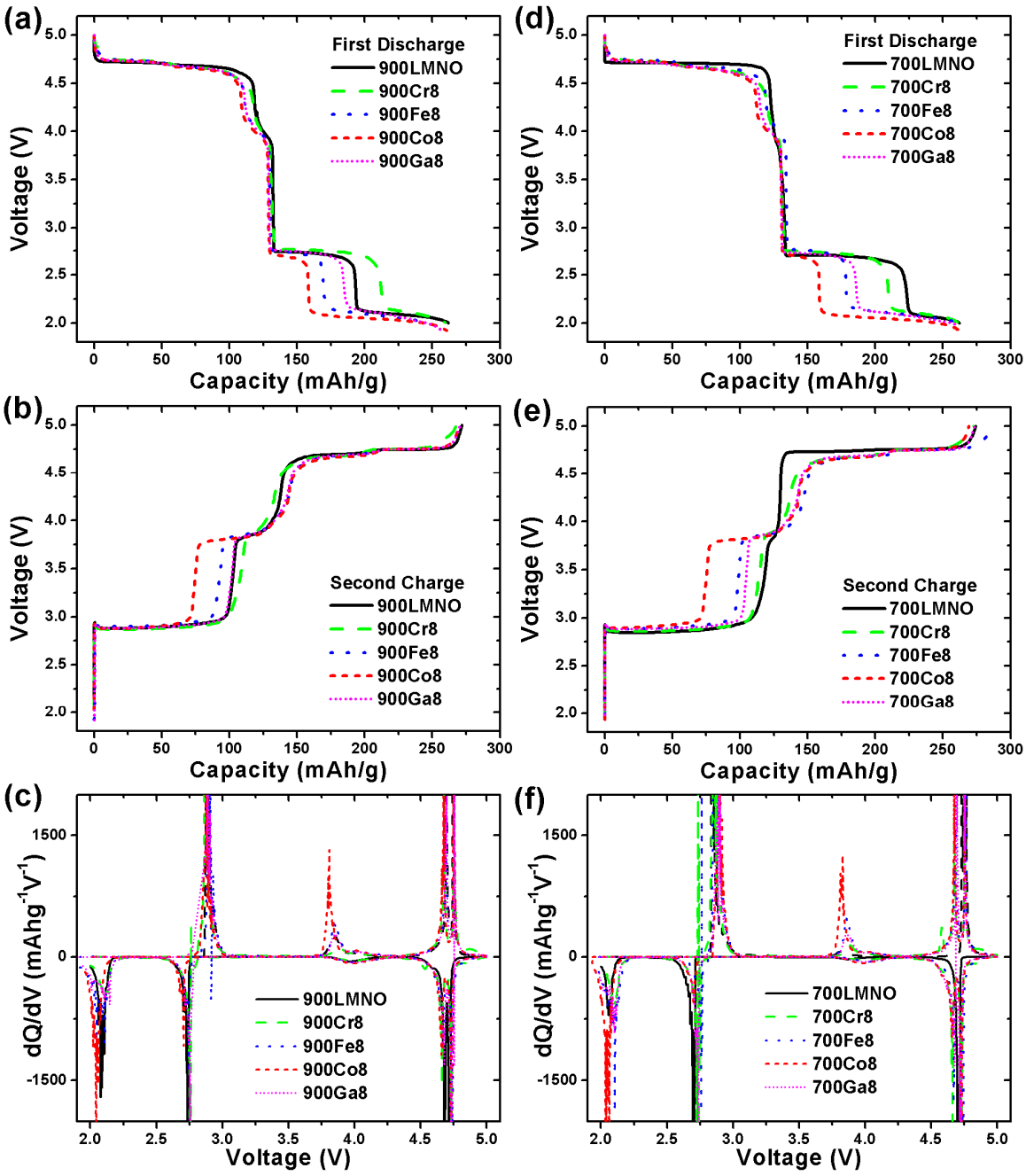

Figure 4.4. Electrochemical data of the $LiMn_{1.5}Ni_{0.5-x}M_xO_4$ (M = Cr, Fe, Co, and Ga; x = 0, 0.08) samples before and after post annealing at 700 ^oC when cycled between 5 and ~ 2 V at 10 mA/g: first discharge profiles (a and d), second charge profiles (b and e), and differential capacity (dQ/dV) plots (c and f).

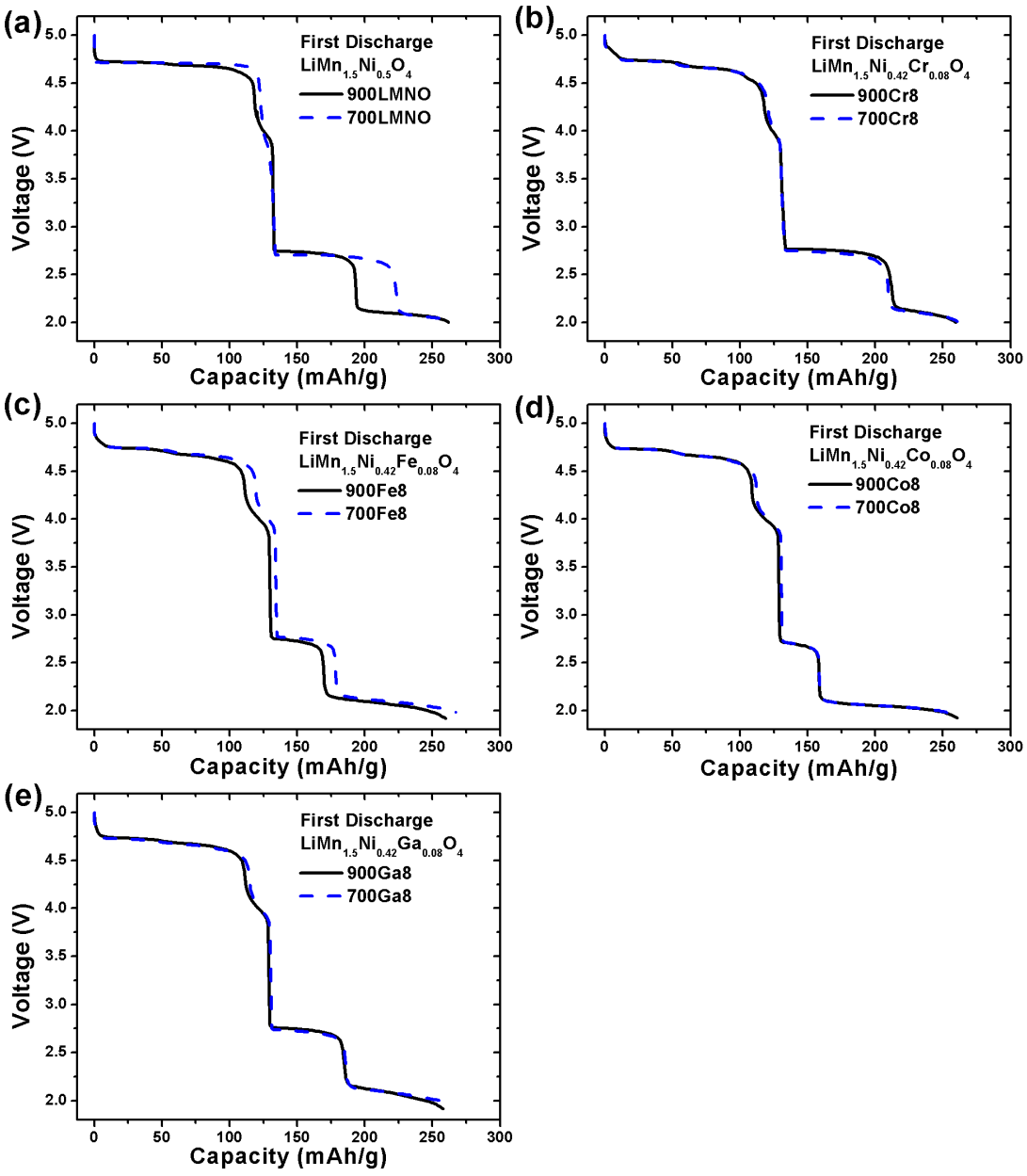

Figure 4.5. First discharge profiles of $LiMn_{1.5}Ni_{0.5-x}M_xO_4$ (M = Cr, Fe, Co, and Ga; x = 0, 0.08) samples before and after post annealing at 700 ^oC: (a) undoped, (b) Cr-doped, (c) Fe-doped, (d) Co-doped, and (e) Ga-doped samples.

4.3.2.2 Effect of dopant ion concentration

To investigate whether the dopant ion concentration can influence the degree of ordering in the $LiMn_{1.5}Ni_{0.5-x}M_xO_4$ samples, first discharge profiles of $LiMn_{1.5}Ni_{0.5-x}M_xO_4$ (M = Cr and Fe) with different *x* values are compared in Figure 4.6. Due to the reduction of both Cr^{4+} and Fe^{4+} to Cr^{3+} and Fe^{3+}, respectively, during the insertion of lithium ions into 8a tetrahedral sites, both 900Cr16 and 900Fe16 samples show a longer plateau at ~ 4.9 V than the 900Cr8 and 900Fe8 samples.[118] In addition, both the 900Cr16 and 900Fe16 samples also have a longer ~ 4.0 V plateau length than the 900Cr8 and 900Fe8 samples due to the increase in Mn^{3+} content by a substitution of M^{3+} for Ni^{2+}. However, the effects of the degree of ordering are different for Cr- and Fe-doped samples. In the case of Cr-doped sample, the degree of ordering decreases with an increase in Cr content as evidenced by the decreased length of the ~ 2.7 V plateau in the first discharge profile. However, in the Fe-doped sample, the degree of ordering does not further decrease with an increase in Fe content, as there is no noticeable change in the length of the ~ 2.7 V plateau in the first discharge profile. In order to further decrease the degree of ordering of the Fe-doped sample, (further decrease the length of ~ 2.7 V plateau), a double doped sample, 900Fe8Co8 ($LiMn_{1.5}Ni_{0.34}Fe_{0.08}Co_{0.08}O_4$), was prepared to take advantage of the high degree of disorder observed in the Co-doped sample, as seen in Figure 4.4. The first discharge profile of the 900Fe8Co8 sample is compared with that of $LiMn_{1.5}Ni_{0.5-x}Fe_xO_4$ (x = 0, 0.08, and 0.16) in Figure 4.6(b). It is noteworthy that the degree of ordering further decreases in the double doped 900Fe8Co8, as shown by the decreased length of the ~ 2.7 V plateau. Again, this result also supports the argument that the different dopant ions have different effects on the degree of ordering in the $LiMn_{1.5}Ni_{0.5-x}M_xO_4$ spinel.

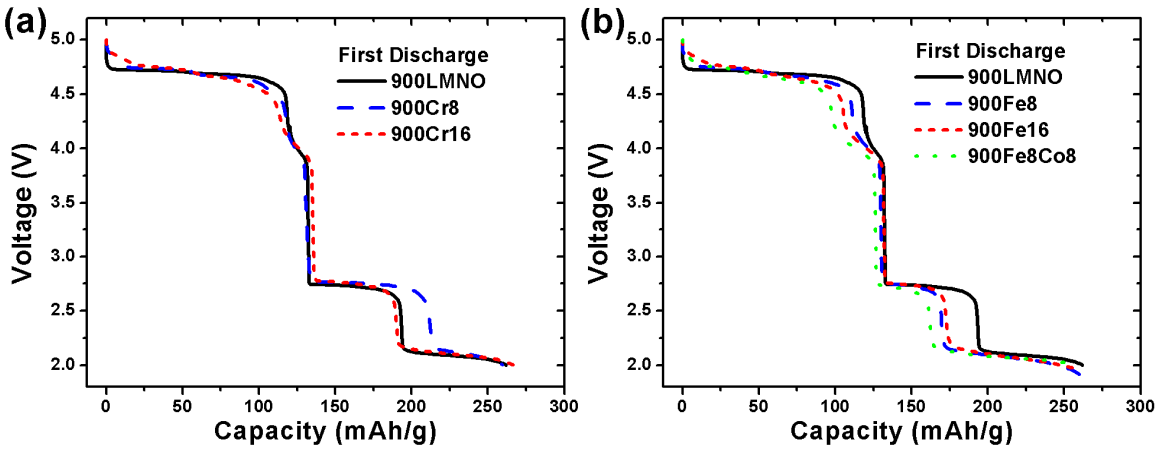

Figure 4.6. First discharge profiles of $LiMn_{1.5}Ni_{0.5-x}M_xO_4$ (M = Cr and Fe; x = 0, 0.08, and 0.16) samples: (a) Cr-doped and (b) Fe-doped and double doped (Fe and Co) samples.

4.3.3 Origin of the differences in cation ordering with different dopant ions

It became clear after analyses of the first discharge profiles that the different dopant ions strongly affect the degree of cation ordering in $LiMn_{1.5}Ni_{0.5-x}M_xO_4$. To understand why different dopant ions differ in the extent of cation order in the resulting material, we consider the situation of each doped sample when all Mn^{4+} and Ni^{2+} ions are perfectly ordered in 12d and 4b sites, respectively. As explained in Chapter 3, in the ordered spinel phase ($P4_332$), the larger Ni^{2+} ions and the smaller Mn^{4+} ions occupy, respectively, the larger 4b sites and smaller 12d sites, which results in a relaxed lattice strain.[66] Different dopants ions will have a unique impact on the lattice strain of the ordered $LiMn_{1.5}Ni_{0.5-x}M_xO_4$ due to their different ionic radii. In Table 4.3, ionic radii of the dopant ions are compared with those of Mn^{4+}, Ni^{2+}, and Mn^{3+}. Except the Fe^{3+} ion, all dopant ions have a smaller ionic radius than Mn^{3+}. Coincidentally, the Fe^{3+} ion has an identical ionic radius to Mn^{3+}. The difference in the ionic radius of M^{3+} (M = Cr^{3+}, Fe^{3+},

Co^{3+}, and Ga^{3+}) compared to that of Mn^{3+} primarily affects the site preference between 4b and 12 sites, because all M^{3+} and Mn^{3+} ions have the same trivalent state. Accordingly, it is expected that for Cr, Ga, and Co-doped samples, dopant ions prefer to occupy the smaller 12d sites and Mn^{3+} ions prefer to occupy the larger 4b sites in the ordered spinel phase. In the case of Fe-doped sample, no site preference is expected for the Fe^{3+} and Mn^{3+} ions between 12d and 4b sites due to their identical ionic radii. Differences between the ionic radii of M^{3+} (M = Cr^{3+}, Fe^{3+}, Co^{3+}, and Ga^{3+}) and Mn^{4+}, and between Mn^{3+} and Ni^{2+}, induce strain in the 12d and 4b sites, respectively. Let us assume that Mn^{3+} ions occupy 4b sites and all M^{3+} (M = Cr^{3+}, Fe^{3+}, Co^{3+}, and Ga^{3+}) ions occupy 12d sites in all doped samples, according to their site preferences (See Table 4.3). In this case, the relative lattice strain between the doped samples can be compared qualitatively by the relative strain difference in the 12d sites because all samples would have identical strain in the 4b sites. The lattice strain in the 12d sites of the doped sample will increase if the ionic radius difference between Mn^{4+} and M^{3+} (M = Cr^{3+}, Fe^{3+}, Co^{3+}, and Ga^{3+}) increases. In this regard, the relative lattice strain in the doped samples could be qualitatively expected to influence the degree of ordering. (Relative lattice strain of the doped samples in the ordered spinel phase: Fe-doped > Ga-doped > Cr-doped > Co-doped). Therefore, the relative degree of ordering in doped sample could be expected to be the inverse order of the relative lattice strain. (Expected relative degree of ordering in the doped samples: Co-doped > Cr-doped > Ga-doped > Fe-doped). This expected result of the relative degree of ordering in doped samples is well matched to the experimental results obtained by an analysis of the first discharge profile, except in the case of the Co-doped sample. As mentioned earlier, the Co-doped sample shows the highest degree of disordering among all doped samples. This deviated result for the Co-doped sample can be explained with the surface-segregation of dopant ions in $LiMn_{1.5}Ni_{0.5-x}M_xO_4$ (M = Cr, Fe, Co, and

Ga) spinels reported recently by our group.[72] Through TOF-SIMS depth profiling analysis, it was found that Cr, Fe, and Ga dopant ions segregate preferentially to the surface, while Co dopant ion does not segregate to the surface. The segregation of the dopant ions to the surface leads to a relative increase in cation ordering in the bulk due to the relatively higher concentration of Ni^{2+} ions in the bulk. In this regard, it can be explained that the Co-doped sample has a higher degree of cation disorder than other doped samples due to a random distribution of Co ions in the bulk. From the above analysis, it is plausible that the cation ordering in the Co-doped sample is disrupted more dominantly by the uniform distribution of Co ions from the surface to the bulk than by the influence of the lattice strain aspect, resulting in the highest degree of disorder among all the samples.

Table 4.3 Comparison of ionic radii of dopant ions and their expected site preference in the perfectly ordered $LiMn_{1.5}Ni_{0.5-x}M_xO_4$ (M = Cr, Fe, Co, and Ga; x = 0, 0.08) spinel phases. [LS] and [HS] refer, respectively, to low spin and high spin.

Sample	Dopant ion	Site preference in the perfectly ordered spinel phase ($P4_332$)	
		12d sites (Ionic radius in pm)	4b sites (Ionic radius in pm)
Undoped		Mn^{4+} (67)	Ni^{2+} (83)
Cr-doped	Cr^{3+}	Mn^{4+} (67)	Ni^{2+} (83)
		Cr^{3+} (75.5)	Mn^{3+} [HS] (78.5)
Fe-doped	Fe^{3+} [HS]	Mn^{4+} (67)	Ni^{2+} (83)
		No site preference Fe^{3+} [HS] or Mn^{3+} [HS] (identical ionic radius of 78.5)	
Ga-doped	Ga^{3+}	Mn^{4+} (67)	Ni^{2+} (83)
		Ga^{3+} (76)	Mn^{3+} [HS] (78.5)
Co-doped	Co^{3+} [LS]	Mn^{4+} (67)	Ni^{2+} (83)
		Co^{3+} [LS] (68.5)	Mn^{3+} [HS] (78.5)

4.4 CONCLUSIONS

The different dopant ions each exert unique effects on the degree of cation ordering in the $LiMn_{1.5}Ni_{0.5-x}M_xO_4$ (M = Cr, Fe, Co, and Ga) spinels, as shown by the variations in the discharge profiles below 3 V. It is understood that the differences in lattice strains originate from the size difference between the Mn^{4+} and M^{3+} (M = Cr, Fe, Co, and Ga) dopant ions in the ordered $LiMn_{1.5}Ni_{0.5-x}M_xO_4$ spinel phase. This in turn explains the origin of the differences in the degree of cation ordering. The highest degree of cation disorder in the Co-doped sample is mainly attributed to the non-surface-segregating character of the Co dopant ions, resulting in a decrease of the relative concentration of Ni^{2+} ions in the bulk compared to other doped samples. This study suggests that we could control the degree of cation ordering in the $LiMn_{1.5}Ni_{0.5-x}M_xO_4$ spinel by designing advantageous dopant ions at an optimal concentration.

Chapter 5: Understanding structural and electrochemical characteristics of layered-spinel composite cathodes

5.1 INTRODUCTION

As mentioned in Chapter 1, integrating the lithium-rich layered and the high-voltage spinel oxides into a composite cathode could give combination of high energy and power. Furthermore, as both the layered and spinel oxides are based on a cubic close packed oxygen array, the composite can be expected to have good interfacial characteristics. Two layered-spinel composite systems, $x\mathrm{Li_2MnO_3} - (1\text{-}x)\mathrm{Li_{1+\delta}Mn_{2-\delta}O_4}$ ($0 \leq \delta \leq 1/3$)[46, 74] and $x(\mathrm{Li_2MnO_3 \cdot Li[Mn_{0.5}Ni_{0.5}]O_2}) - (1\text{-}x)\mathrm{Li[Mn_{1.5}Ni_{0.5}]O_4}$ ($0 \leq x \leq 1$)[75-78] have been studied in the literature. In order to understand the structural complexity of the layered-spinel composite materials, various techniques such as XRD, XAS, and NMR have been used both for the pristine state and during first cycle.[74, 76] The electrochemical activities of the layered and spinel phases were confirmed with these techniques. However, the compositional variations of the layered and spinel phases in the composite samples have not been investigated; because of the same basic cubic close packed oxygen array, the actual composition and content of the layered and spinel phases in the composite could be different from the nominal composition and content. In addition, limited information is available on the structural and electrochemical characteristics during the extended cycling of these composite cathodes. In fact, these composite cathodes show a gradual increase in discharge capacity that is accompanied by significant changes in the charge/discharge profiles during extended electrochemical cycling, which is different from what is observed with either of the individual phases.

Accordingly, we present here the synthesis and characterization of the composite system $x\mathrm{Li[Li_{0.2}Mn_{0.6}Ni_{0.17}Co_{0.03}]O_2} - (1\text{-}x)\mathrm{Li[Mn_{1.5}Ni_{0.425}Co_{0.075}]O_4}$ ($0 \leq x \leq 1$),

consisting of the lithium-rich layered oxide $Li[Li_{0.2}Mn_{0.6}Ni_{0.17}Co_{0.03}]O_2$ (*i.e.* $0.6Li[Li_{1/3}Mn_{2/3}]O_2 - 0.4Li[Mn_{0.5}Ni_{0.425}Co_{0.075}]O_2$ solid solution) and the 5 V spinel oxide $Li[Mn_{1.5}Ni_{0.425}Co_{0.075}]O_4$. It should be noted that the Mn : Ni : Co ratio are nominally identical in the layered and spinel phases of the above composite cathodes. The high-capacity of the lithium-rich layered oxide is attributed to the irreversible loss of oxygen from the lattice during first charge, followed by a lowering of the oxidation state of the transition-metal ions at the end of first discharge.[44] A small amount of cobalt was added in our study as the cobalt ions are known to facilitate the oxygen loss from the lithium-rich layered phase due to an overlap of the $Co^{3+/4+}$:3d band with the top of the O^{2-}:2p band and thereby increase the discharge capacity.[120, 121] The unique structural characteristics of these layered-spinel composite cathodes and their effect on the electrochemical performances are investigated by a careful analysis of the ND data, XRD data, electrochemical charge-discharge profiles, and electrochemical differential-capacity measurements.

5.2 EXPERIMENTAL

5.2.1 Synthesis

The $xLi[Li_{0.2}Mn_{0.6}Ni_{0.17}Co_{0.03}]O_2 - (1-x)Li[Mn_{1.5}Ni_{0.425}Co_{0.075}]O_4$ ($0 \leq x \leq 1$) composite cathodes were synthesized by heating a required amount of mixed metal hydroxides (Mn : Ni : Co = 1 : 0.28 : 0.05) with lithium hydroxide at 800 ^oC for 6 h in air; a 3 wt. % excess lithium hydroxide was taken in the reaction mixture to compensate for lithium volatilization during the high temperature calcination process. The mixed metal hydroxide $Mn_{0.75}Ni_{0.2125}Co_{0.0375}(OH)_2$ was obtained by a co-precipitation method as described in Chapter 2. Figure 5.1 shows the five different compositions (x = 0, 0.25, 0.5, 0.75, and 1) investigated in the composite cathode system $xLi[Li_{0.2}Mn_{0.6}Ni_{0.17}Co_{0.03}]O_2 -$

(1-*x*)Li[$Mn_{1.5}Ni_{0.425}Co_{0.075}$]$O_4$. The five different compositions were prepared by controlling the lithium: mixed metal molar ratio in the reaction mixture as 0.5, 0.62, 0.79, 1.05, and 1.5, respectively, for the *x* = 0, 0.25, 0.5, 0.75, and 1 samples.

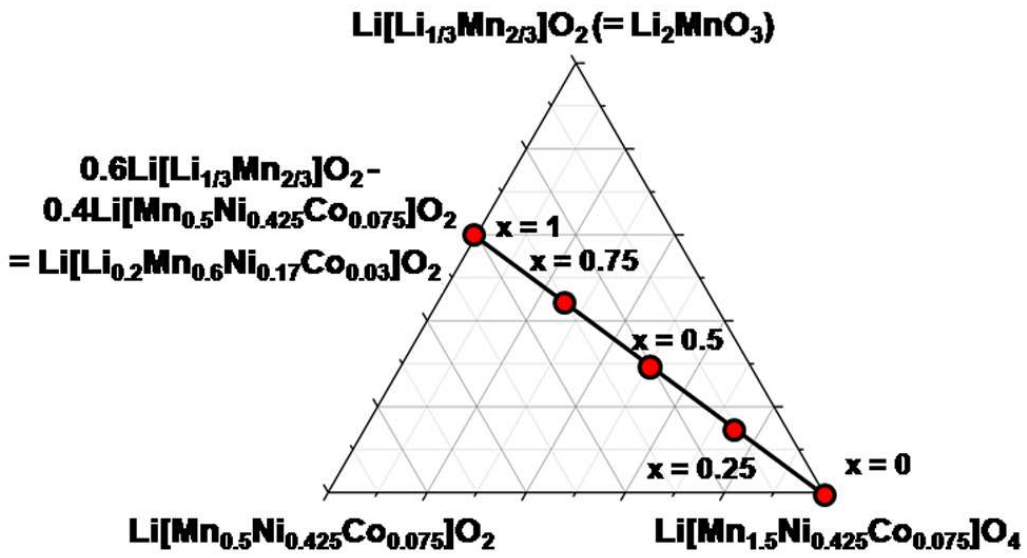

Figure 5.1. Compositional phase diagram of the *x*Li[$Li_{0.2}Mn_{0.6}Ni_{0.17}Co_{0.03}$]$O_2$ – (1-*x*) Li[$Mn_{1.5}Ni_{0.425}Co_{0.075}$]$O_4$ system.

5.2.2 Characterization

The Li, Mn, Ni, and Co molar ratios in the synthesized samples were analyzed with ICP-AES. ND measurements were carried out with the general purpose powder diffraction beamline POWGEN at the Spallation Neutron Source.[98] The samples were loaded in vanadium cans and the 24 sample changer was used to collect the room-temperature patterns at wavelengths of 1.066 and 2.665 Å, which cover a d spacing range of 0.3 to 6.2 Å. XRD data were collected with a Rigaku Ultima-IV system (Cu Kα

radiation). The structural characterization of all the five pristine samples were carried out with both XRD and ND and a joint Rietveld refinement with the software package GSAS and the EXPGUI interface.[96, 97] The *ex-situ* XRD analyses were carried out as described in Chapter 3. Electrochemical properties of the layered-spinel composite cathodes were evaluated with 2032-type coin cells. The coin cells were assembled as described in Chapter 2.

5.3 RESULT AND DISCUSSION

5.3.1 Chemical and structural analysis

ICP-AES analysis data of the metal ion contents in the xLi[$Li_{0.2}Mn_{0.6}Ni_{0.17}Co_{0.03}$]$O_2$ − (1-x)Li[$Mn_{1.5}Ni_{0.425}Co_{0.075}$]$O_4$ composite cathodes with x = 0, 0.25, 0.5, 0.75, and 1.0 are shown in Table 5.1. The experimental ratios of Mn : Ni : Co in all the samples are in good agreement with the nominal value of 1 : 0.28 : 0.05. The experimental Li : (Mn,Ni,Co) molar ratios are slightly higher than the designed nominal value for most of the samples due to the addition of 3 wt. % excess LiOH during the synthesis.

Table 5.1 ICP-AES analysis results of Mn : Ni : Co and Li/[Mn + Ni + Co] ratios in the xLi[$Li_{0.2}Mn_{0.6}Ni_{0.17}Co_{0.03}$]$O_2$ − (1-x)Li[$Mn_{1.5}Ni_{0.425}Co_{0.075}$]$O_4$ (x = 0, 0.25, 0.5, 0.75, and 1) composite cathodes

x	Mn : Ni : Co	Li / [Mn+Ni+Co]	
		Nominal	Experimental
0	1 : 0.29 : 0.05	0.50	0.55
0.25	1 : 0.28 : 0.05	0.62	0.65
0.5	1 : 0.28 : 0.05	0.79	0.82
0.75	1 : 0.28 : 0.05	1.05	1.04
1	1 : 0.28 : 0.05	1.50	1.58

Selected segments of the XRD and ND patterns of the pristine xLi[$Li_{0.2}Mn_{0.6}Ni_{0.17}Co_{0.03}$]$O_2$ − (1-x)Li[$Mn_{1.5}Ni_{0.425}Co_{0.075}$]$O_4$ (x = 0, 0.25, 0.5, 0.75, and 1) composite cathodes prepared at 800 °C are shown in Figure 5.2. As a representative example, the joint XRD and ND Rietveld refinement results for the x = 0.5 sample are summarized in Figure 5.3 to show the quality of the refinement result. The lattice parameter values obtained are summarized in Table 5.2. The XRD pattern of the x = 0 end member Li[$Mn_{1.5}Ni_{0.425}Co_{0.075}$]$O_4$ fits well with the cubic spinel phase (Fd-3m). Although an ordered spinel structure with the space group $P4_332$, in which the Mn^{4+} and Ni^{2+} ions are ordered in the 16d octahedral sites, is generally formed for the Li[$Mn_{1.5}Ni_{0.5}$]O_4 composition, the presence of Co in the Li[$Mn_{1.5}Ni_{0.425}Co_{0.075}$]$O_4$ composition suppresses the ordering and a disordered spinel phase with the space group Fd-3m is formed as revealed by the absence of any superstructure reflections.[104-106] Moreover, the $Li_xNi_{1-x}O$ impurity phases is often observed with the synthesis of

$Li[Mn_{1.5}Ni_{0.5}]O_4$,[31, 32, 70] but no reflections corresponding to $Li_xNi_{1-x}O$ are seen with our x = 0 sample containing a small amount of Co. However, a trace amount of the layered phase is detected in the x = 0 composition due to the slightly higher lithium content taken in the reaction mixture.

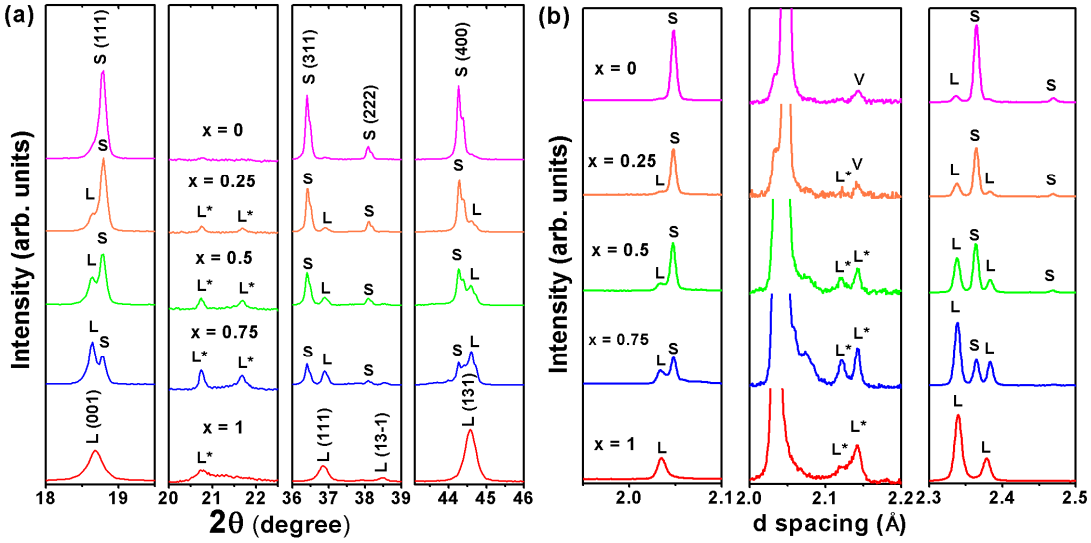

Figure 5.2. Selected portions of (a) XRD and (b) ND patterns of the xLi[$Li_{0.2}Mn_{0.6}Ni_{0.17}Co_{0.03}$]$O_2$ – (1-x)Li[$Mn_{1.5}Ni_{0.425}Co_{0.075}$]$O_4$ (x = 0, 0.25, 0.5, 0.75, and 1) samples prepared at 800 ^oC to show the various phases present. S and L refer, respectively, to cubic spinel and layered phases. L* refers the superstructure reflections arising from an ordering among Li^+, Mn^{4+}, and Ni^{2+} in the layered phase. V refers to the reflection arising from the vanadium can used for the ND experiments.

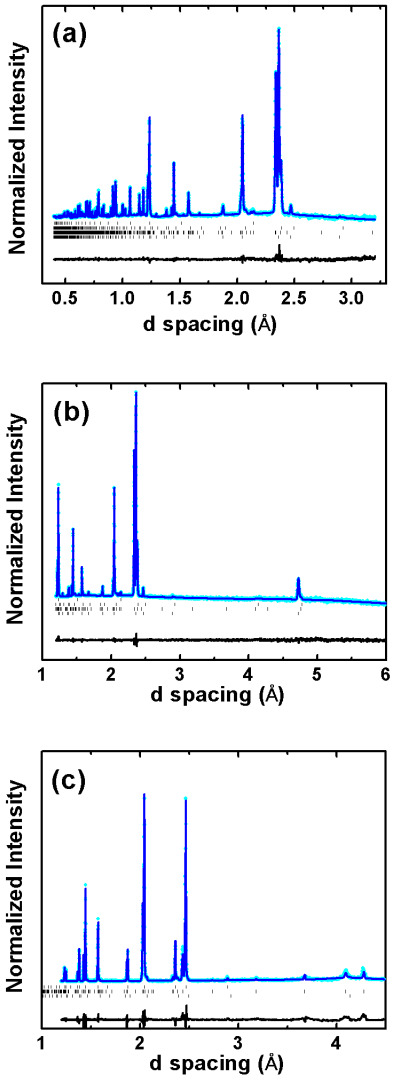

Figure 5.3. XRD and ND joint Rietveld refinement results of the $0.5Li[Li_{0.2}Mn_{0.6}Ni_{0.17}Co_{0.03}]O_2 - 0.5Li[Mn_{1.5}Ni_{0.425}Co_{0.075}]O_4$ sample (x = 0.5) prepared at 800^{o}C. Observed pattern is denoted by dots, and the calculated and difference plots are shown in solid lines. Peak markers for layered, cubic spinel, and cubic impurity phase are included. Also included in the neutron pattern are markers for V from the sample can. (a), (b), and (c) are showing refinements of neutron data collected, respectively, using center wavelengths 1.066 and 2.665 Å and X-ray data.

Table 5.2 Lattice parameters of the layered, spinel, and cubic impurity phases in the xLi[$Li_{0.2}Mn_{0.6}Ni_{0.17}Co_{0.03}$]$O_2$ – (1-x)Li[$Mn_{1.5}Ni_{0.425}Co_{0.075}$]$O_4$ (x = 0, 0.25, 0.5, 0.75, and 1) composite cathodes.

x	Spinel (*Fd*-3*m*)	Layered (*C*2/*m*)				Cubic Impurity	R Factor
	a (Å)	a (Å)	b (Å)	c (Å)	β	a (Å)	R_{wp} (%)
0	8.1801(1)	2.8507(1)		14.2778(8)	120		2.52
0.25	8.1783(1)	2.8524(2)	8.5539(3)	5.0440(2)	109.307(2)	8.2922(15)	1.27
0.5	8.1765(1)	2.8534(1)	8.5548(1)	5.0432(1)	109.296(1)	8.2754(6)	1.77
0.75	8.1784(1)	2.8530(2)	8.5574(1)	5.0434(1)	109.292(1)	8.2727(5)	2.47
1	8.1798(8)	2.8600(4)	8.5633(1)	5.0292(1)	109.171(3)		2.94

In the XRD pattern of the x = 1 end member Li[$Li_{0.2}Mn_{0.6}Ni_{0.17}Co_{0.03}$]$O_2$, a few weak and broad reflections appear in the 2θ range of 20.5 – 22.5 ° (see Figure 5.2(a)) due to the ordering of the excess lithium ions in the transition metal layer of Li[$Li_{0.2}Mn_{0.6}Ni_{0.17}Co_{0.03}$]$O_2$.[40, 122, 123,124-128] A combined XRD and transmission electron microscopy (TEM) analysis has shown recently that the lithium-rich layered oxide Li[$Li_{0.2}Mn_{0.6}Ni_{0.2}$]O_2 is a single-phase solid solution with C2/m monoclinic symmetry and multiple planar defects.[128] Accordingly, the x = 1 end member Li[$Li_{0.2}Mn_{0.6}Ni_{0.17}Co_{0.03}$]$O_2$ was fitted with the *C*2/*m* Li_2MnO_3 type structure. For the intermediate compositions with x = 0.25, 0.5, and 0.75, both XRD and ND patterns show reflections corresponding to layered and the spinel phases. The intensities of the reflections corresponding to the layered phase increase at the expense of the reflections of the spinel phase as the x value increases. Most notably, the two superstructure reflections

in the 2θ range of 20.5 – 22.5° appear more clearly in the composite samples (x = 0.25, 0.5, and 0.75) compared to that in the x = 1 sample. The sharp superstructure reflections in the composite samples suggest a greater number of lithium ions in the transition metal layer[129, 130] than that expected based on the nominal composition. The details of the compositional variations in the layered phase that was obtained by the combined ND and XRD data are discussed below.

Due to the presence of multiple transition metal ions (Mn, Co and Ni), which have similar X-ray scattering factors due to their close atomic numbers, and the low X-ray scattering factor of Li, it is not possible to independently refine the occupancy of the various ions with the XRD data alone. However, the occupancy could be refined with the combined XRD and ND data as the ND scattering power of the various ions involved differ significantly: Li: -1.9, Mn: -3.73, Co: 2.49, and Ni: 10.3. For the x = 0 sample, a small fraction of layered phase is observed as mentioned earlier, which could be fitted with the rhombohedral (*R*-3*m)* symmetry. No superstructure reflections are observed in ND data similar to that in the XRD data. Superstructure reflections are, however, observed in the ND patterns of all the other compositions, with the strongest ordering present in the x = 0.5 and 0.75 samples. For the x = 1 sample, a very small fraction (~ 3.9 wt. %) of the spinel phase is present. Due to the presence of small amounts of secondary phases in the two end members (x = 0 and x = 1), the compositions could not be refined, so they were fixed to the nominal expected value. For the x = 0.25, 0.5, and 0.75 samples, a cubic impurity phase is observed in the ND data. A close inspection of the location of the peaks reveal that this impurity could not be indexed with the cubic $Li_xNi_{1-x}O$ rock salt phase, which has a lattice parameter of 4.14 Å and is often present as an impurity phase with the synthesis of the x = 0 member.[76] Instead, the cubic impurity phase could be fitted as a Ni_6MnO_8 phase,[107] which has a lattice parameter of ~ 8.3 Å, because of the peak at

4.14 Å in the ND pattern. The lattice parameters of this impurity phase are listed in Table 5.2.

With the combined ND and XRD data, the layered phase in the x = 0.25, 0.5, 0.75, and 1 samples could be fitted with the $C2/m$ Li_2MnO_3 type structure.[126] The details of the compositions thus obtained and the lattice parameters of the layered phase in all the five samples are listed in Table 5.2 and Table 5.3. The 2c and 4h sites are almost entirely occupied by Li while Mn shows a clear preference for the 4g site and Ni prefers the larger 2b site, which is in agreement with the previous work.[126] The overall residuals R_{wp} values are listed in Table 5.2, which attests to the good quality of the fit to the data. It should be mentioned here that some constraints had to be applied to the site occupancies so that each site is fully occupied, *e.g.*, full occupancy of the oxygen sites is assumed for both the spinel and layered phases.

Based on the obtained compositions in Table 5.3, we can see the compositional variations of each phase in the composite samples (x = 0.25, 0.5, and 0.75) compared to the nominal compositions due to the presence of the cubic impurity phase. It should be noted that the lithium contents in the layered phase present in the x = 0.5 and 0.75 samples are much higher than that in the x = 1 sample. The higher lithium contents in the x = 0.5 and 0.75 samples lead to strong superstructure reflections due to a better ordering of the lithium ions in the transition metal layer of the layered structure; the Li_2MnO_3 type ordering requires an ideal Li : transition metal ratio of 1:2 in the transition metal layer, so a total lithium content > 1.2 in the layered phase enhances the ordering.

Table 5.3 The refined chemical compositions and weight percent of the layered, spinel, and cubic impurity phases in the xLi[$Li_{0.2}Mn_{0.6}Ni_{0.17}Co_{0.03}$]$O_2$ – (1-x)Li[$Mn_{1.5}Ni_{0.425}Co_{0.075}$]$O_4$ (x = 0, 0.25, 0.5, 0.75, and 1) composite cathodes.

x	Chemical composition			Weight %			Li / [Mn+Ni+Co]
	Atom	Spinel (*Fd*-3*m*)	Layered (*C*2/*m*)	Spinel (*Fd*-3*m*)	Layered (*C*2/*m*)	Cubic	
0	Li	1	1.20	89.67	10.54		0.59
	Mn	1.5000(9)	0.60				
	Ni	0.3750(9)	0.17				
	Co	0.1235(9)	0.03				
0.25	Li	1	1.19(2)	81.34	18.28	0.40	0.69
	Mn	1.500(1)	0.67(2)				
	Ni	0.402(1)	0.05(1)				
	Co	0.099(1)	0.01(1)				
0.50	Li	1	1.26(1)	63.86	34.86	1.30	0.93
	Mn	1.500(1)	0.60(1)				
	Ni	0.441(1)	0.051(5)				
	Co	0.059(1)	0.005(5)				
0.75	Li	1	1.31(1)	37.26	59.59	3.1	1.05
	Mn	1.500(2)	0.56(1)				
	Ni	0.489(2)	0.046(4)				
	Co	0.011(2)	0.012(4)				
1.00	Li	1	1.185(2)	3.89	96.11		1.64
	Mn	1.5	0.620(2)				
	Ni	0.425	0.115(5)				
	Co	0.075	0.006(5)				

5.3.2 First cycle charge-discharge profiles

The first cycle charge-discharge profiles of the xLi[$Li_{0.2}Mn_{0.6}Ni_{0.17}Co_{0.03}$]$O_2$ – (1-x)Li[$Mn_{1.5}Ni_{0.425}Co_{0.075}$]$O_4$ composite cathodes (x = 0, 0.25, 0.5, 0.75, and 1) between 2 and 5 V at 10 mA/g (~ C/25 rate assuming a capacity of ~ 250 mAh/g) are shown in Figure 5.4. As seen in Chapter 3, the spinel Li[$Mn_{1.5}Ni_{0.425}Co_{0.075}$]$O_4$ phase (x = 0) clearly shows five distinctive plateau regions during discharge (Figure 5.4(a)). The three plateau regions, two at ~ 4.7 V and one at ~ 4.0 V, originate from the extraction/insertion of lithium ions from/into the 8a tetrahedral sites of the cubic spinel structure. Among them, the upper plateau region at ~ 4.7 V originate from the Ni^{3+}/Ni^{4+} couple, the lower plateau region at ~ 4.7 V originate from the Ni^{2+}/Ni^{3+} couple, and the plateau region at ~ 4.0 V originates from the Mn^{3+}/Mn^{4+} couple because the spinel phase generally consists of a small amount of Mn^{3+} ions.[31, 32, 104] The two remaining plateau regions at ~ 2.7 and ~ 2.1 V are associated with the extraction/insertion of lithium ions from/into the empty 16c octahedral site of the cubic spinel structure, which is accompanied by a cubic to tetragonal phases transition involving Jahn-Teller distortion.[67-69, 110]

For x = 1, the lithium-rich layered Li[$Li_{0.2}Mn_{0.6}Ni_{0.17}Co_{0.03}$]$O_2$ shows distinctly different first charge and discharge profiles (Figure 5.4(e)) as known in the literature.[55] The first charge profile can be divided into two regions: the sloping (OCV to ~ 4.5 V) and the plateau (4.5 to 5 V) regions. In the sloping region, the voltage increases up to ~ 4.5 V, which is accompanied by an oxidation of the transition metal ions to 4+ state.[42, 43] The plateau region at 4.5 to 5 V corresponds to the oxidation of O^{2-} ions to O and the extraction of lithium ions from the lattice in the form of Li_2O.[44, 131-133] During the first discharge, the voltage profile shows a sloping characteristic, involving the insertion of

lithium ions and the corresponding reduction of the transition metal ions from the 4+ state.[55]

The charge-discharge profiles of the composite cathodes xLi[$Li_{0.2}Mn_{0.6}Ni_{0.17}Co_{0.03}$]$O_2$ – (1-x)Li[$Mn_{1.5}Ni_{0.425}Co_{0.075}$]$O_4$ with x = 0.25, 0.5, and 0.75 show both the spinel and layered oxide characteristics (Figure 5.4(b) – 5.4(d)). As x increases, the capacity from the layered oxide phase (sloping region at 3 to 4 V) increases, while the capacity of the spinel oxide phase (the five plateau regions at ~ 4.7, 4.0, 2.7, and 2.1 V) decreases. Interestingly, the capacities of the layered oxide phase in these composite cathodes are much lower than what is expected for the layered oxide phase, while the capacities of the spinel oxide phase are slightly higher than what is expected for the nominal composition. Due to the decrease in the intrinsic capacity of the layered oxide phase in the composite cathode with increasing x, the overall discharge capacity of the composite cathode decreases with increasing x. The lower capacity of the layered oxide phase in the composite cathode could be due to the presence of more lithium ions in the transition metal layer than that expected based on the nominal composition.[129, 130] The capacity of the lithium-rich layered oxide is sensitive to the lithium content in the transition metal layer.[120] First-principles calculations have shown that the lithium ions in the transition metal layer migrate into the tetrahedral site and forms a Li-Li dumbbell during the charging process, which is accompanied by a migration of nickel ions from the transition metal layer to the lithium layer, *i.e.* increased interlayer mixing.[134] The lithium ions in those tetrahedral sites are very stable, and higher than 5.0 V is needed to remove them from those tetrahedral sites. Also, the increased nickel ion content in the lithium layer due to increased interlayer mixing could interfere with the diffusion path of the lithium ions. Such higher nickel content in the lithium layer leads to a lowering of lithium diffusivity and consequently a lower capacity of the layered

oxide phase in the composite cathode (*i.e.* a lower electrochemical utilization of the layered oxide).

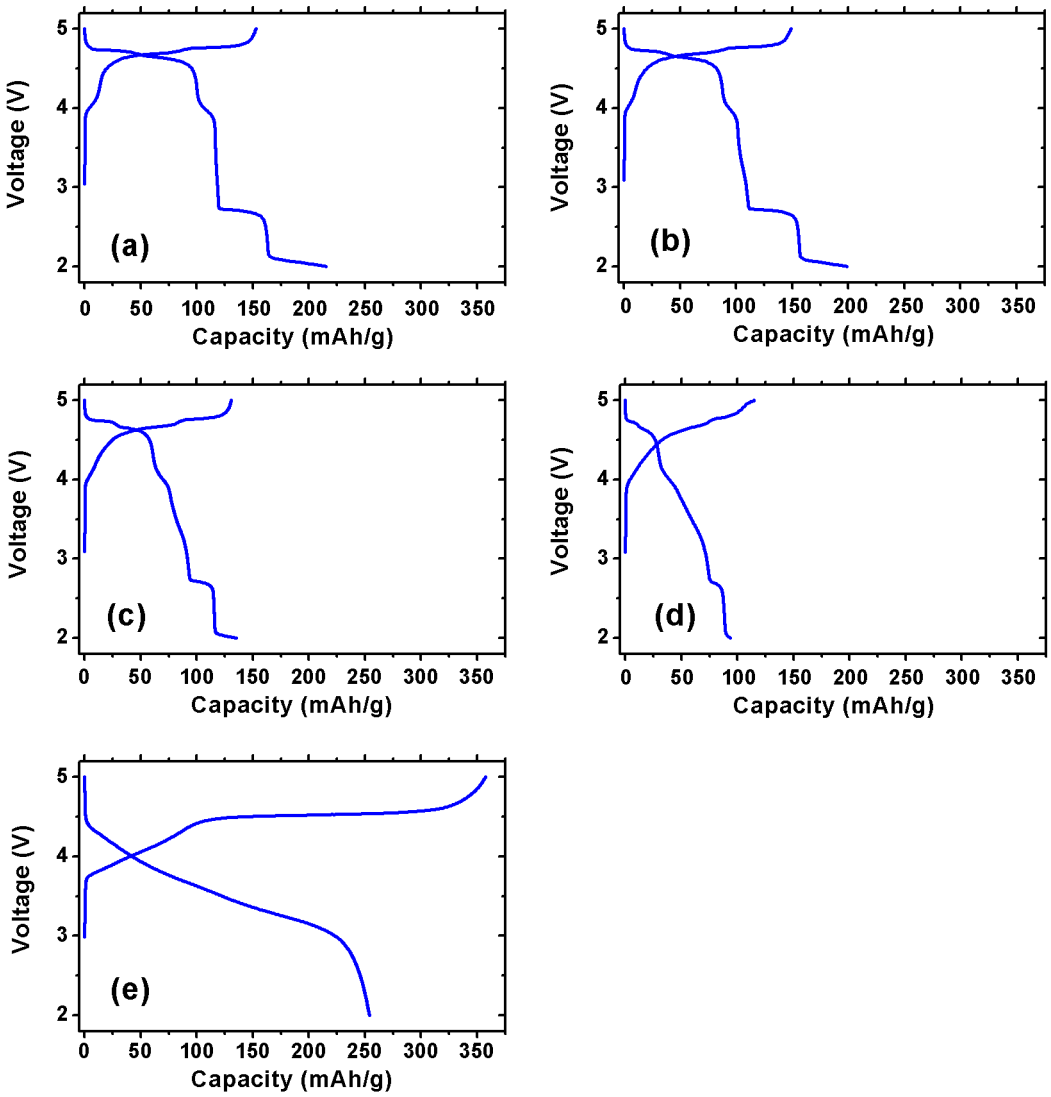

Figure 5.4. First charge-discharge profiles of xLi[$Li_{0.2}Mn_{0.6}Ni_{0.17}Co_{0.03}$]$O_2$ – (1-x)Li[$Mn_{1.5}Ni_{0.425}Co_{0.075}$]$O_4$ composite cathodes when cycled between 2 and 5 V at 10 mA/g (~ C/25 rate based on a capacity of ~ 250 mAh/g): (a) x = 0, (b) x = 0.25, (c) x = 0.5, (d) x = 0.75, and (e) x = 1.

5.3.3 Cyclability

Comparisons of the cyclability in terms of discharge capacity and discharge energy of the xLi[$Li_{0.2}Mn_{0.6}Ni_{0.17}Co_{0.03}$]$O_2$ – (1-x)Li[$Mn_{1.5}Ni_{0.425}Co_{0.075}$]$O_4$ (x = 0, 0.25, 0.5, 0.75, and 1) composite cathodes between 2 and 5 V at 10 mA/g are shown in Figure 5.5. The x = 0 sample (Li[$Mn_{1.5}Ni_{0.425}Co_{0.075}$]$O_4$ spinel) shows a relatively large discharge capacity (215 mAh/g in the first cycle), but exhibits inferior cyclability due to Jahn-Teller distortion accompanied by a large volume change when the lithium ions are inserted/extracted into/from the 16c octahedral sites. Detailed structural analysis results will be discussed later in the *ex*-situ XRD section. The x = 1 sample (layered Li[$Li_{0.2}Mn_{0.6}Ni_{0.17}Co_{0.03}$]$O_2$) shows a discharge capacity of 254 mAh/g in the first cycle, and the capacity retention becomes stable after an initial fade during the first 10 cycles. The x = 0.25 sample shows inferior cyclability like the x = 0 sample due to the presence of a relatively large fraction of the spinel phase. In contrast, both the x = 0.5 and 0.75 samples show a gradual increase in capacity during 50 cycles from a relatively low capacity values of, respectively, 135 and 95 mAh/g. The x = 0.5 and 0.75 samples show, 203 and 207 mAh/g, respectively, after 50 cycles. The reason for the continuously increasing capacity will be discussed in a later section.

The discharge energy density variation is similar to that of the discharge capacity, except for the x = 0.5 and 0.75 samples. The x = 0.5 sample displays a higher discharge energy density than the x = 0.75 sample at 50 cycle even though the x = 0.75 composition shows a slightly higher discharge capacity at the 50^{th} cycle. This is because of the relatively higher capacity of the x = 0.5 sample in the higher voltage (~ 4.7 V) plateau region. It is interesting to note that the discharge energy density of the x = 0.5 sample is

720 mWh/g, which is only slightly lower than that of the x = 1 (lithium-rich layered oxide) sample (761 mWh/g) at 50th cycle.

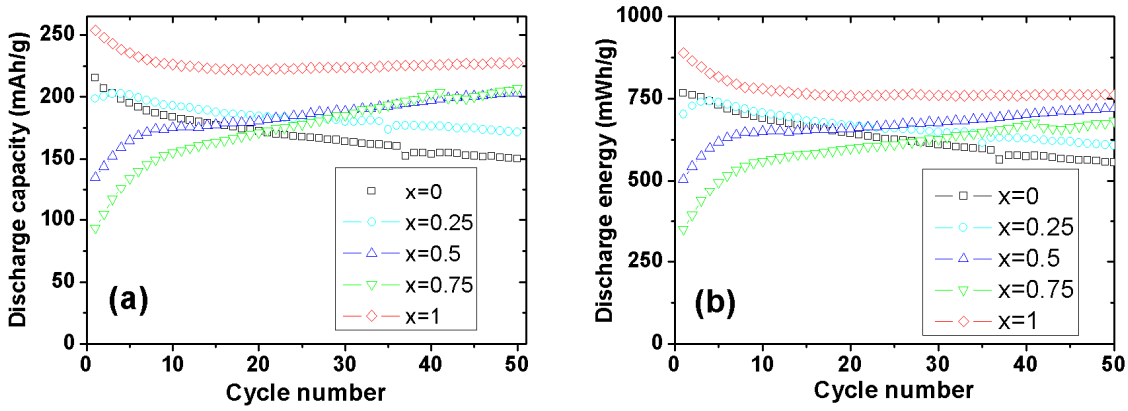

Figure 5.5. Cyclability data of the xLi[$Li_{0.2}Mn_{0.6}Ni_{0.17}Co_{0.03}$]$O_2$–(1-$x$) Li[$Mn_{1.5}Ni_{0.425}Co_{0.075}$]$O_4$ composite cathodes (x = 0, 0.25, 0.5, 0.75, and 1) during 50 cycles when cycled between 2 and 5 V at 10 mA/g: (a) discharge capacity and (b) discharge energy.

5.3.4 Coulombic Efficiency

Figure 5.6 compares the coulombic efficiencies of the xLi[$Li_{0.2}Mn_{0.6}Ni_{0.17}Co_{0.03}$]$O_2$ – (1-x)Li[$Mn_{1.5}Ni_{0.425}Co_{0.075}$]$O_4$ (x = 0, 0.25, 0.5, 0.75, and 1) composite cathodes during 50 cycles between 2 and 5 V at 10 mA/g. The first cycle coulombic efficiencies are 141, 133, 103, 82, and 71 % respectively, for the x = 0, 0.25, 0.5, 0.75, and 1 samples. The x = 0 sample (5 V spinel Li[$Mn_{1.5}Ni_{0.425}Co_{0.075}$]$O_4$) shows the highest coulombic efficiency of 141 % (> 100 %) since additional lithium ions inserted into the empty 16c octahedral sites of the spinel phase during discharge. On the other hand, the x = 1 sample (layered Li[$Li_{0.2}Mn_{0.6}Ni_{0.17}Co_{0.03}$]$O_2$) shows the lowest coulombic efficiency of 71 % due to the elimination of oxygen and lithium-ion vacancies at the end of the first charge and the consequent inability to insert all the lithium back into the layered lattice.[44, 48, 49, 52] All of the composite cathodes with x = 0.25, 0.5, and 0.75 show better coulombic efficiency than the layered oxide only composition (x = 1) since the lithium ions that could not be inserted back into the layered oxide could be inserted into the empty 16c octahedral sites of the spinel phase. After two cycles, all compositions show similar coulombic efficiencies up to 50 cycles. The data in Figure 5.6 reveals that the composite strategy is also beneficial for decreasing the large first cycle irreversible capacity loss associated with the lithium-rich layered oxide cathodes.

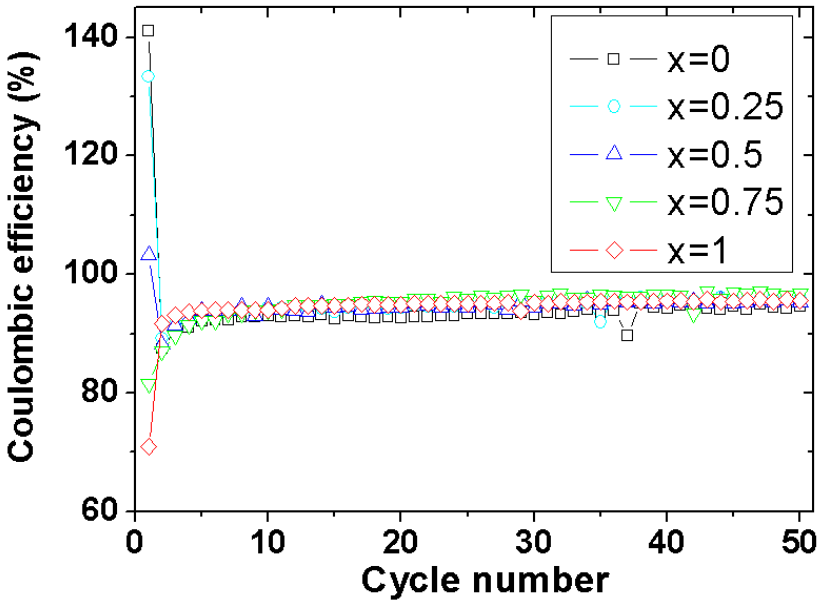

Figure 5.6. Variations of the coulombic efficiencies of the xLi[$Li_{0.2}Mn_{0.6}Ni_{0.17}Co_{0.03}$]$O_2$ – (1-x)Li[$Mn_{1.5}Ni_{0.425}Co_{0.075}$]$O_4$ composite cathodes (x = 0, 0.25, 0.5, 0.75, and 1) during 50 cycles when cycled between 2 and 5 V at 10 mA/g.

5.3.5 Charge-discharge & differential capacity profile analyses during cycling

Figure 5.7 compares the charge-discharge profiles at the 1st, 2nd, 25th, and 50th cycles of the xLi[$Li_{0.2}Mn_{0.6}Ni_{0.17}Co_{0.03}$]$O_2$ – (1-x)Li[$Mn_{1.5}Ni_{0.425}Co_{0.075}$]$O_4$ (x = 0, 0.25, 0.5, 0.75, and 1) composite cathodes when cycled between 2 and 5 V at 10 mA/g, while Figure 5.8 compares the corresponding differential capacity (dQ/dV) plots. The x = 0 (5 V spinel Li[$Mn_{1.5}Ni_{0.425}Co_{0.075}$]$O_4$) sample continues to lose its capacity from the five distinctive plateau regions (at ~ 4.7, 4.0, 2.7 and 2.1 V) as the cycle number increases. Due to the large amount of spinel phase in the x = 0.25 sample, the variations of the charge-discharge profiles and the corresponding dQ/dV plots are similar to those of the x

= 0 sample. In addition to the 5 V spinel phase characteristics, the x = 0.25 sample shows an increase in the utilization of the layered phase during cycling, as evidenced by an increase in the capacity in the sloping region between 3.8 - 2.8 V at the 2nd cycle and 3.2 - 2.8 V at the 25th cycle. The increased sloping region gradually diminishes and disappears at the 50th cycle.

The x = 0.5 and 0.75 compositions show similar charge-discharge and dQ/dV profiles during 50 cycles. First, the discharge capacity in the sloping region at 3.8 - 2.8 V continuously increases due to the increase in the utilization of the layered phase. The stiffness of the sloping region decreases as the cycle number increases and finally becomes similar to that for the ~ 3 V plateau region at the 50th cycle. The dQ/dV plots in Figure 5.8 also show that the broad peaks at 3.8 - 2.8V at the 2nd cycle change to larger area broad peaks at 3.5 - 2.8 V at the 25th cycle and finally change to relatively sharp peaks at 3.0 V. These results suggest that in the x = 0.5 and 0.75 samples, the layered phase continuously changes to other phases as the cycle number increases. Second, the 5 V spinel phase maintains its capacity without any fade during 50 cycles. The five distinctive plateau regions (at ~ 4.7, 4.0, 2.7, and 2.1 V) that originated from the 5 V spinel phase did not decrease during 50 cycles. This suggests that the 5 V spinel phase ($Li[Mn_{1.5}Ni_{0.425}Co_{0.075}]O_4$) is stable during cycling. From the foregoing electrochemical data, we conclude that the lithium-rich layered oxide phase in the composite cathodes undergoes phase transformation during cycling and the 5 V spinel phase in the composite cathode exhibits remarkable cyclability in a wide voltage range of 2 – 5 V despite the occurrence of Jahn-Teller (cubic to tetragonal) distortion. In order to develop a better understanding of the phase transformation of the layered phase and the superior cycle life of the spinel phase, *ex-situ* XRD data were collected for the x = 0, 0.25, 0.5, and 0.75 samples, and the results are presented in the section below.

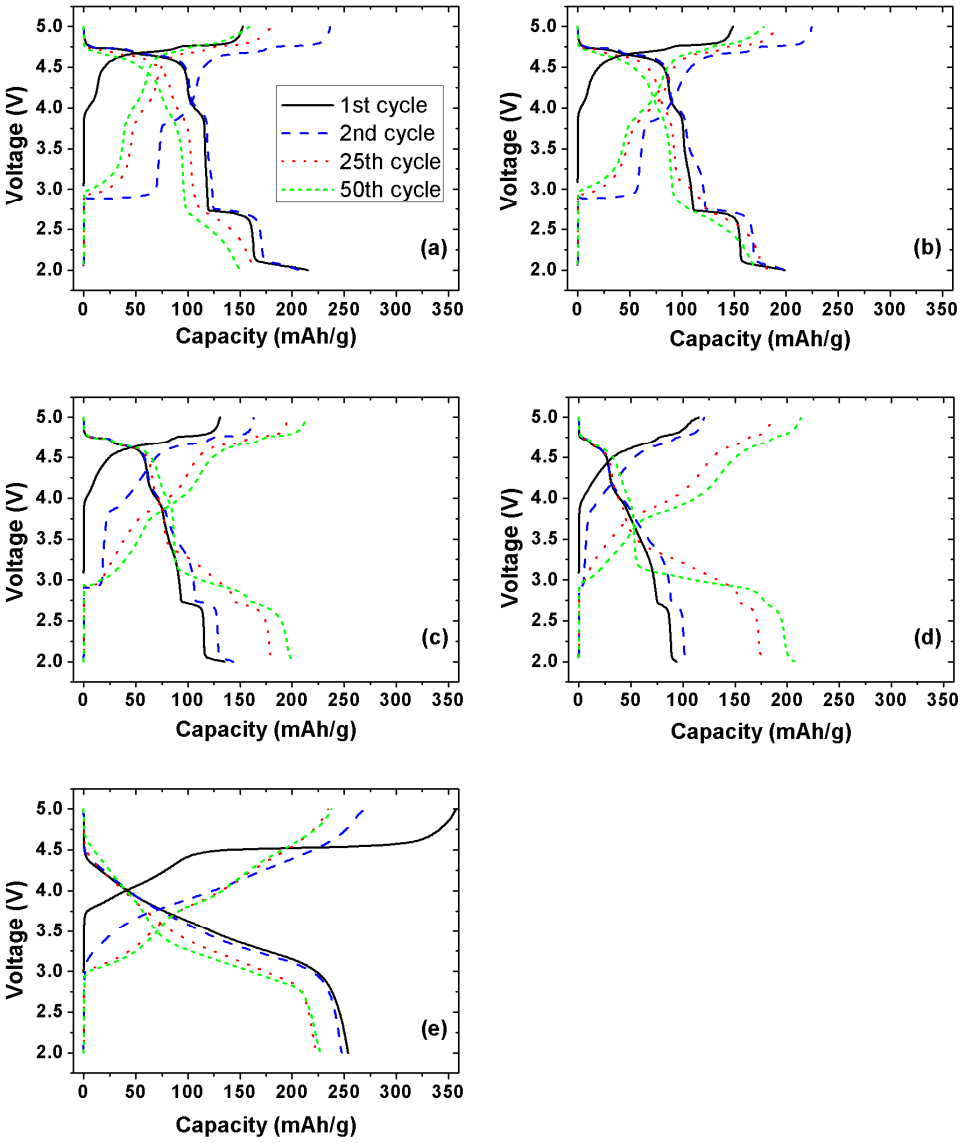

Figure 5.7. Charge-discharge profiles at 1st, 2nd, 25th, and 50th cycles of the xLi[$Li_{0.2}Mn_{0.6}Ni_{0.17}Co_{0.03}$]$O_2$ − (1-x)Li[$Mn_{1.5}Ni_{0.425}Co_{0.075}$]$O_4$ composite cathodes when cycled between 2 and 5 V at 10 mA/g: (a) x = 0, (b) x = 0.25, (c) x = 0.5, (d) x = 0.75, and (e) x = 1.

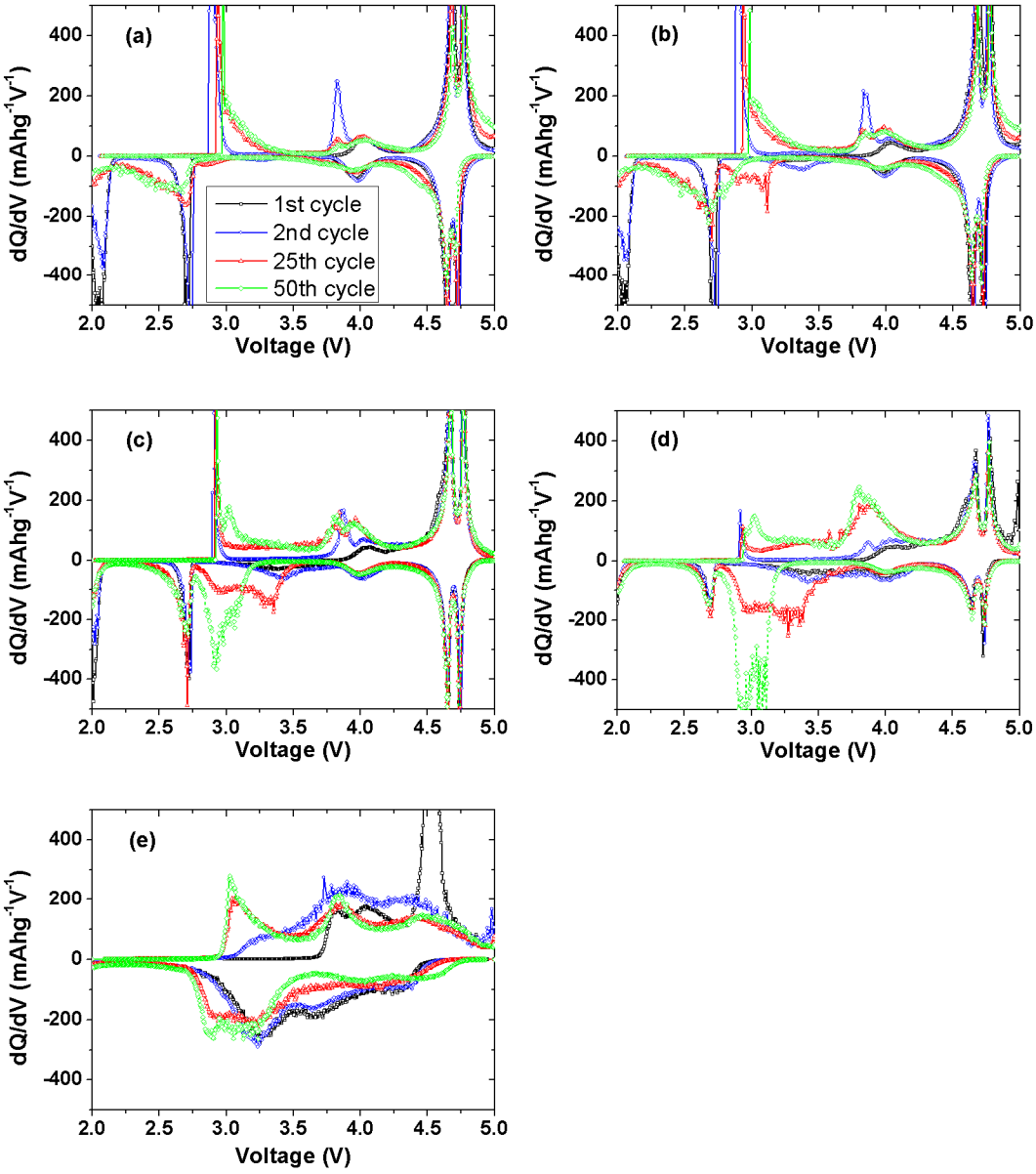

Figure 5.8. Differential capacity (dQ/dV) plots at 1st, 2nd, 25th, and 50th cycles of the xLi[$Li_{0.2}Mn_{0.6}Ni_{0.17}Co_{0.03}$]$O_2$ – (1-x)Li[$Mn_{1.5}Ni_{0.425}Co_{0.075}$]$O_4$ composite cathodes when cycled between 2 and 5 V at 10 mA/g: (a) x = 0, (b) x = 0.25, (c) x = 0.5, (d) x = 0.75, and (e) x = 1.

5.3.6 *Ex-situ* XRD data analysis

Figure 5.9 shows the XRD patterns of the x = 0 sample (5 V spinel $Li[Mn_{1.5}Ni_{0.425}Co_{0.075}]O_4$) before and after the first charge-discharge cycle. As described in Chapter 3, the intensities of the (111), (311), (222), and (400) reflections of the spinel phase (*Fd*-3*m*) are reduced or disappear after the first charge-discharge cycle with the evolution of two new tetragonal phases (T1 and T2) with the space group $I4_1/amd$. The lattice parameters of these T1 and T2 phases are given in Table 5.4. In order to compare the lattice parameter values before and after the first charge-discharge cycle, the lattice parameter of the pristine cubic spinel phase (*Fd*-3*m*) is also expressed in terms of the tetragonal phase ($I4_1/amd$) by the relation, $a_T = a_C/\sqrt{2}$ and $c_T = a_C$, where *T* and *C* refer, respectively, to tetragonal and cubic structures.[67] As revealed in Chapter 3, the inferior cyclability of the x = 0 sample (5 V spinel $Li[Mn_{1.5}Ni_{0.425}Co_{0.075}]O_4$) in Figure 5.5 is due to this large volume and c/a ratio changes associated with the cubic to tetragonal transition, especially during the cubic to tetragonal 2 transition. When the local stress induced by the volume change exceeds certain elastic limit of the matrix, cracks arise and the particles become electrochemically isolated.[135]

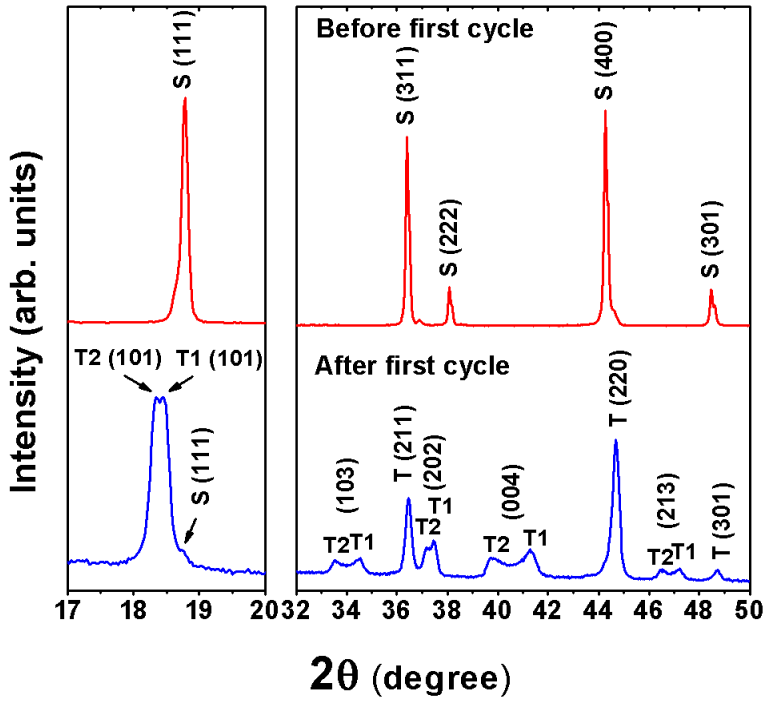

Figure 5.9. XRD data of the $Li[Mn_{1.5}Ni_{0.425}Co_{0.075}]O_4$ sample (before and after the first cycle). S and T refer, respectively, to the cubic spinel and tetragonal spinel phases.

Figure 5.10 shows the XRD patterns of the x = 0.25 sample in the $xLi[Li_{0.2}Mn_{0.6}Ni_{0.17}Co_{0.03}]O_2 - (1\text{-}x)Li[Mn_{1.5}Ni_{0.425}Co_{0.075}]O_4$ composite cathode system before and after the first charge-discharge cycle. Similar to that found with the x = 0 sample, the intensities of the reflections corresponding to the cubic spinel phase (*Fd*-3*m*) decrease and two new tetragonal phases T1 and T2 ($I4_1/amd$) evolve. On the other hand, the reflections corresponding to the layered phase remain without much change. The lattice parameters of each of the four phases are given in Table 5.4. Similar to that found with the x = 0 sample, the a_T and c_T parameters and the unit cell volume of the cubic spinel phase remain unchanged after the first charge-discharge cycle. Similarly, the T1

and T2 tetragonal phases ($I4_1/amd$) have smaller a_T parameter, larger c_T parameter, and larger unit cell volume (4.1 and 8.6 % volume increase, respectively, for the T1 and T2 phases) compared to the cubic spinel phase (Fd-3m). The inferior cyclability seen in Figure 5.5 is due to this large volume and c/a ratio changes associated with the cubic to tetragonal transition, especially during the cubic to tetragonal 2 transition similar to that found with the x = 0 sample.

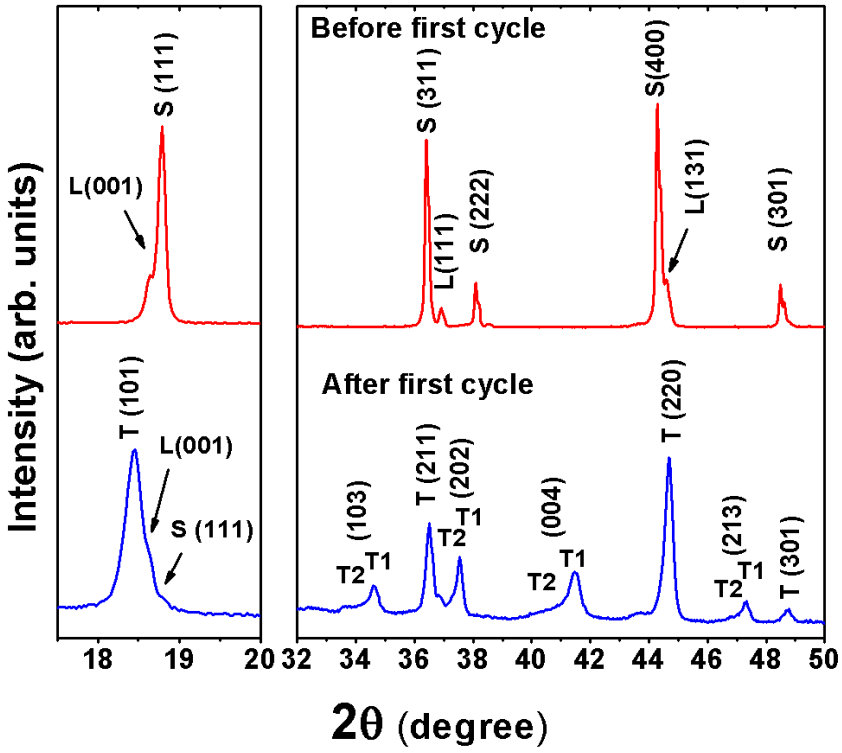

Figure 5.10. XRD data of the 0.25Li[$Li_{0.2}Mn_{0.6}Ni_{0.17}Co_{0.03}$]$O_2$ – 0.75Li[$Mn_{1.5}Ni_{0.425}Co_{0.075}$]$O_4$ sample (before and after the first cycle). L, S, and T refer, respectively, to layered, cubic spinel, and tetragonal spinel phases.

Table 5.4. Lattice parameters of the layered, spinel, and tetragonal phases in the xLi[$Li_{0.2}Mn_{0.6}Ni_{0.17}Co_{0.03}$]$O_2$ − (1-x)Li[$Mn_{1.5}Ni_{0.425}Co_{0.075}$]$O_4$ composite cathodes with various x values (x = 0, 0.25, 0.5, 0.75, and 1) before and after the charge-discharge cycles.

Sample		Spinel (*Fd*-3*m*)			Tetragonal 1 ($I4_1/amd$)			Tetragonal 2 ($I4_1/amd$)			Layered (*C*2/*m*)			
		a_T (Å)	c_T (Å)	V (Å^3)	a_T (Å)	c_T (Å)	V (Å^3)	a_T (Å)	c_T (Å)	V (Å^3)	a (Å)	b (Å)	c (Å)	V (Å^3)
x = 0	Pristine	5.7842(1)	8.1801(1)	274										
	After 1st cycle	5.7842(1)	8.1801(1)	274	5.7365(5)	8.7472(10)	288	5.7356(6)	9.0270(15)	297				
x = 0.25	Pristine	5.7829(1)	8.1783(1)	274							4.9422(2)	8.5539(3)	5.0440(2)	201
	After 1st cycle	5.7829(1)	8.1783(1)	274	5.7247(3)	8.6904(7)	285	5.7356(6)	9.0270(15)	297	4.9580(10)	8.6330(19)	5.0340(8)	203
x = 0.5	Pristine	5.7817(1)	8.1765(1)	273							4.9421(1)	8.5548(1)	5.0432(1)	201
	After 1st cycle	5.7749(7)	8.1670(10)	272	5.7431(2)	8.6862(5)	286				5.0412(9)	8.5103(12)	5.0444(7)	204
	After 25th cycle	5.7817(1)	8.1766(2)	273	5.7504(6)	8.6886(11)	287		Not detected		4.9404(3)	8.5400(5)	5.0798(6)	202
	After 50th cycle	5.7814(1)	8.1761(1)	273	5.7335(7)	8.6933(17)	286					Not detected		
x = 0.75	Pristine	5.7830(1)	8.1784(1)	274							4.9433(1)	8.5574(1)	5.0434(1)	201
	After 1st cycle	5.7825(5)	8.1777(7)	273	5.7600(5)	8.6806(12)	288				4.9538(8)	8.5674(10)	5.0487(7)	202
	After 25th cycle	5.7831(2)	8.1786(3)	274	5.7505(3)	8.6692(8)	287		Not detected		4.9265(8)	8.6791(12)	5.0065(7)	202
	After 50th cycle	5.7812(2)	8.1758(3)	273	5.7500(5)	8.6562(15)	286					Not detected		

Figure 5.11 shows the XRD patterns of the x = 0.5 sample in the xLi[$Li_{0.2}Mn_{0.6}Ni_{0.17}Co_{0.03}$]$O_2$ – (1-x)Li[$Mn_{1.5}Ni_{0.425}Co_{0.075}$]$O_4$ composite cathode system before the first cycle and after the first, 25th, and 50th cycles. After the first cycle, reflections due to the new tetragonal phase ($I4_1/amd$) appear in addition to the presence of the cubic spinel phase similar to that seen with the x = 0 sample; however, only one tetragonal phase is detected. On the other hand, the reflections corresponding to the layered phase (*C2/m*) remain unchanged after the first cycle. Interestingly, after the 25th-cycle, the apparent intensities of the reflections corresponding to the layered phase (*C2/m*) have almost vanished, and the intensity ratio of the cubic to tetragonal spinel phase has increased. After the 50th-cycle, the reflections corresponding to the layered phase have completely disappeared, and only the reflections corresponding to the cubic spinel (*Fd*-3*m*) and the tetragonal spinel ($I4_1/amd$) phases are seen. It should be noted that the intensity ratio of the cubic to tetragonal spinel phase has increased further compared to that after the 25th cycle. In other words, the cubic spinel phase (*Fd*-3*m*) content is greater than the tetragonal phase ($I4_1/amd$) content in the x = 0.5 sample after the 50th-cycle.

In addition, the capacities in the ~ 2.7 and ~ 2.1 V plateau regions in Figure 5.7 and the corresponding peaks in Figure 5.8 that are related to the cubic to tetragonal transition of the spinel phase do not change significantly during cycling. This suggests that the increase in the intensity of the cubic spinel phase after 50 cycles is not due to the increase in the 5 V spinel (such as Li[$Mn_{1.5}Ni_{0.425}Co_{0.075}$]$O_4$) content, but due to the evolution of a new spinel phase from the layered phase. This is supported by the differential capacity (dQ/dV) profile analysis data, the decrease in the sloping region of the discharge profile with increasing cycle number, and the formation of finally a 3 V plateau region at the 50th cycle. In other words, the appearance of the 3 V plateau at

extended cycling is due to the newly formed spinel phase from the lithium-rich layered phase. We believe this newly formed spinel phase from the lithium-rich layered phase has an Mn oxidation state of 4+ similar to that in the $Li[Li_{1/3}Mn_{5/3}]O_4$ cubic spinel phase (*Fd*-3*m*), which is known to exhibit a 3 V plateau with good cyclability.[136] Furthermore, despite the cubic to tetragonal transition occurring with the 5 V spinel phase on cycling between 5 and 2 V, the capacities from the parent 5 V spinel phase occurring in the five plateau regions, ~ 4.7, 4.0, 2.7, and 2.1 V did not change much during 50 cycles in the x = 0.5 sample as seen in Figures 5.7(c) and 5.8(c).

The origin of the stability of the parent 5 V spinel phase (*Fd*-3*m*) during extended electrochemical cycling can be explained by the relatively smaller discharge capacity in the ~ 2.7 and 2.1 V plateaus (lithium ion insertion into 16c octahedral sites) compared to those in the x = 0 and x = 0.25 samples. In the x = 0 and x = 0.25 samples, the capacity ratios of the 5 V spinel phase between the lithium ion insertion into the 8a tetrahedral sites (~ 4.7 and ~ 4 V) and lithium ion insertion into the 16c octahedral sites (~ 2.7 and ~ 2 V) are about 1 : 0.85. However, that capacity ratio in the x = 0.5 sample is about 1 : 0.55. According to *ex-situ* XRD data in Chapter 3, the ~ 2.7 and 2.1 V plateaus are related to the cubic to tetragonal phases transition, which encounter drastic changes in cell volume and *c/a* ratio. Therefore, the parent 5 V spinel in the x = 0.5 sample shows better phase stability than that in the x = 0 and x = 0.25 samples during cycling.

The changes in the lattice parameters with cycle number were assessed for the x = 0.5 sample. The lattice parameter values of each of the three phases before the first cycle and after the first, 25^{th}, and 50^{th} cycles are given in Table 5.4. For the cubic spinel phase (*Fd*-3*m*), the unit cell volumes remain virtually unchanged during the 50 cycles. The unit cell volume of the tetragonal phase ($I4_1/amd$) that evolved after the first cycle also remains unchanged during cycling (Table 5.4). The volume increase associated with the

cubic (*Fd*-3*m*) to the tetragonal ($I4_1/amd$) phase transition is 5.2, 5.5, and 4.9 %, respectively, after the first, 25th, and 50th cycles. In summary, both the stability of the newly evolved 3 V spinel-like phase from the lithium-rich layered phase as well as the stability of the 5 V spinel phase lead to superior cyclability, high energy density, and higher capacity for the x = 0.5 sample, despite a wide voltage range (2 – 5 V).

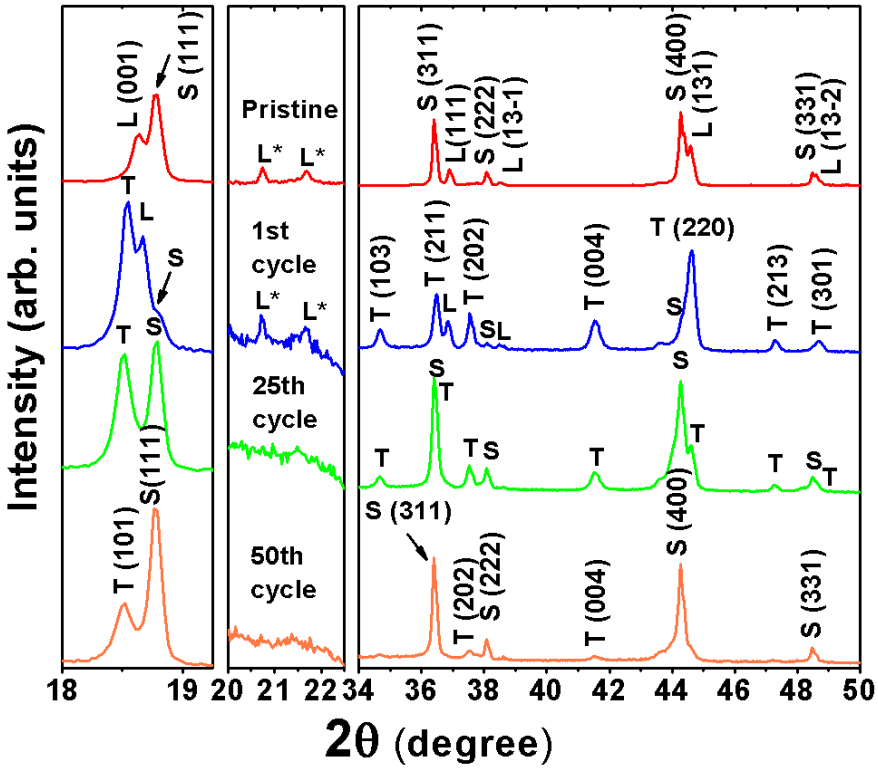

Figure 5.11. XRD data of the 0.5Li[$Li_{0.2}Mn_{0.6}Ni_{0.17}Co_{0.03}$]$O_2$ – 0.5Li[$Mn_{1.5}Ni_{0.425}Co_{0.075}$]$O_4$ sample (before cycling, after first cycle, after 25th cycle, and after 50th cycle). L, S, and T refer, respectively, to layered, cubic spinel, and tetragonal spinel phases. L* refer to the superstructure reflections arising from an ordering among Li^+, Mn^{4+}, and Ni^{2+} in the layered phase.

Figure 5.12 shows the XRD patterns of the x = 0.75 sample in the xLi[$Li_{0.2}Mn_{0.6}Ni_{0.17}Co_{0.03}$]$O_2$ – (1-x)Li[$Mn_{1.5}Ni_{0.425}Co_{0.075}$]$O_4$ composite cathode system before the first cycle and after the first, 25th, and 50th cycles. The behavior of the x = 0.75 phase is largely similar to that of the x = 0.5 phase, except the intensity ratio of the tetragonal phase to the cubic spinel phase is higher in the x = 0.75 sample. Similar to the x = 0.5 sample, the reflections corresponding to the layered phases have completely vanished and only the cubic spinel (*Fd*-3*m*) and the tetragonal ($I4_1/amd$) phases are present after the 50th cycle. The lattice parameter values before the first cycle and after the first, 25th, and 50th cycles are given in Table 5.4. For the cubic spinel phase (*Fd*-3*m*), the unit cell volumes remain virtually unchanged during the 50 cycles. For the tetragonal phase, the unit cell volume decreases slightly during 50 cycles (Table 5.4). Both the stability of the newly evolved 3 V spinel-like phase from the lithium-rich layered phase and the relative small capacity at ~ 2.7 and ~ 2.1 V plateaus, associated with the cubic to tetragonal transition of the 5 V spinel phase lead to superior cyclability in a wide voltage range (2 – 5 V) similar to that found with the x = 0.5 sample.

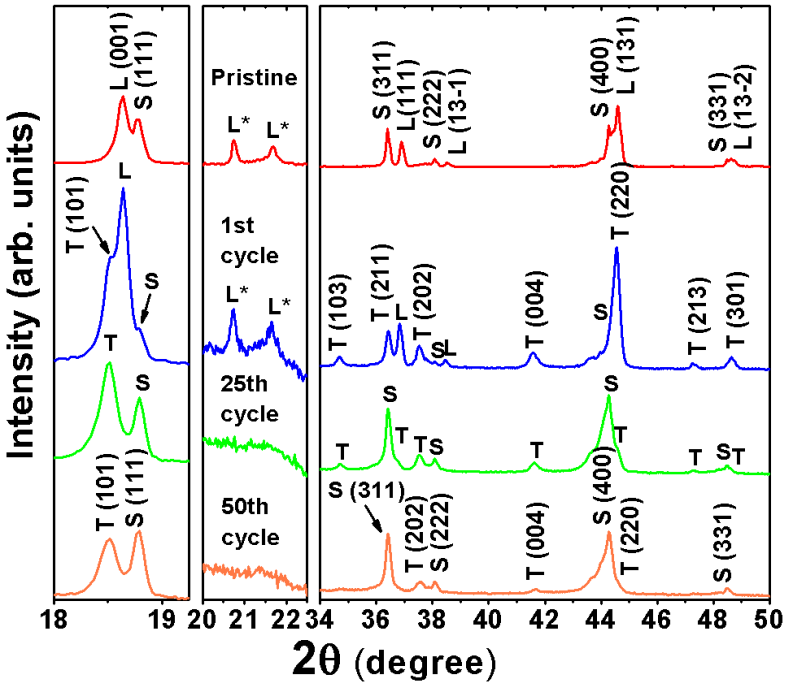

Figure 5.12. XRD data of the $0.75Li[Li_{0.2}Mn_{0.6}Ni_{0.17}Co_{0.03}]O_2 - 0.25Li[Mn_{1.5}Ni_{0.425}Co_{0.075}]O_4$ sample before cycling, after first cycle, after 25^{th} cycle, and after 50^{th} cycle. L, S, and T refer, respectively, to layered, cubic spinel, and tetragonal spinel phases. L* refer to the superstructure reflections arising from an ordering among Li^+, Mn^{4+}, and Ni^{2+} in the layered phase.

5.3.7 Structural transformation mechanisms of the composite cathodes

As discussed above, the evolution of the XRD, charge-discharge profile, and differential-capacity plot data suggests an irreversible transformation of the lithium-rich layered oxide phase (*C2/m*) in the composite cathode samples with x = 0.5 and 0.75 to a 3 V spinel-like phase (*Fd*-3*m*) during extended electrochemical cycling. The layered-to-spinel structural transformation is a well-known phenomenon for the layered $LiMnO_2$ system.[137-140] Typically, the spinel phase that evolves from the layered $LiMnO_2$ shows both the 4 V and 3 V plateau regions that are similar to those of typical $LiMn_2O_4$ spinel oxide. However, in our study here, the newly evolved spinel phase shows only a 3 V plateau. Although the transformation of a small portion of the lithium-rich layered oxide into a spinel-like phase has been suggested in the literature, a complete transformation of the lithium-rich layered phase has never been observed before.[45, 125, 132, 134, 141] The observations in our study raise two important questions: (i) why does the layered oxide phase (*C2/m*) in the composite environment (x = 0.5 and 0.75 samples) transform more easily to the spinel phase (*Fd*-3*m*) than that in the layered only composition (x = 1 sample) and (ii) why does the transformed spinel phase (*Fd*-3*m*) exhibit only a ~ 3 V plateau without any 4 V plateau? We address these questions below:

As discussed earlier, the combined ND and XRD Rietveld refinement results reveal that lithium ions have higher occupancy in the transition metal layer of the lithium-rich layered phase in the composite samples (x = 0.25. 0.5, and 0.75) compared to that in the layered oxide only sample (x = 1). Recently, Xu et al.[134] and Boulineau et al.[45] have reported that the surface of the lithium-rich layered oxides changes to a spinel-like structure during first charge. First-principles calculations have indicated that the lithium ions in the transition metal layer migrate into the tetrahedral sites and form Li-Li

dumbbells during the first charging process. The lithium ions in the tetrahedral site are very stable and are difficult to extract during electrochemical cycling conditions below 5 V. The lithium ions that remain in the tetrahedral sites and the transition metal ions that migrate into the lithium layer could facilitate the formation of a spinel-like phase with an extremely low energy. With first-principles calculation, Xu et al.[134] have suggested that the surface of the lithium-rich layered oxide $Li[Ni_{1/4}Li_{1/6}Mn_{7/12}]O_2$ changes into the lithium-rich spinel phase (*Fd*-3*m*) $Li[Li_{1/3}Ni_{1/2}Mn_{7/6}]O_4$, with part of the *16d* octahedral sites of the spinel phase occupied by lithium ions. In the $Li[Li_{1/3}Ni_{1/2}Mn_{7/6}]O_4$ composition, both the manganese and the nickel ions exist in the 4+ oxidation state. Accordingly, the lithium ions cannot be extracted from the $Li[Li_{1/3}Ni_{1/2}Mn_{7/6}]O_4$ spinel phase, implying the absence of a 4 and 5 V plateaus. On the other hand, the $Li[Li_{1/3}Ni_{1/2}Mn_{7/6}]O_4$ spinel phase can insert an additional lithium ion into the *16c* octahedral sites of the spinel lattice to form $Li_2[Li_{1/3}Ni_{1/2}Mn_{7/6}]O_4$, resulting in a 3 V plateau. This process is accompanied by a reduction of Ni^{4+} to Ni^{2+} while Mn^{4+} remains unchanged, and the lithiated $Li_2[Li_{1/3}Ni_{1/2}Mn_{7/6}]O_4$ is composed of Mn^{4+} and Ni^{2+} ions. As a result, $Li[Li_{1/3}Ni_{1/2}Mn_{7/6}]O_4$ does not suffer from Jahn-Teller distortion or Mn dissolution as the Mn^{4+} ions are stable during charge-discharge process.

Considering the higher occupancy of the transition metal layers by lithium ions in our composite samples with x = 0.5 and 0.75, it is possible that larger number of tetrahedral sites could be occupied by lithium ions during the extended electrochemical cycling of the composite cathodes compared to that with the layered only phase since the tetrahedral lithium ions originate from lithium migration from the transition metal layer. It is also possible that more nickel ions could be present in the lithium layer in the composite samples as the tetrahedral-site lithium ions are accompanied by a migration of nickel ions from the transition metal layer to the lithium layer. These two facts most

likely facilitate the formation of a spinel-like phase with an extremely low energy compared to that in the layered only composition (x = 1 sample). As Xu et al. proposed,[134] the structural transformation occurs from the surface to the bulk during the charging process, so the transformation of the layered phase to the spinel phase occurs gradually in our composite samples (x = 0.5 and 0.75) during extended electrochemical cycling. In essence, the higher lithium ion occupancy in the transition metal layer in the composite cathodes compared to that in the layered oxide only phase appears to be the reason for the facile transformation to the 3 V spinel-like phase during extended electrochemical cycling of the composite cathodes.

5.4 CONCLUSIONS

The layered-spinel composite system $x\text{Li}[\text{Li}_{0.2}\text{Mn}_{0.6}\text{Ni}_{0.17}\text{Co}_{0.03}]\text{O}_2 - (1-x)\text{Li}[\text{Mn}_{1.5}\text{Ni}_{0.425}\text{Co}_{0.075}]\text{O}_4$ with $0 \leq x \leq 1$ has been investigated systematically with XRD, ND, and electrochemical measurements. *Ex-situ* XRD data analyses indicate that the entire layered phase (*C2/m*) transforms irreversibly into a spinel phase (*Fd*-3*m*) in the composite cathodes during extended electrochemical cycling. Higher lithium occupancy in the transition metal layer of the layered phase appears to be the driving force for this facile structural transformation. As suggested by first principles calculations in the literature,[134] the migration of lithium ions from the transition metal layer into the tetrahedral sites and the consequent formation of Li-Li dumbbells during the charging process facilitate the formation of a spinel-like phase with an extremely low energy. Electrochemical data analysis suggests that the transformed cubic spinel phase (*Fd*-3*m*) consists of Mn and Ni in the 4+ state with part of the *16d* octahedral sites occupied by lithium ions as, for example, in $\text{Li}[\text{Li}_{1/3}\text{Ni}_{1/2}\text{Mn}_{7/6}]\text{O}_4$; such a spinel phase can only insert lithium into the empty 16c octahedral sites in the 3 V region without any plateau in the 4

or 4.7 V region as Mn and Ni are present in the 4+ state. In addition, $Li[Li_{1/3}Ni_{1/2}Mn_{7/6}]O_4$ does not suffer from Jahn-Teller distortion or Mn dissolution as Mn remains in the 4+ state during the charge-discharge. Additionally, the parent 5 V cubic spinel phase $Li[Mn_{1.5}Ni_{0.425}Co_{0.075}]O_4$ undergoes a cubic (*Fd*-3*m*) to tetragonal ($I4_1/amd$) transition during discharge down to 2 V, but the degree of phase transition is relatively small for the $x = 0.5$ and 0.75 compositions. Both the small capacity at ~ 2.7 and ~ 2.1 V plateaus, associated with the cubic to tetragonal transition of the parent 5 V spinel phase and the excellent stability of the newly evolved 3 V spinel-like phase from the lithium-rich layered phase lead to superior cyclability in a wide voltage range (2 – 5 V) for the composite cathodes with $x = 0.5$ and 0.75. The study suggests that carefully engineered layered-spinel composite cathodes could offer a combination of high energy and power with long cycle life.

Chapter 6: Understanding the effect of synthesis temperature on the structural and electrochemical characteristics of layered-spinel composite cathodes

6.1 INTRODUCTION

In Chapter 5, we investigated the variations in composition and wt. % from the nominal values of the layered and spinel phases for the system $x\text{Li}[\text{Li}_{0.2}\text{Mn}_{0.6}\text{Ni}_{0.17}\text{Co}_{0.03}]\text{O}_2 - (1\text{-}x)\text{Li}[\text{Mn}_{1.5}\text{Ni}_{0.425}\text{Co}_{0.075}]\text{O}_4$ ($0 \leq x \leq 1$) by employing a joint XRD and neutron diffraction (ND) Rietveld refinement method. The investigation provided useful information for explaining the unique structural and electrochemical characteristics of the layered-spinel composite materials during extended cycling.

However, the previous study in Chapter 5 was on samples synthesized at a specific temperature (800 ^{o}C). Considering the cubic close-packed array in both the layered and spinel phases, the synthesis temperatures could have a significant influence on the composition and amount of the layered and spinel phases in the composite. Accordingly, we present here an investigation of the effect of synthesis temperature on the structural and electrochemical characteristics of the layered-spinel composite system $x\text{Li}[\text{Li}_{0.2}\text{Mn}_{0.6}\text{Ni}_{0.2}]\text{O}_2 - (1\text{-}x)\text{Li}[\text{Mn}_{1.5}\text{Ni}_{0.5}]\text{O}_4$ ($0 \leq x \leq 1$), employing XRD, ND, and electrochemical analysis. In this system, the nominal oxidation states of manganese and nickel are, respectively, 4+ and 2+ and the Mn:Ni ratios are 3:1 in both the layered and spinel phases.

6.2 EXPERIMENTAL

6.2.1 Synthesis

The $x\text{Li}[\text{Li}_{0.2}\text{Mn}_{0.6}\text{Ni}_{0.2}]\text{O}_2 - (1\text{-}x)\text{Li}[\text{Mn}_{1.5}\text{Ni}_{0.5}]\text{O}_4$ samples with x = 0, 0.25, 0.5, 0.75, and 1.0 compositions as indicated in Figure 6.1 were prepared by mechanically

mixing the required amount of mixed metal hydroxides (Mn : Ni = 3 : 1) with lithium hydroxide, followed by firing at 700, 800, and 900 ^{o}C for 6 h in air. The mixed metal hydroxides were synthesized by a co-precipitation method, as described in Chapter 2, involving a drop-wise addition of a required amount of the aqueous metal acetate (Mn : Ni = 3 : 1) solution into a 2 M KOH solution under continuous stirring. The Li : Mn+Ni metal molar ratio in the mixtures were 0.5, 0.62, 0.79, 1.05, and 1.5, respectively, to obtain the x = 0, 0.25, 0.5, 0.75, and 1 samples in the xLi[$Li_{0.2}Mn_{0.6}Ni_{0.2}$]O_2 – (1-x)Li[$Mn_{1.5}Ni_{0.5}$]O_4 system.

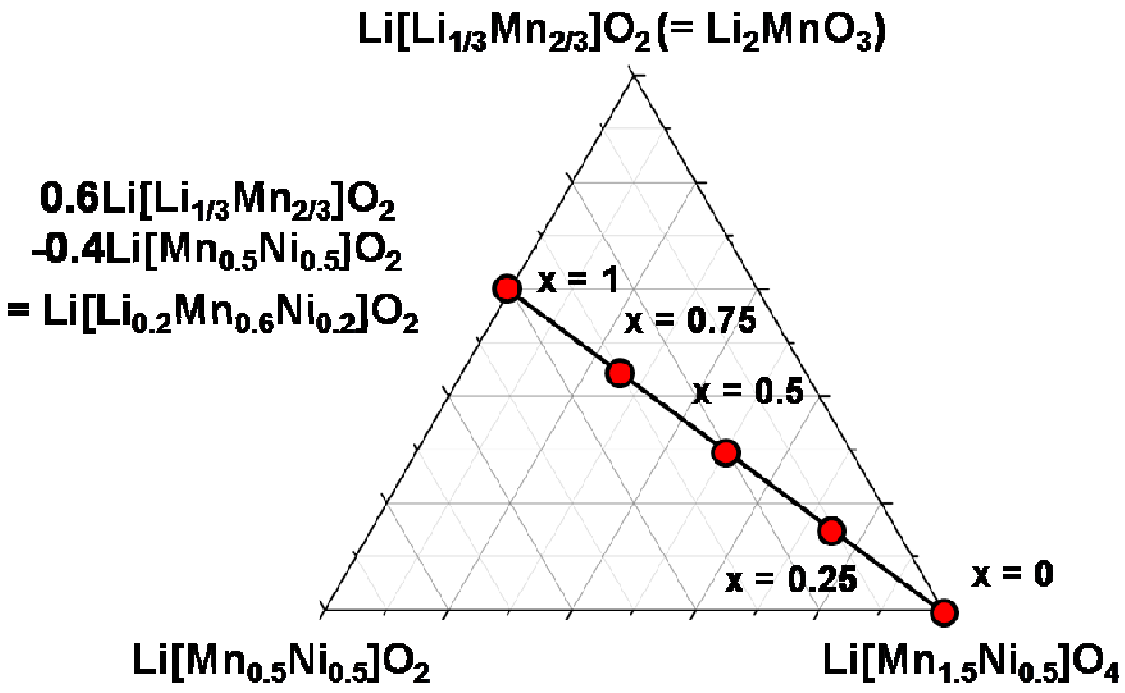

Figure 6.1. Compositional phase diagram of the xLi[$Li_{0.2}Mn_{0.6}Ni_{0.2}$]O_2 – (1-x) Li[$Mn_{1.5}Ni_{0.5}$]O_4 system.

6.2.2 Characterization

Characterization procedures for the ICP, ND, XRD, and electrochemical performance analyses are described in the experimental section in Chapter 5. Fourier transform infrared (FTIR) spectroscopy data were obtained with KBr pellets with a PerkinElmer IR spectrometer. Multi-point Brunauer−Emmett−Teller (BET) surface area data were collected with an automatic nitrogen gas sorption analyzer (NOVA 2000, Quantachrome) using physical adsorption at 77 K.

6.3 RESULT AND DISCUSSION

6.3.1 Chemical and structural analysis

ICP-AES analysis data of the metal ion contents in the $x\text{Li}[\text{Li}_{0.2}\text{Mn}_{0.6}\text{Ni}_{0.2}]\text{O}_2 - (1\text{-}x)\text{Li}[\text{Mn}_{1.5}\text{Ni}_{0.5}]\text{O}_4$ composite materials synthesized with different temperatures are given in Table 6.1. The experimental Mn/Ni and Li/[Mn + Ni] molar ratios are in good agreement with the designed nominal values, considering the experimental errors with ICP.

Table 6.1 ICP-AES compositional analysis data of the xLi[$Li_{0.2}Mn_{0.6}Ni_{0.2}$]O_2 – (1-x)Li[$Mn_{1.5}Ni_{0.5}$]O_4 composite materials cathodes.

x	Synthesis Temperature	Mn/Ni ratio	Li/[Mn+Ni] ratio	
			Nominal	Experimental
0	700°C	3.0	0.50	0.52
	800°C	3.1		0.53
	900°C	3.1		0.51
0.25	700°C	3.1	0.62	0.65
	800°C	3.1		0.60
	900°C	3.1		0.62
0.5	700°C	3.1	0.79	0.79
	800°C	3.1		0.79
	900°C	3.1		0.78
0.75	700°C	3.1	1.05	1.07
	800°C	3.1		1.07
	900°C	3.1		1.05
1	700°C	3.1	1.50	1.55
	800°C	3.1		1.53
	900°C	3.1		1.49

Figure 6.2 shows the XRD and ND patterns of the pristine xLi[$Li_{0.2}Mn_{0.6}Ni_{0.2}$]O_2 – (1-x)Li[$Mn_{1.5}Ni_{0.5}$]O_4 (x = 0, 0.25, 0.5, 0.75, and 1) composite materials prepared at 800 ^oC. The x = 0.25, 0.5, and 0.75 samples show reflections from both the layered (*C*2/*m*) and spinel (*F*d-3*m*) phases in the XRD and ND patterns. The relative intensities of the reflections from the layered phase increase with increasing x, as expected. As seen in Chapter 5, the composite materials show much clearer and stronger superstructure reflections in the 2θ range of 20.5 – 22.5° due to the higher occupancy of the lithium ions in the transition metal layer than that based on nominal composition.[129, 130] Notably, the intensities of the reflections and hence the phase fraction of the cubic impurity phase are much higher than that observed with the cobalt-doped composite materials in Chapter 5, indicating that the presence of Co restricts the formation of this impurity phase. Similar X-ray scattering factors of Mn, Ni and the low X-ray scattering factor of Li make it hard to refine the occupancy of the atoms in each phase with XRD data alone. However, the occupancy of each atom could be refined in each phase by combining the XRD and ND data as Li, Mn, and Ni have significantly different ND scattering factors.

In order to compare the structural and compositional changes of the pristine xLi[$Li_{0.2}Mn_{0.6}Ni_{0.2}$]O_2 – (1-x)Li[$Mn_{1.5}Ni_{0.5}$]O_4 (x = 0, 0.25, 0.5, 0.75, and 1) composite materials, chemical compositions and weight percentages of each phase were refined for the five pristine samples synthesized at 800 °C and the results are summarized in Table 6.2. During the refinement process, the site occupancy of lithium and oxygen in the spinel phase and oxygen in the layered phase were fixed to 1.

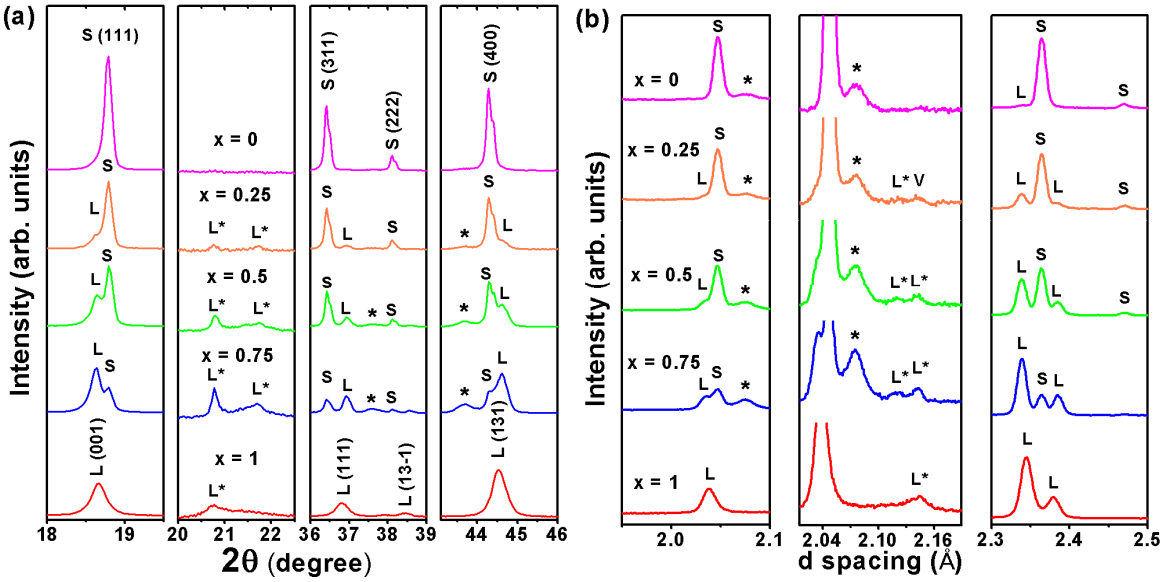

Figure 6.2. Selected portions of the (a) XRD and (b) ND patterns of the xLi[$Li_{0.2}Mn_{0.6}Ni_{0.2}$]O_2 – (1-x)Li[$Mn_{1.5}Ni_{0.5}$]O_4 (x = 0, 0.25, 0.5, 0.75, and 1) samples synthesized at 800 ^oC to show the various phases present. S and L refer, respectively, to the cubic spinel and layered phases. L* refers to the superstructure reflections arising from an ordering among the Li^+, Mn^{4+}, and Ni^{2+} ions in the layered phase. The asterisk refers to the $NiMn_6O_8$ cubic impurity phase. V refers to the reflection arising from the vanadium can used for the ND experiments.

The nominal compositions were applied for the layered phase in the x = 0 sample and spinel phase in the x = 1 sample as little or a small fraction of them is expected to be present in those samples. In the x = 0 sample, small fractions of layered (~ 4.5 wt. %) and cubic impurity phases (~ 3.9 wt. %) are detected. As explained in Chapter 5, we indexed this cubic impurity phase as the Ni_6MnO_8 phase,[107] which has a lattice parameter of ~ 8.3 Å. Due to the presence of the Ni_6MnO_8 impurity phase, the Ni content in the spinel phase appears to be lower than the nominal composition. In the x =1 sample, a small fraction (~

8.5 wt. %) of the spinel phase is observed, which leads to an increase in the lithium content in the layered phase compared to the nominal value. For the composite samples (x = 0.25, 0.5, and 0.75), a relatively large wt. % (7.0 - 11.4 %) of Ni_6MnO_8 cubic impurity phases are observed as expected in the XRD and ND data in Figure 6.2. The presence of the Ni_6MnO_8 cubic impurity phase in the composite samples reduces the nickel content in both the spinel and layered phases. Notably, the Ni content in the layered phase is affected more than that in the spinel phase since the difference between the actual and nominal wt. % of the layered phase is larger than that of the spinel phase. So it increases the lithium and manganese contents above the expected nominal values in the layered phase.

Table 6.2 Refined chemical compositions and weight percentages of the layered, spinel, and cubic impurity phases in the xLi[$Li_{0.2}Mn_{0.6}Ni_{0.2}$]O_2 – (1-x)Li[$Mn_{1.5}Ni_{0.5}$]O_4 composite materials synthesized at 800 ^oC

x	Chemical composition			Weight %			Li/[Mn+Ni] ratio
	Atom	Spinel (*Fd*-3*m*)	Layered (*C*2/*m*)	Spinel (*Fd*-3*m*)	Layered (*C*2/*m*)	Cubic impurity	
0	Li	1	1.20	91.5	4.5	3.9	0.52
	Mn	1.566(1)	0.60				
	Ni	0.434(1)	0.20				
0.25	Li	1	1.36(4)	74.7	13.9	11.4	0.65
	Mn	1.557(1)	0.62(3)				
	Ni	0.443(1)	0.02(1)				
0.50	Li	1	1.31(2)	59.8	33.2	7.0	0.85
	Mn	1.549(1)	0.65(1)				
	Ni	0.452(1)	0.04(1)				
0.75	Li	1	1.29(1)	29.4	60.6	10.0	1.16
	Mn	1.540(2)	0.65(1)				
	Ni	0.460(1)	0.06(1)				
1.00	Li	1	1.27(1)	8.5	91.5		1.62
	Mn	1.5	0.59(1)				
	Ni	0.5	0.14(1)				

In order to investigate the structural changes of the composite materials with varying synthesis temperatures, XRD patterns of the pristine xLi[$Li_{0.2}Mn_{0.6}Ni_{0.2}$]O_2 – (1-x)Li[$Mn_{1.5}Ni_{0.5}$]O_4 (x = 0, 0.25, 0.5, 0.75, and 1) composite materials synthesized at different temperatures are compared in Figure 6.3. The obtained lattice parameter values for each phase are summarized in Table 6.3. Lattice parameters were obtained with the XRD and ND joint refinement for the x = 0 and 0.5 samples synthesized at 700, 800, and 900 ^{o}C and for the x = 0.25, 0.75, and 1.0 samples synthesized at 800 °C. Lattice parameters of all other samples were obtained with the XRD data due to the limitation in the availability of ND beamtime. As explained Chapter 3, the samples of the spinel only composition Li[$Mn_{1.5}Ni_{0.5}$]O_4 (x = 0) can have two different crystallographic structures depending on the synthesis temperature: samples synthesized at high temperatures (> 700 °C) have the disordered phase with the space group *Fd-3m*, while synthesis or post annealing at 700 °C stabilizes the ordered phase with a 3:1 ordering of Mn^{4+} and Ni^{2+} ions in the 12d and 4b octahedral sites, respectively, decreasing the symmetry to the space group $P4_332$.[64, 67, 102, 104] The superstructure reflections, which originate from the transition metal ordering in the 16d octahedral sites, are not observed in the XRD patterns irrespective of thermal history. The lattice parameter of the cubic spinel phase gradually increases with increasing synthesis temperature possibly due to the (i) decreased solubility of Ni in the spinel lattice and the increased amount of Mn^{3+} in the spinel phase at high temperature[72] and (ii) decreased degree of transition metal ordering in 16d octahedral sites.[32, 63, 66, 103] In the ordered spinel phase ($P4_332$), space optimization is possible because the larger Ni^{2+} ions and the smaller Mn^{4+} ions occupy, respectively, the larger 4b sites and smaller 12d sites.[66] Therefore, the lattice parameter of the spinel phase increases with decreasing degree of ordering in the 16d sites as we saw in Chapter 3.

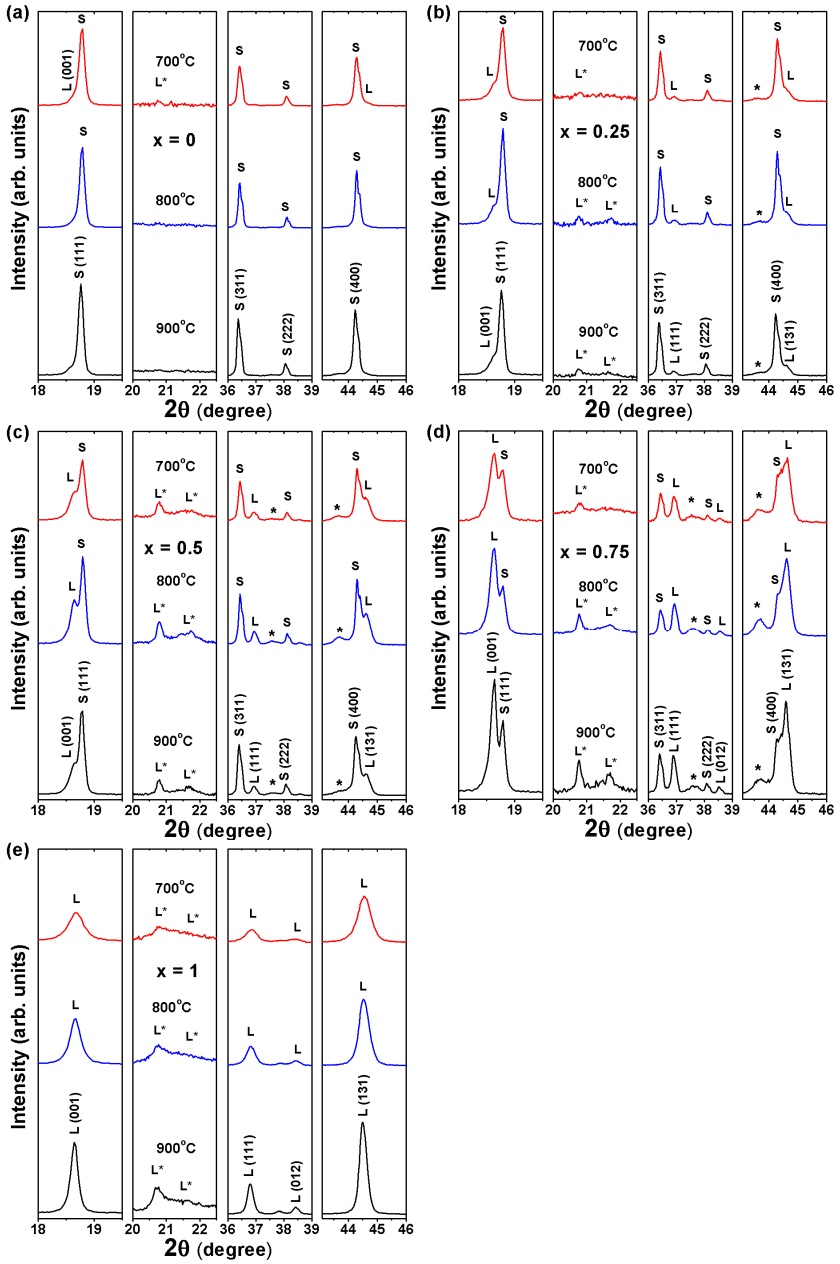

Figure 6.3. XRD patterns of the xLi[$Li_{0.2}Mn_{0.6}Ni_{0.2}$]O_2 – (1-x)Li[$Mn_{1.5}Ni_{0.5}$]O_4 samples synthesized at various temperatures: (a) x = 0, (b) x = 0.25, (c) x = 0.5, (d) x = 0.75, and (e) x = 1. S and L refer, respectively, to the cubic spinel and layered phases. L* refers to the superstructure reflections arising from an ordering among the Li^+, Mn^{4+}, and Ni^{2+} ions in the layered phase. The asterisk refers to the $NiMn_6O_8$ cubic impurity phase.

Table 6.3 Lattice parameters of the layered and spinel phases in xLi[$Li_{0.2}Mn_{0.6}Ni_{0.2}$]O_2 − (1-x)Li[$Mn_{1.5}Ni_{0.5}$]O_4 composite materials synthesized at different temperatures.

x	Synthesis Temp.	Spinel (*Fd*-3*m*)		Layered (*C*2/*m*)				
		a (Å)	V (Å^3)	a (Å)	b (Å)	c (Å)	β	V (Å^3)
0	700°C	8.1731(1)	545.9					
	800°C	8.1763(1)	546.6					
	900°C	8.1801(1)	547.4					
0.25	700°C	8.1718(4)	545.7	4.9322(3)	8.5318(10)	5.0329(3)	109.32(1)	199.9
	800°C	8.1754(1)	546.4	4.9414(2)	8.5529(3)	5.0447(1)	109.29(1)	201.2
	900°C	8.1810(3)	547.5	4.9374(2)	8.5448(6)	5.0377(1)	109.32(1)	200.6
0.5	700°C	8.1724(1)	545.8	4.9372(2)	8.5450(3)	5.0409(1)	109.15(1)	200.8
	800°C	8.1746(1)	546.3	4.9412(1)	8.5530(1)	5.0441(1)	109.28(1)	201.2
	900°C	8.1839(1)	548.1	4.9404(1)	8.5496(2)	5.0452(1)	109.30(1)	201.1
0.75	700°C	8.1706(6)	545.5	4.9419(6)	8.5255(11)	5.0370(5)	109.26(1)	200.3
	800°C	8.1752(1)	546.4	4.9418(1)	8.5539(1)	5.0443(1)	109.29(1)	201.3
	900°C	8.1773(2)	546.8	4.9406(6)	8.5522(11)	5.0508(6)	109.26(1)	201.5
1	700°C			4.9719(9)	8.5540(2)	5.0301(12)	109.23(1)	202.0
	800°C			4.9591(2)	8.5779(2)	5.0299(1)	109.19(1)	202.1
	900°C			4.9599(5)	8.5782(9)	5.0359(5)	109.25(1)	202.3

Due to the similar X-ray scattering factor of Mn and Ni, XRD is not a powerful method for identification of the transition-metal ordering in the spinel phase. In contrast, the infrared spectra and ND data can be used for identifying transition metal ordering in the spinel phase.[66, 100, 104, 142] In the ordered spinel phase, the infrared spectra has well-distinguished peaks due to the existence of long-range order and the ND pattern has the superstructure reflections from the transition metal ordering in the 16d octahedral sites. The infrared spectra of the $x = 0$ composition synthesized at different temperatures are compared in Figure 6.4(a) The number of distinctive peaks increases with decreasing synthesis temperature, supporting the idea of increased transition metal ordering in the spinel phase. The sample synthesized at 700 ^{o}C has seven distinctive bands and the observed wavenumbers match with the values in the literature.[67, 104] In addition, we can see in Figure 6.4(b) that the ND data of the sample synthesized at 700 ^{o}C show superstructure reflections, which originate from the transition metal ordering in the 16d octahedral sites. From the decrease in the refined lattice parameters, existence of superstructure reflections in the ND data, and infrared spectroscopy data, we can conclude that the degree of transition metal ordering in the spinel phase increases with decreasing synthesis temperature. Furthermore, very weak reflections corresponding to the layered phase are detected both in the XRD and ND patterns of the sample synthesized at 700 ^{o}C.

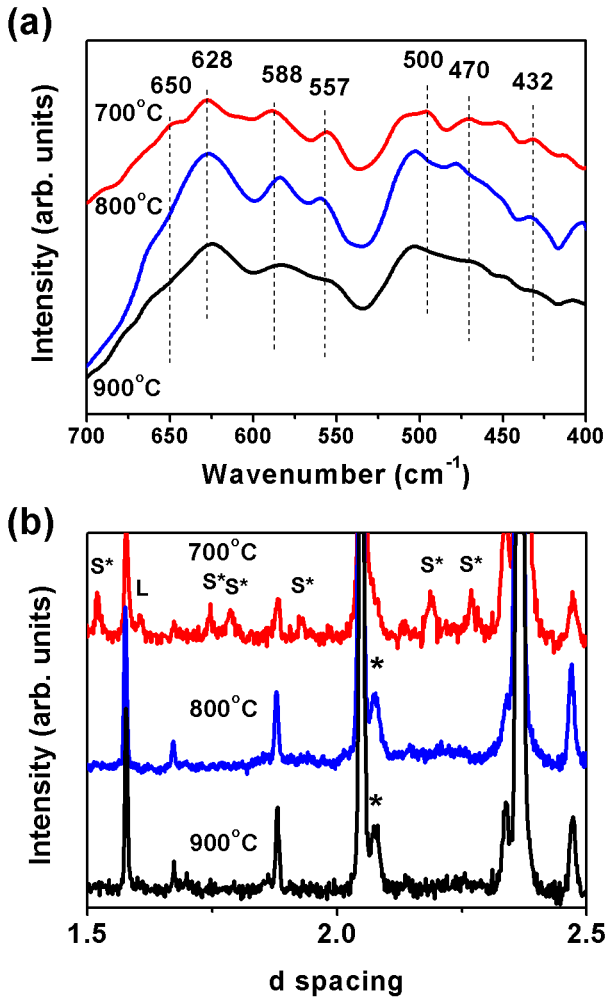

Figure 6.4. (a) Infrared spectra and (b) ND patterns of the xLi[$Li_{0.2}Mn_{0.6}Ni_{0.2}$]O_2 – (1-x)Li[$Mn_{1.5}Ni_{0.5}$]O_4 (x = 0) samples synthesized at various temperatures. S* refers to the superstructure reflections arising from an ordering of the Mn^{4+} and Ni^{2+} ions in the 16d octahedral sites of the spinel phase. The asterisk refers to the $NiMn_6O_8$ cubic impurity phase.

The samples of the layered only composition (x = 1) have the layered structure with the space group $C2/m$.[128] The peak shape in the XRD patterns gradually becomes broad and asymmetric with decreasing synthesis temperature possibly due to the decreased particle size and increased amount of secondary spinel phase in the sample. The layered phase differs from the pure spinel composition in that the synthesis temperature does not have a noticeable effect on the lattice parameter. For the composite samples (x = 0.25, 0.5, and 0.75), similar trends of lattice parameter changes are observed for the spinel and layered phase. The lattice parameter of the spinel phase in the composite samples gradually increases with increasing synthesis temperature as seen in the x = 0 composition due to both the (i) decreased solubility of Ni and the increased amount of Mn^{3+} in the spinel phase[72] and (ii) decreased degree of transition metal ordering in the spinel phase. Similar to that found with the x = 1 composition, the synthesis temperature does not clearly affect the lattice parameter of the layered phase in the composite samples.

For the x = 0.5 composite samples synthesized at 700 and 900 ^{o}C, XRD and ND joint Rietveld refinement were performed to investigate the effect of the synthesis temperature on the composition and weight percentage changes of the layered and spinel phases. BET data were also measured with all the x = 0.5 composite samples to investigate the surface area change with the synthesis temperature. The obtained variations of the composition, weight percent, and surface area are given in Table 6.4. As seen in Table 6.4, a decrease in synthesis temperature leads to a slight (~ 6 wt. %) increase in the amount of the layered phase at the expense of the spinel phase. The weight percent of the cubic impurity phase is ~ 7 wt% regardless of the synthesis temperature. The refined compositions of the x = 0.5 composite samples do not show abrupt compositional variations with the synthesis temperature. From this analysis, it is

confirmed that synthesis temperatures between 700 – 900 ^{o}C do not severely affect the phase composition of the composite cathode with x = 0.5. In contrast, the synthesis temperature clearly does affect the surface area of the composite cathode material. As we can see in Table 6.4, the surface area of the composite cathode material decreases significantly from 2.77 to 0.03 m^2/g as the synthesis temperature increases from 700 to 900 ^{o}C.

Table 6.4 Refined chemical compositions, weight percentages, and surface areas of the $0.5Li[Li_{0.2}Mn_{0.6}Ni_{0.2}]O_2 - 0.5Li[Mn_{1.5}Ni_{0.5}]O_4$ composite materials synthesized at different temperatures.

Synthesis Temperature	Chemical composition			Weight %			Surface area (m^2/g)
	Atom	Spinel (*Fd*-3*m*)	Layered (*C*2/*m*)	Spinel (*Fd*-3*m*)	Layered (*C*2/*m*)	Cubic impurity	
700^{o}C	Li	1	1.29(2)	55.6	37.2	7.2	2.77
	Mn	1.524(1)	0.66(2)				
	Ni	0.476(1)	0.07(1)				
800^{o}C	Li	1	1.31(2)	59.8	33.2	7.0	1.21
	Mn	1.549(1)	0.65(1)				
	Ni	0.452(1)	0.04(1)				
900^{o}C	Li	1	1.26(1)	61.5	31.3	7.0	0.03
	Mn	1.566(1)	0.69(1)				
	Ni	0.434(1)	0.04(1)				

6.3.2 First cycle charge-discharge profiles

Figure 6.5 shows the first cycle charge-discharge profiles of the $x\text{Li}[\text{Li}_{0.2}\text{Mn}_{0.6}\text{Ni}_{0.2}]\text{O}_2 - (1\text{-}x)\text{Li}[\text{Mn}_{1.5}\text{Ni}_{0.5}]\text{O}_4$ (x = 0, 0.25, 0.5, 0.75, and 1) composite materials synthesized at different temperature. As mentioned in Chapter 3, five distinctive plateaus are apparent during the discharge of the spinel $\text{Li}[\text{Mn}_{1.5}\text{Ni}_{0.5}]\text{O}_4$ (x = 0) phase. The three plateaus above 3 V (two at ~ 4.7 V and one at ~ 4.0 V) are attributed to lithium ion insertion into the 8a tetrahedral sites of the cubic spinel structure. The two plateaus at ~ 4.7 V are associated with the reduction of Ni^{4+} to Ni^{2+} through Ni^{3+},[103, 109] while the ~ 4.0 V plateau originates from the reduction of Mn^{4+} due to the existence of small amount of Mn^{3+} ions in the pristine state.[32, 104] The plateau length at ~ 4.0 V decreases with decreasing synthesis temperature due to the decrease in Mn^{3+} content in the spinel phase. The two plateaus below 3 V, at ~ 2.7 and ~ 2.1 V, originate from lithium-ion insertion into the empty 16c octahedral sites of the cubic spinel structure through the reduction of Mn^{4+} to Mn^{3+}, which is associated with a cubic to tetragonal phase transition.[67-69, 110] As we can see in Figure 6.5(a), the synthesis temperature affects the discharge profile below 3 V more significantly than above 3 V in the spinel phase. We have identified in Chapter 3 that the ~ 2.7 and ~ 2.1 V plateaus are accompanied by the creation of two different tetragonal phases with different lattice volumes and *c/a* ratios. It appears that as the degree of transition metal ordering in the spinel phase increases, the capacity at the ~ 2.7 V plateau increases at the expense of the capacity at the ~ 2.1 V plateau. The longer length of the ~ 2.7 V plateau displayed by the ordered spinel sample is attributed to the facile lithium ion insertion into the empty octahedral sites, with little lattice distortion as the empty octahedral sites (4a sites) in the ordered spinel are larger than the size of Li^+ ions. On the other hand, the longer length of the ~

2.1 V plateau displayed by the disordered spinel sample is attributed to the sluggish lithium ion insertion into the empty octahedral sites, with a large lattice distortion as the empty octahedral sites (16c sites) in the disordered spinel are smaller than the size of Li^+ ions. In this regard, the increase in transition metal ordering in the 16d sites of the spinel phase with decreasing synthesis temperature is also confirmed by the electrochemical data, *i.e.* by the differences in the relative lengths of the plateaus at ~ 2.7 and ~ 2.1 V. In addition to the discharge capacities from the five spinel plateaus, a small capacity from the layered phase can also be observed as a sloping profile from 3.8 - 2.8 V for the sample synthesized at 700 ^oC, which is consistent with the XRD data in Figure 6.3(a).

The lithium-rich layered oxide only composition $Li[Li_{0.2}Mn_{0.6}Ni_{0.2}]O_2$ (x = 1) shows the typical first charge and discharge profiles as expected from the literature.[44, 120] The capacities of the sloping region (OCV to ~ 4.5 V) during first charge, in which lithium-ion removal is associated with the oxidation of Ni^{2+} to Ni^{4+}, are similar regardless of the synthesis temperature;[42, 43] however, the capacities of the plateau region (around 4.5 V),[44, 131, 132] which originate from the lithium-ion removal from the lattice by the oxidation of O^{2-} ions to O, decrease with decreasing synthesis temperature. This leads to a decrease in the first discharge capacity with decreasing synthesis temperature since the discharge capacity of lithium-rich layered oxides depends on the irreversible loss of oxygen from the lattice during the first charge.[44] This decrease in the plateau region with decreasing synthesis temperature could be due to the presence of more lithium ions in the transition metal layer, which originates from the increase in the secondary spinel phase in the sample as mentioned earlier. As we explained in Chapter 5, the higher lithium content in the transition metal layer markedly affects lithium ion extraction during the charge process due to the increased migration of nickel ions to the lithium layer.[120, 134] The

increased nickel ion content in the lithium layer decreases the lithium ion diffusivity by interfering with the diffusion paths of the lithium ions.

The composite materials $x\text{Li}[\text{Li}_{0.2}\text{Mn}_{0.6}\text{Ni}_{0.2}]\text{O}_2 - (1\text{-}x)\text{Li}[\text{Mn}_{1.5}\text{Ni}_{0.5}]\text{O}_4$ with x = 0.25, 0.5, and 0.75) show both the spinel and layered oxide characteristics in their charge-discharge profiles, as expected. Generally, the capacities from the spinel phase do not change much with synthesis temperature variation; however, it is noted that the capacity from the ~2.7 V plateau increases at the expense of the ~ 2.1 V plateau with decreasing synthesis temperature as was seen in the spinel only composition (x = 0). In this regard, an increase in transition metal ordering in the spinel phase in the composite material is also expected with decreasing synthesis temperature, as in the spinel only (x = 0) composition. Figure 6.5(b) - (d) illustrates that the synthesis temperature noticeably affects the discharge capacity of the layered phase. This behavior is consistent with the previous studies on Li_2MnO_3.[143] The discharge capacity from the layered phase observed in the sloping region between 3.8 and 2.8 V increases with decreasing synthesis temperature due to the increase in the surface area of the samples as shown by the BET data in Table 6.4. The layered phases in the composite materials show smaller capacities than expected from the nominal composition, while the spinel phases show slightly higher capacities than expected from the nominal composition. This is due to the higher lithium ion content in the transition metal layer as mentioned in Chapter 5. As we can see in Table 6.2, the actual lithium contents in the layered phases in the x = 0.25, 0.5, and 0.75 samples synthesized at 800 ^{o}C are much higher than the nominal values. The higher capacities of the spinel phase in the composite materials are attributed to the higher weight percentages of the spinel phase than the nominal value, as we can see in Tables 6.2 and 6.4.

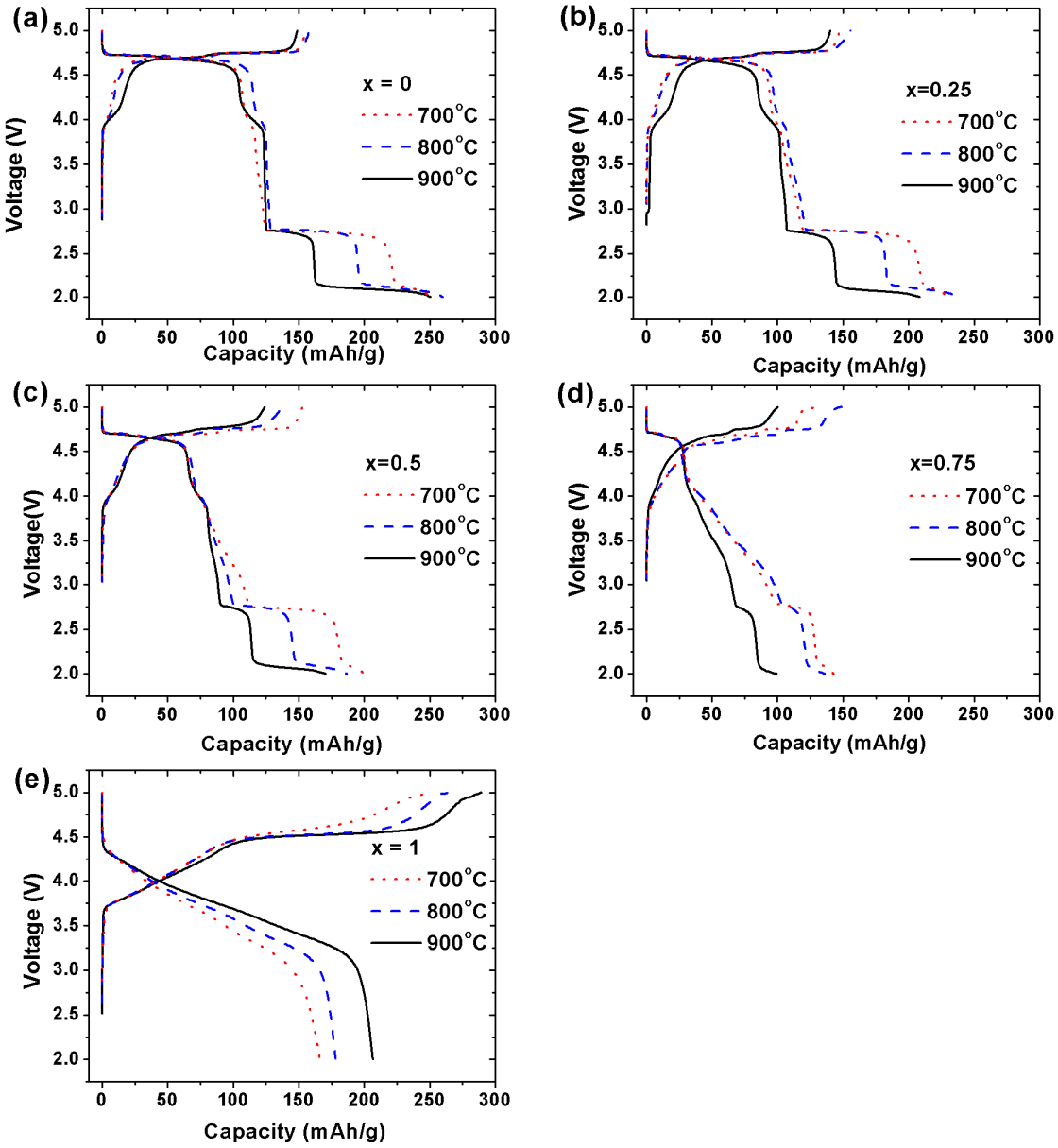

Figure 6.5. First cycle charge-discharge profiles of the xLi[$Li_{0.2}Mn_{0.6}Ni_{0.2}$]O_2 – (1-x)Li[$Mn_{1.5}Ni_{0.5}$]O_4 samples synthesized at various temperatures when cycled between 2 and 5 V at 10 mA/g: (a) x = 0, (b) x = 0.25, (c) x = 0.5, (d) x = 0.75, and (e) x = 1.

6.3.3 Cyclability

Figure 6.6 shows the cyclability of the xLi[$Li_{0.2}Mn_{0.6}Ni_{0.2}$]O_2 – (1-x)Li[$Mn_{1.5}Ni_{0.5}$]O_4 (x = 0, 0.25, 0.5, 0.75, and 1) composite materials synthesized at different temperatures. As explained in Chapter 3, the spinel Li[$Mn_{1.5}Ni_{0.5}$]O_4 (x = 0) samples show inferior cycle performance due to the large volume and *c/a* ratio changes, which are attributed to the cubic to tetragonal phase transitions during lithium ion insertion/extraction into/from the 16c octahedral sites. On the other hand, the layered Li[$Li_{0.2}Mn_{0.6}Ni_{0.2}$]O_2 (x =1) samples show good cycle performance. Interestingly, the layered samples synthesized at 700 and 800 ^oC show a gradual increase in discharge capacity over 50 cycles. After 50 cycles, all of the layered Li[$Li_{0.2}Mn_{0.6}Ni_{0.2}$]O_2 samples display a similar discharge capacity of about 200 mAh/g. The x = 0.25 samples show inferior cycle performance similar to the x = 0 sample due to the large fraction of the spinel phase in the samples. Unlike the cobalt-doped sample in Chapter 5, the x = 0.5 samples in this system also show inferior cycle performance except for the sample synthesized at 900 ^oC. The x = 0.75 samples, however, exhibit a superior cycle performance with a gradual increase in discharge capacity over 50 cycles with characteristics similar to the cobalt-doped sample in Chapter 5. After 50 cycles, the discharge capacities of the x = 0.75 samples reaches 213, 220, and 196 mAh/g for the 700, 800, and 900 ^oC samples. The reason for the varying cycle performance will be discussed in the following section with the charge-discharge profile analysis.

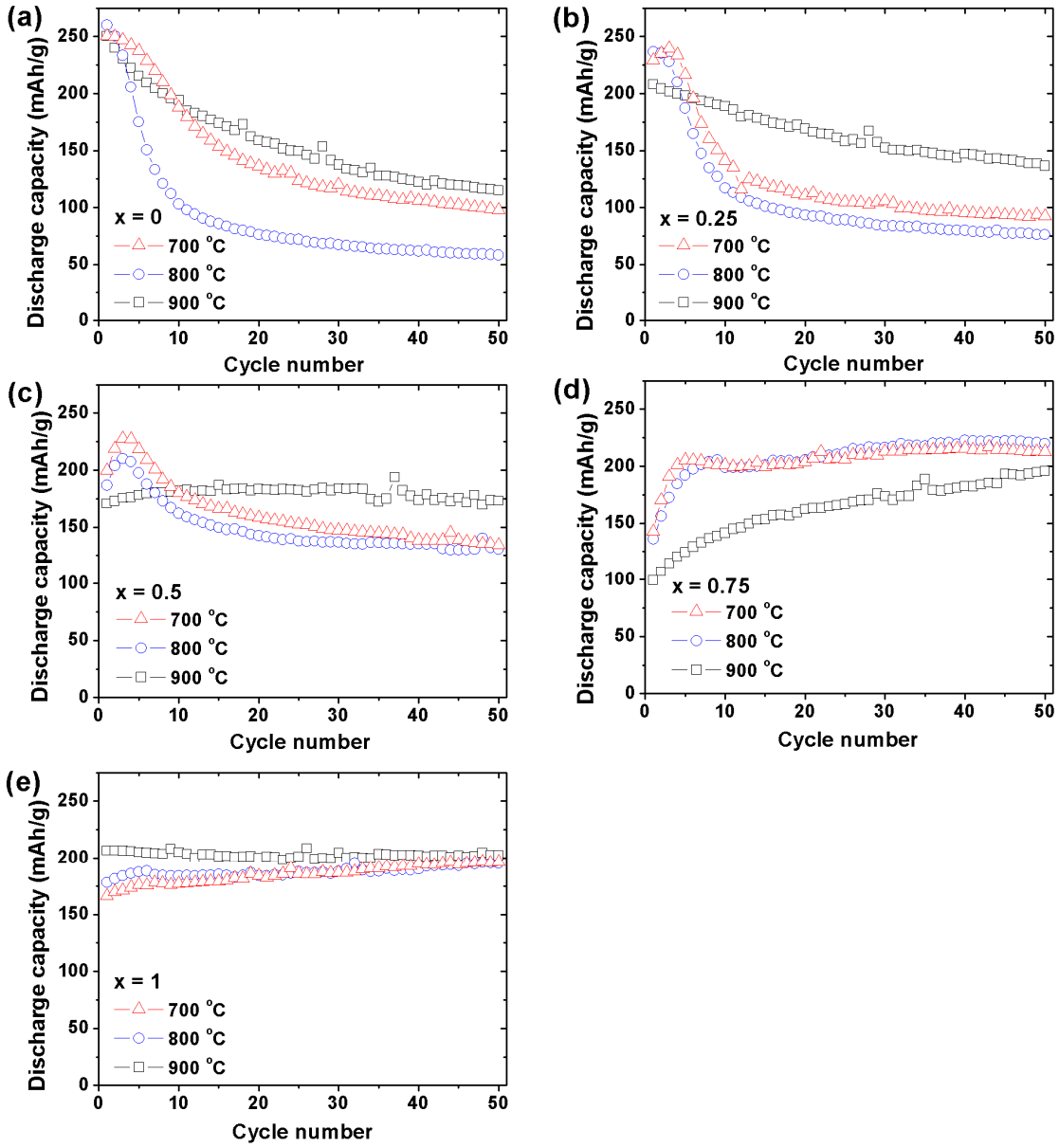

Figure 6.6. Cyclability data of the xLi[$Li_{0.2}Mn_{0.6}Ni_{0.2}$]O_2 – (1-x)Li[$Mn_{1.5}Ni_{0.5}$]O_4 samples synthesized at various temperatures when cycled between 2 and 5 V at 10 mA/g: (a) x = 0, (b) x = 0.25, (c) x = 0.5, (d) x = 0.75, and (e) x = 1.

6.3.4 Charge-discharge profile analyses during cycling

Figure 6.7 compares the charge-discharge profiles at the 25th and 50th cycles of the xLi[$Li_{0.2}Mn_{0.6}Ni_{0.2}$]O_2 – (1-x)Li[$Mn_{1.5}Ni_{0.5}$]O_4 (x = 0, 0.25, 0.5, 0.75, and 1) composite materials synthesized at different temperatures. The spinel Li[$Mn_{1.5}Ni_{0.5}$]O_4 (x = 0) samples steadily lose their capacities as shown by the decreased length of the five distinctive plateaus during cycling. The sample synthesized at 900 ^{o}C shows the lowest capacity reduction due to the decrease in the reaction of the cathode surface with the electrolyte caused by the smaller surface area. The layered Li[$Li_{0.2}Mn_{0.6}Ni_{0.2}$]O_2 (x =1) samples show a gradual voltage decay even while delivering a constant discharge capacity for the 900 ^{o}C sample and a steadily increasing discharge capacity for the 800 and 700 ^{o}C samples. As revealed in the literature, this voltage decay is explained by the slow phase transformation to a spinel-like phase during cycling by the migration of manganese and nickel ions into the lithium layer.[50, 134] The x = 0.25 samples show charge-discharge profile changes during 50 cycles similar to the x = 0 sample due to the large fraction of the spinel phase in the samples. In addition to the capacity fade of the five distinctive plateaus, the capacity of the layered phase shown by the sloping region between 3.8 - 2.8 V at the first cycle in Figure 6.5(b) also disappears by the 50th cycle.

The x = 0.5 and 0.75 samples show similar charge-discharge profile changes over 50 cycles. As a representative example, several charge-discharge profiles of the x = 0.5 and 0.75 samples synthesized at 800 ^{o}C are shown in Figure 6.8 to illustrate the details of the changes. The layered phases in the x = 0.5 and 0.75 samples exhibit similar charge-discharge profile changes over 50 cycles. Initially, the discharge capacity in the sloping region (3.8 – 2.8 V) steadily increases due to the increased utilization of the layered phase, but then the gradient of the sloping region gradually decreases and finally changes

to the ~ 3 V plateau by the 50^{th} cycle. We revealed in Chapter 5 that this voltage profile change of the layered phase in the composite cathode materials originates from the gradual phase transformation of the layered phase to a 3 V spinel-like phase. It was proposed that the newly created 3 V spinel-like phase does not suffer from Jahn-Teller distortion or Mn dissolution as the Mn oxidation state remains 4+ during the charge-discharge process. On the other hand, the parent 5 V spinel phases in the $x = 0.5$ and 0.75 samples gradually lose their capacity over 50 cycles. This is a different characteristic compared to the cobalt-doped composite samples in Chapter 5. We believe that the relatively higher discharge capacity of the parent 5 V spinel phases at the ~ 2.7 and ~ 2.1 V plateaus in this system is the reason for the capacity fade of the parent 5 V spinel phase. In other words, a larger portion of the parent 5 V spinel phase undergoes Jahn-Teller distortion (cubic to tetragonal transformation) in this system compared to the system containing cobalt due to the smaller lattice distortion during lithium-ion insertion into the 16d octahedral sites. From the aforementioned charge-discharge profile analysis, we deduce that the superior cycle performance of the $x = 0.75$ samples originate from the higher wt. % of layered phase, which undergoes a continuously increasing electrochemical utilization during cycling, followed by gradual phase transformation to a stable 3 V spinel-like phase.

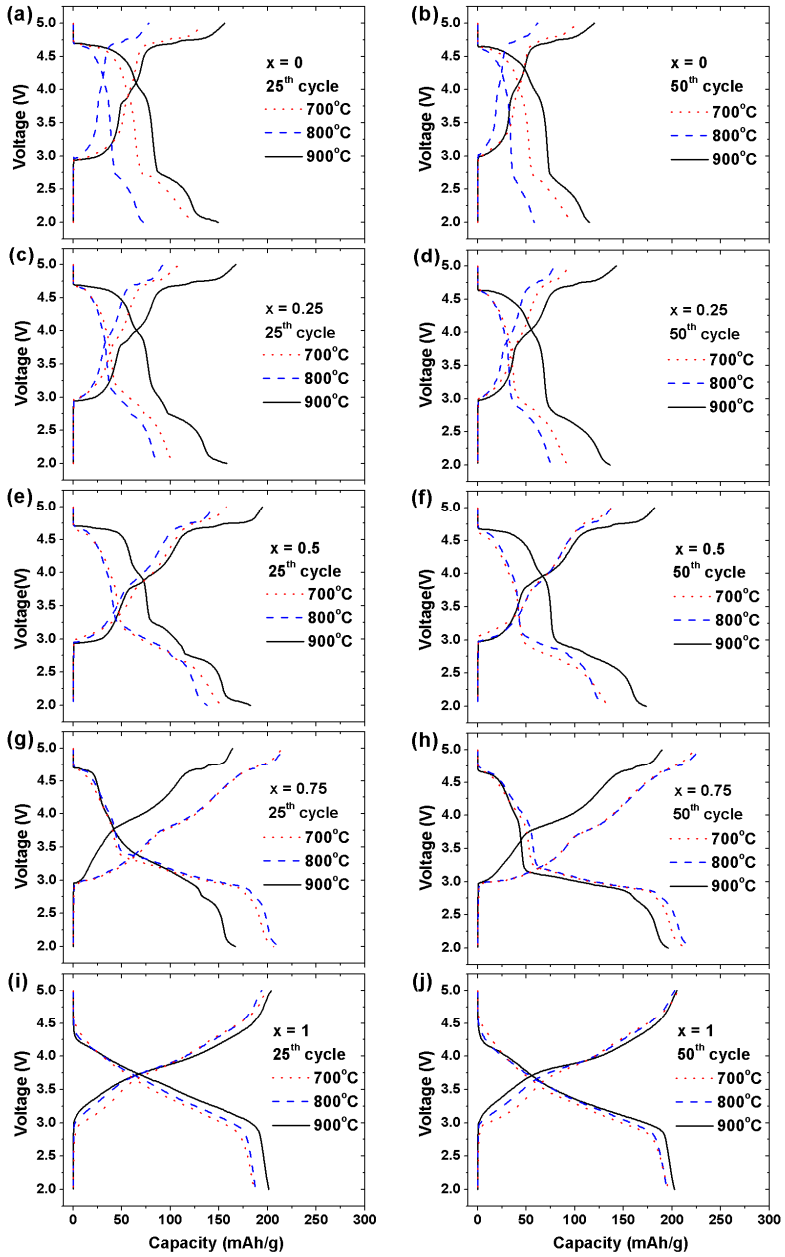

Figure 6.7. Charge-discharge profiles of the xLi[$Li_{0.2}Mn_{0.6}Ni_{0.2}$]O_2 – (1-x)Li[$Mn_{1.5}Ni_{0.5}$]O_4 samples synthesized at various temperatures when cycled between 2 and 5 V at 10 mA/g: at the 25th cycle [(a) x = 0, (c) x = 0.25, (e) x = 0.5, (g) x = 0.75, and (i) x = 1] and at the 50th cycle [(b) x = 0, (d) x = 0.25, (f) x = 0.5, (h) x = 0.75, and (j) x = 1].

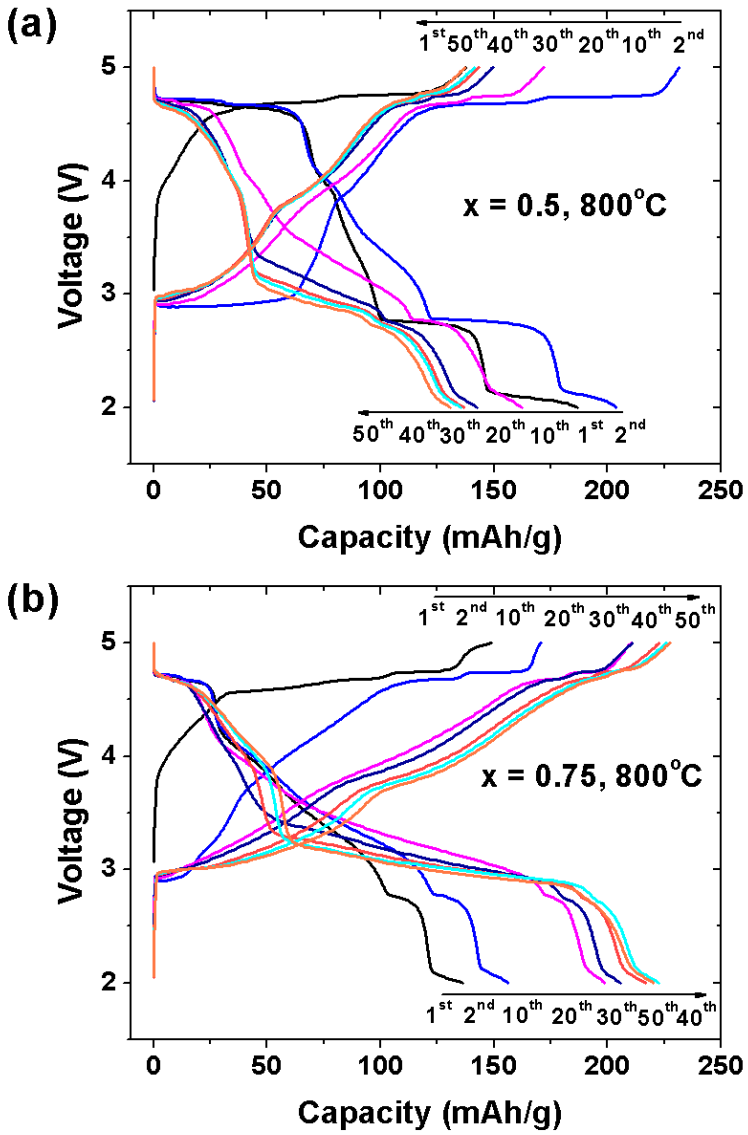

Figure 6.8. Charge-discharge profiles of the 1st, 2nd, 10th, 20th, 30th, 40th and 50th cycles of the xLi[$Li_{0.2}Mn_{0.6}Ni_{0.2}$]O_2 – (1-x)Li[$Mn_{1.5}Ni_{0.5}$]O_4 samples synthesized at 800 °C when cycled between 2 and 5 V at 10 mA/g: (a) x = 0.5 and (b) x = 0.75.

6.3.5 *Ex-situ* XRD data analysis

We discussed in Chapter 5 that the layered phase in the cobalt-doped layered-spinel composite materials (x = 0.5 and 0.75) undergoes complete phase transformation to a 3 V spinel-like phase after 50 cycles due to a higher lithium ion content in the transition metal layer compared to the nominal composition. It appears from the charge-discharge profile analyses that the phase transformation of the layered phases in the x = 0.5 and 0.75 samples also occur in this layered-spinel composite system. In order to confirm that the same phase transformation phenomena can be found in this layered-spinel composite system regardless of synthesis temperature, *ex-situ* XRD data were collected after the 50^{th} cycle for all the x = 0.5 and 0.75 composite samples in the discharged state. The *ex-situ* XRD data after 50 cycles are compared with the pristine XRD data in Figure 6.9. As we can see in Figure 6.9, after the 50^{th} cycle, the reflections corresponding to the layered phase (*C2/m*), such as the (001), (111), and (131) reflections, completely vanish in all the x = 0.5 and 0.75 samples irrespective of their synthesis temperature. Instead of the reflections corresponding to the layered phase (*C2/m*), the reflections corresponding to the tetragonal phase ($I4_1/amd$) are observed in addition to the reflections corresponding to the cubic spinel phase (*Fd*-3*m*), which is similar to the results found in Chapter 5. The tetragonal phase ($I4_1/amd$) originates from the cubic to tetragonal phase transition of the parent 5 V spinel phase during discharge down to 2 V. By combining the *ex-situ* XRD data after the 50^{th} cycle and the formation of a 3 V plateau at the 50^{th} cycle in the charge-discharge profile analysis data in Figure 6.7(f) and 6.7(h), we can also confirm the complete transformation of the layered phase (*C2/m*) in the x = 0.5 and 0.75 samples to a 3 V spinel-like phase (*Fd*-3*m*) after 50 cycles similar to that in Chapter 5.

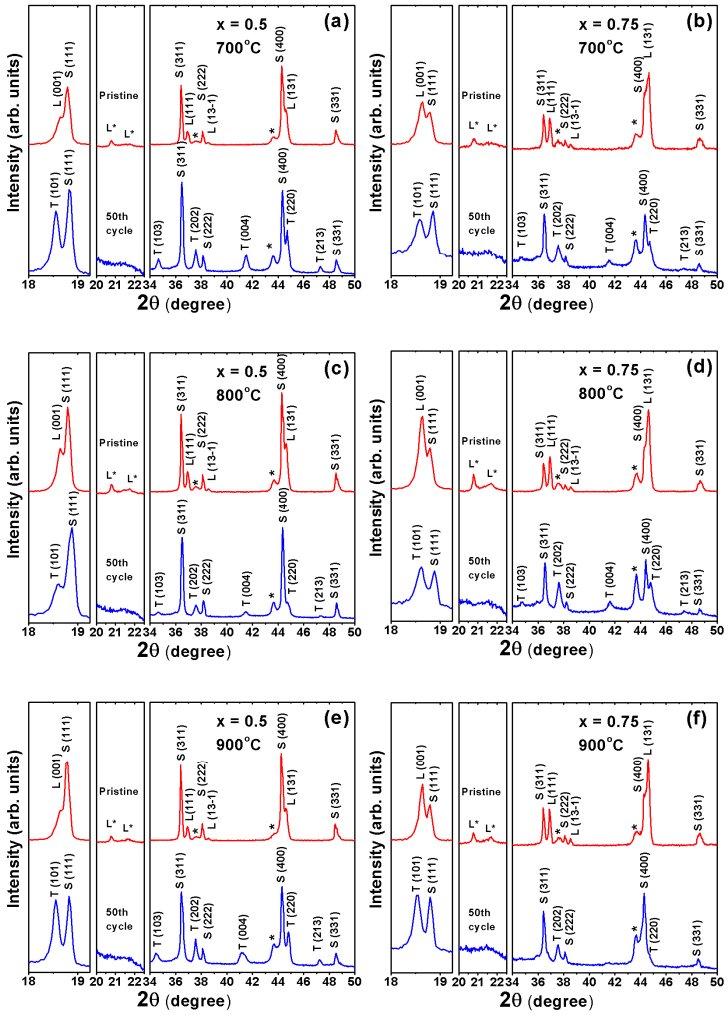

Figure 6.9. Comparison of XRD patterns of the xLi[$Li_{0.2}Mn_{0.6}Ni_{0.2}$]O_2 – (1-x)Li[$Mn_{1.5}Ni_{0.5}$]O_4 (x = 0.5 and 0.75) samples synthesized at various temperatures before cycling and after the 50th cycle: (a) x = 0.5 sample synthesized at 700 ^{o}C, (b) x = 0.75 sample synthesized at 700 ^{o}C, (c) x = 0.5 sample synthesized at 800 ^{o}C, (d) x = 0.75 sample synthesized at 800 ^{o}C, (e) x = 0.5 sample synthesized at 900 ^{o}C, and (f) x = 0.75 sample synthesized at 900 ^{o}C. L, S, and T refer, respectively, to the layered, cubic spinel, and tetragonal spinel phases. L* refers to the superstructure reflections arising from an ordering among the Li^{+}, Mn^{4+}, and Ni^{2+} ions in the layered phase. The asterisk refers to the $NiMn_6O_8$ cubic impurity phase.

6.4 CONCLUSIONS

The effect of synthesis temperature on the structural and electrochemical characteristics of the layered-spinel composite system $x\text{Li}[\text{Li}_{0.2}\text{Mn}_{0.6}\text{Ni}_{0.2}]\text{O}_2 - (1-x)\text{Li}[\text{Mn}_{1.5}\text{Ni}_{0.5}]\text{O}_4$ ($0 \leq x \leq 1$) has been investigated systematically with XRD, ND, and electrochemical measurements. By joint ND and XRD Rietveld refinement method, the composition and weight percentage variations of the layered and spinel phases in the composite samples with different synthesis temperatures have been obtained. While no pronounced composition and weight percentage variations are found with the synthesis temperature, the electrochemical characteristics of both the layered and spinel phases are highly affected by the synthesis temperature. The capacity from the layered phase increases with decreasing synthesis temperature due to the increased surface area. For the spinel phase, synthesis temperature highly affects the discharge profile below 3 V due to the decrease in lattice distortion by the increase in the transition metal ordering with decreasing synthesis temperature. The combined electrochemical and *ex-situ* XRD data reveal a complete transformation of the layered phase (*C2/m*) in the x = 0.5 and 0.75 samples to a 3 V spinel-like phase (*Fd*-3*m*) after 50 cycles due to the higher lithium-ion content in the layered phase, which is similar to that found in Chapter 5 with the cobalt-doped systems. In contrast to cobalt-doped systems, the spinel phases in the x = 0.5 and 0.75 samples gradually lose their capacity over 50 cycles due to the higher capacity of the ~ 2.7 and 2.1 V plateaus, which is associated with a cubic to tetragonal phase transition involving large volume and *c/a* ratio changes. The study suggests that tailored and optimized electrochemical characteristics of layered-spinel composite cathode materials could be possible by controlling the transition metal composition, synthesis temperature, transition metal ordering in the spinel phase, and the particle size of the samples.

Chapter 7: High-capacity $Li[Li_{0.2}Mn_{0.54}Ni_{0.13}Co_{0.13}]O_2 – VO_2(B)$ composite cathodes with controlled irreversible capacity loss for lithium-ion batteries

7.1 INTRODUCTION

As mentioned in Chapter 1, lithium-rich layered oxides $Li[Li,Mn,Ni,Co]O_2$, which are solid solutions between layered $Li[Li_{1/3}Mn_{2/3}]O_2$ and $LiMO_2$ (M = Mn, Ni, and Co), have become appealing as they offer high capacities of ~ 250 mAh/g when charged above 4.5 V.[39-41, 43, 44] However, the inferior rate capability, large irreversible capacity loss (C_{irr}) in the first cycle, and decline in cell voltage during cycling are major obstacles for the commercialization of these cathode materials.

To overcome these drawbacks and improve the electrochemical performances of the lithium-rich layered oxide cathodes, various strategies have been pursued. Surface coating with other materials such as Al_2O_3, $AlPO_4$, RuO_2, $LiNiPO_4$, C, and Al have been found to reduce the C_{irr} and increase the rate capability significantly, as the surface coating helps retain oxide-ion vacancies and lithium sites in the layered lattice after the first charge.[48, 49, 51-54] Similarly, surface treatment with mild acids has also been reported to reduce the C_{irr}.[55, 56] Aside from surface modification strategies, our group recently showed that blending the lithium-rich layered oxide $Li[Li_{0.2}Mn_{0.54}Ni_{0.13}Co_{0.13}]O_2$ with lithium-free insertion hosts such as V_2O_5, $Li_4Mn_5O_{12}$, and LiV_3O_8 is another effective way for eliminating the C_{irr}.[57, 58] The lithium-free insertion hosts provide the lithium sites for inserting the lithium ions that could not be inserted back into the layered oxide lattice. While some of these lithium-free hosts like V_2O_5 tends to exhibit capacity fade, nanocrystalline $VO_2(B)$ is known to exhibit good cyclability with high-capacity.[144] Recently, surface coating of the lithium-rich layered oxide with mixed valent VO_x, consisting of mainly V_2O_5 with a small portion of VO_2, has been reported to be effective

in protecting and stabilizing the layered oxide surface from the electrolyte.[145] However, the electrochemical performance of lithium-rich layered oxide – VO_2(B) composite has not been investigated before. Accordingly, we present here the electrochemical performances of the $Li[Li_{0.2}Mn_{0.54}Ni_{0.13}Co_{0.13}]O_2$ – VO_2(B) composite cathodes with various VO_2(B) contents. A comparison of the performances of VO_2(B) prepared by three different methods and the influence of the amount of VO_2(B) in the composite cathode on the irreversible capacity loss, cyclability, and rate capability are presented.

7.2 EXPERIMENTAL

7.2.1 Synthesis

The layered $Li[Li_{0.2}Mn_{0.54}Ni_{0.13}Co_{0.13}]O_2$ oxide was synthesized by a coprecipitation method, followed by heat treatment at 900 ^oC for 24 h in air as reported before.[49] VO_2(B) was prepared by three different methods. Methods 1 and 2 involved reduction of the vanadate ions with borohydride or dithionite to obtain nanocrystalline VO_2(B) as reported before.[144] For reduction with borohydride, a vanadate solution was prepared by dissolving V_2O_5 in a LiOH solution followed by lowering the pH to 4 by adding dilute HCl. Then 250 mL of potassium borohydride solution (0.25 M) that was prepared by dissolving KBH_4 in LiOH solution with a pH value of 11-12 was added drop by drop to 50 mL of vanadate solution while sustaining the pH value of the reaction mixture at 4 with the addition of HCl. For reduction with dithionite, 250 mL of 1 M sodium dithionite solution that was prepared by dissolving $Na_2S_2O_4$ in LiOH was added drop by drop to 50 mL of 0.25 M vanadate solution. The reduction products formed were filtered, washed with distilled water, and dried in a convection oven at 120 ^oC, and finally heated in vacuum at 230 ^oC for 2 h. Method 3 involved a hydrothermal process used by Armstrong *et al.*[146] 0.6 g of V_2O_5 powder was stirred with 10 mL of ethylene glycol and

10 mL of distilled water for 1 h to make a suspension. The suspension was then transferred into a 20 mL autoclave jar and heated at 150 ^{o}C for 3 h. The product formed was filtered, washed with distilled water and ethanol, and finally dried in a convection oven at 120 ^{o}C. The $Li[Li_{0.2}Mn_{0.54}Ni_{0.13}Co_{0.13}]O_2 - VO_2(B)$ composite samples were prepared by grinding required amounts of $Li[Li_{0.2}Mn_{0.54}Ni_{0.13}Co_{0.13}]O_2$ and $VO_2(B)$ in a mortar.

7.2.2 Characterization

Characterization procedures for the SEM, TEM, and XRD analyses are described in Chapter 2. Electrochemical data were collected with CR2032 coin cells. The cathodes were fabricated by mixing 75 wt. % active material, 20 wt. % Super P carbon, and 5 wt. % polytetrafluoroethylene (PTFE) binder in a mortar, followed by rolling and cutting into circular electrodes of 0.64 cm^2 area. The electrodes were then pressed into Al mesh current collectors and dried in a vacuum oven overnight at 120 ^{o}C before assembling the coin cells. Coin cells were assembled in a glove box with the synthesized cathodes, lithium foil as a counter electrode, Celgard polypropylene separator, and 1 M $LiPF_6$ in ethylene carbonate (EC)/diethyl carbonate (DEC) (1:1 v/v) electrolyte. The charge-discharge profile, cyclability, and rate capability data were collected with an Arbin battery cycler.

7.3 RESULTS AND DISCUSSION

7.3.1 Structural and morphological analysis

Figure 7.1 shows the XRD patterns of $Li[Li_{0.2}Mn_{0.54}\ Ni_{0.13}Co_{0.13}]O_2$, $VO_2(B)$ synthesized by the three methods, and the $Li[Li_{0.2}Mn_{0.54}\ Ni_{0.13}Co_{0.13}]O_2 - VO_2(B)$ composites with various $VO_2(B)$ content. While the $VO_2(B)$ sample synthesized by the borohydride does not show any impurity peak, the $VO_2(B)$ samples synthesized by the

other two methods show weak reflections corresponding to V_2O_5; since V_2O_5 is also electrochemically active, its presence as a secondary phase is not harmful. The broad reflections of the VO_2(B) samples is indicative of their nanocrystalline nature, but the three samples prepared by the three different methods differ in their degree of crystallinity and crystallite size. Due to the broad and weak nature of the reflections of the nanocrystalline VO_2(B), the $Li[Li_{0.2}Mn_{0.54}\ Ni_{0.13}Co_{0.13}]O_2 - VO_2$(B) composites with low VO_2(B) content show sharp reflections corresponding to mainly the layered oxide. Nevertheless, with a higher content (30 wt. %) of VO_2(B), weak reflections corresponding to VO_2(B) begin to appear as seen in Figure 7.1(g).

The differences in the morphology and particle size among the three samples are also evident in the SEM and TEM photographs shown in Figure 7.2. The sample prepared with borohydride consists of agglomerated nanowires and sub-mircon particles. The sample prepared with sodium dithionite contains only nonowires. The sample prepared by the hydrothermal method consists of agglomerated nanowires and sheets. In all the three samples, the nanowires are 30 – 50 nm in diameter and several microns in length.

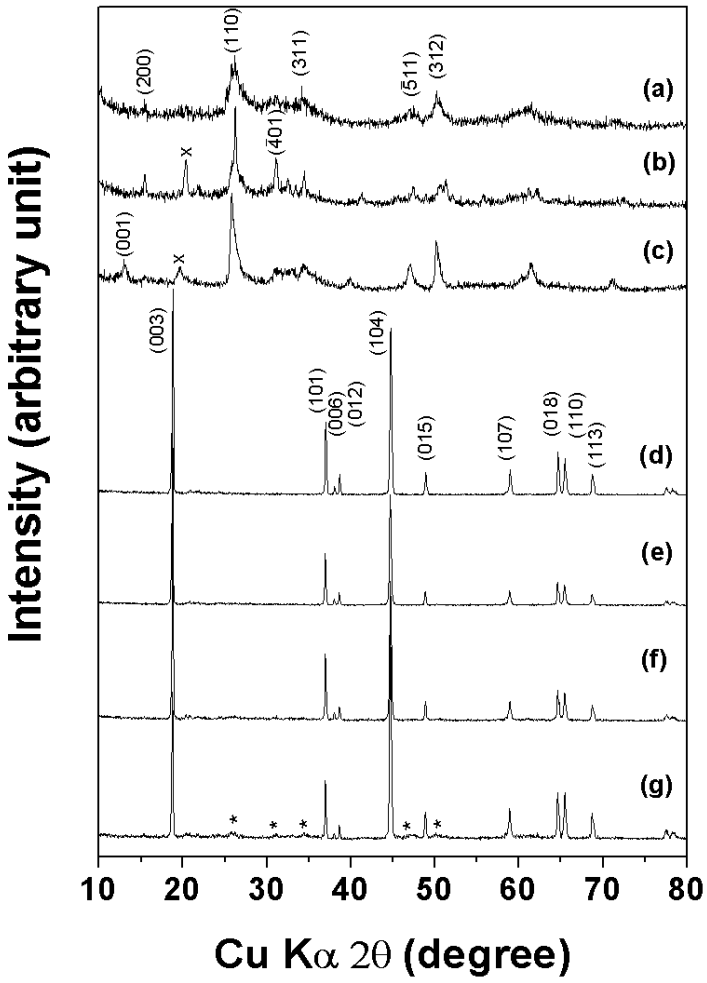

Figure 7.1. XRD patterns of VO_2(B), layered $Li[Li_{0.2}Mn_{0.54}\ Ni_{0.13}Co_{0.13}]O_2$, and $Li[Li_{0.2}Mn_{0.54}\ Ni_{0.13}Co_{0.13}]O_2$ – VO_2(B) composites: (a) VO_2(B) prepared with borohydride, (b) VO_2(B) prepared with sodium dithionite, (c) VO_2(B) prepared by hydrothermal process, (d) layered $Li[Li_{0.2}Mn_{0.54}\ Ni_{0.13}Co_{0.13}]O_2$, (e) 90 wt. % $Li[Li_{0.2}Mn_{0.54}\ Ni_{0.13}Co_{0.13}]O_2$ – 10 wt. % VO_2(B), (f) 80 wt. % $Li[Li_{0.2}Mn_{0.54}\ Ni_{0.13}Co_{0.13}]O_2$ – 20 wt . % VO_2(B), (g) 70 wt. % $Li[Li_{0.2}Mn_{0.54}\ Ni_{0.13}Co_{0.13}]O_2$ – 30 wt. % VO_2(B). The reflections marked with X in (b) and (c) correspond to V_2O_5 and those marked with * in (g) correspond to VO_2(B). The VO_2(B) samples in (e) – (g) were prepared with borohydride.

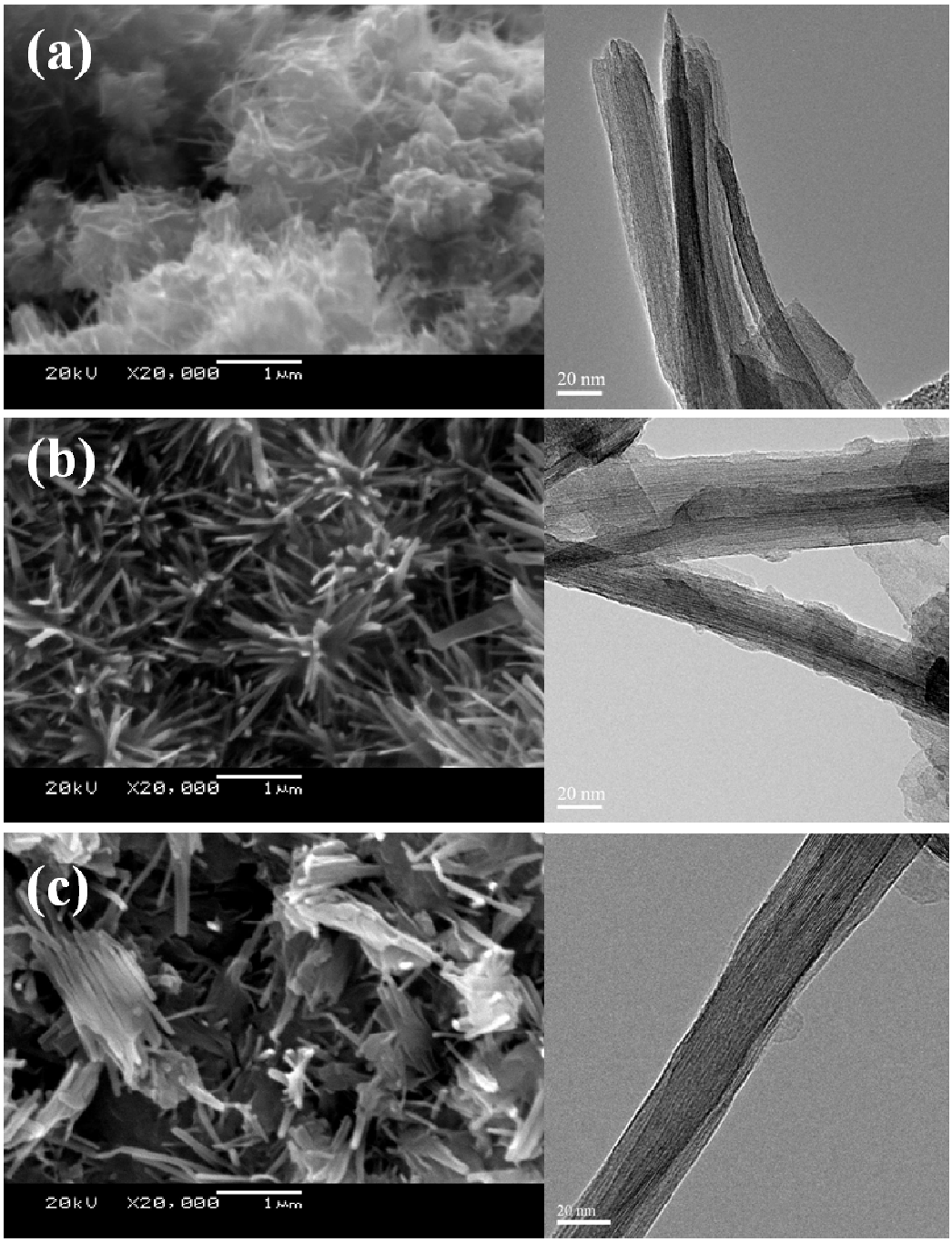

Figure 7.2. SEM and TEM images of the VO_2(B) samples (a) prepared with borohydride, (b) prepared with sodium dithionite, and (c) prepared by hydrothermal process.

7.3.2 Electrochemical characterization

Figure 7.3 shows the first discharge profiles of the VO_2(B) samples synthesized by the three methods at 12.5 mA/g (C/20) between 3.5 and 2 V. The first discharge capacities of the VO_2(B) produced by the three methods are in the range of 228 – 237 mAh/g, with the VO_2(B) prepared by the sodium dithionite reduction method showing the largest capacity of 237 mAh/g and that prepared by the potassium borohydride reduction method showing the lowest capacity of 228 mAh/g. However, the shapes of the discharge profiles of the three samples vary significantly. While the samples prepared by the borohydride and dithionite methods exhibit mainly sloping profiles, the sample prepared by the hydrothermal method shows sloping and plateau profiles. The voltage profiles and capacity values observed for the VO_2(B) samples in this work are similar to those reported before for VO_2(B) in the literature with the same synthesis method.[144, 146]

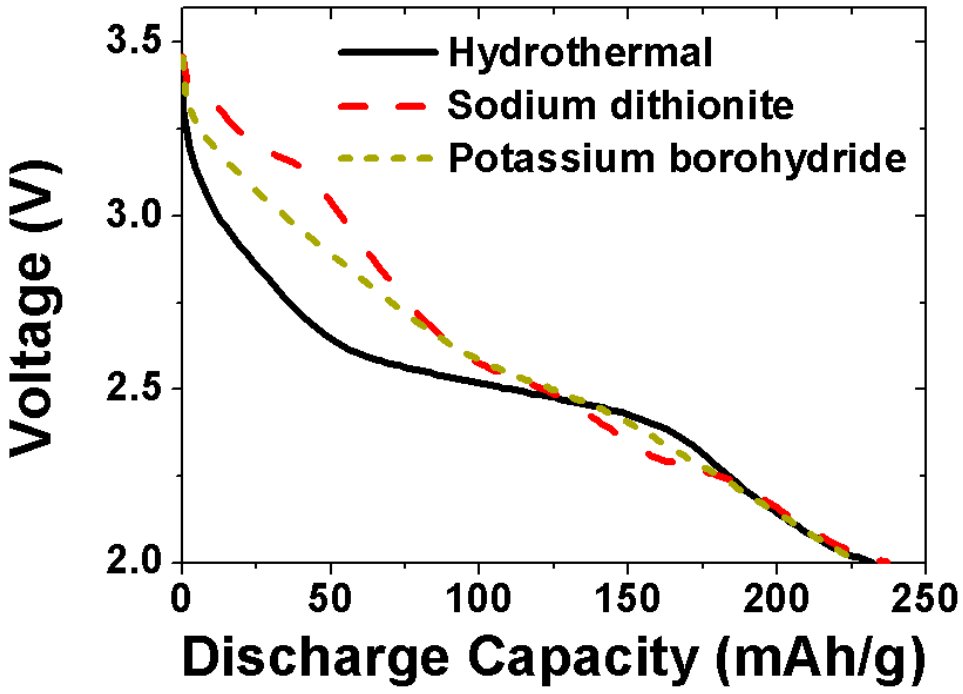

Figure 7.3. First discharge profiles of VO_2(B) synthesized by three different methods.

Figure 7.4 compares the cycle performance data of the VO_2(B) samples synthesized by the three methods. The VO_2(B) sample synthesized by the hydrothermal method shows a continuous fade in capacity during the 25 cycles investigated. On the other hand, the VO_2(B) samples synthesized by the borohydride and dithionite reduction methods show good cyclability after an initial drop between the first and second cycles. Based on these data, the VO_2(B) sample synthesized by the borohydride reduction method was selected for making composite cathodes with $Li[Li_{0.2}Mn_{0.54}\ Ni_{0.13}Co_{0.13}]O_2$, and the data presented in Figs. 7.5 – 7.8 below were collected with these composite cathodes.

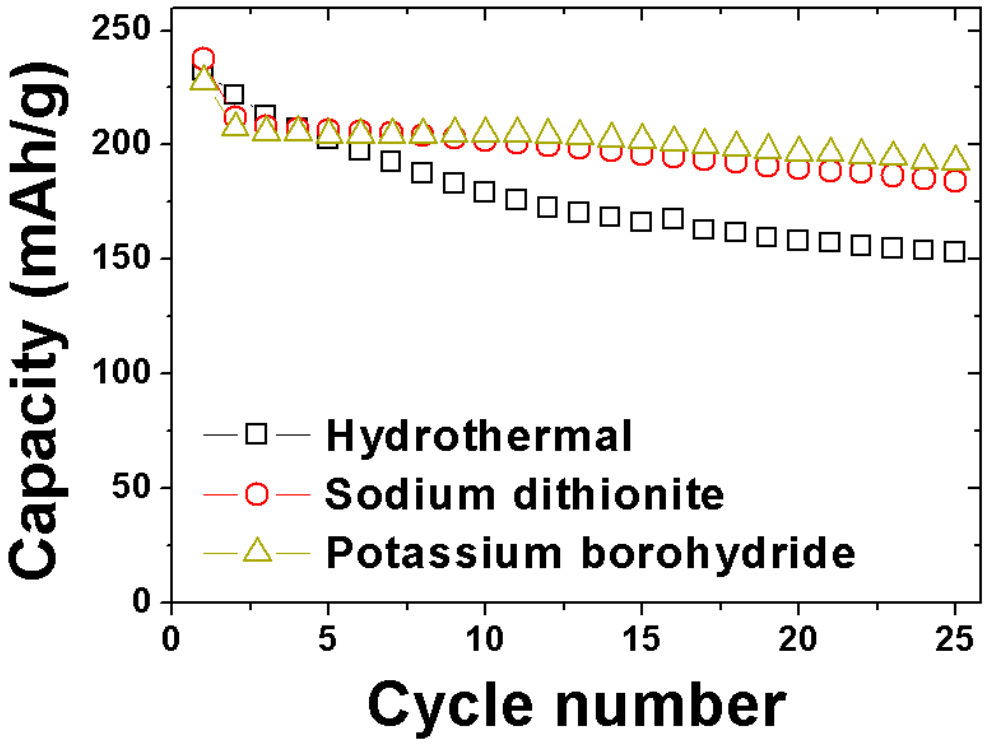

Figure 7.4. Comparison of the cyclabilities (C/20 rate) of VO_2(B) synthesized by three different methods.

Figure 7.5 shows the first charge-discharge profiles of the $Li[Li_{0.2}Mn_{0.54}Ni_{0.13}Co_{0.13}]O_2 - VO_2(B)$ composites with various $VO_2(B)$ content at a constant current of 25 mA/g (C/10) between 2 and 4.8 V. Table 7.1 gives the first charge and discharge capacity values and the irreversible capacity losses in the first cycle, while Figure 7.6 shows the variation of the irreversible capacity loss with $VO_2(B)$ content. The irreversible capacity loss decreases monotonically from 88 mAh/g at 0 wt. % $VO_2(B)$ to -23 mAh/g at 30 wt. % $VO_2(B)$. The decrease in irreversible capacity loss is due to the ability to insert the lithium back into the lithium-free host $VO_2(B)$ in the composite cathodes. The data in Figure 7.6 reveal that the irreversible capacity loss vanishes to zero around 23 wt.% $VO_2(B)$. These observations are consistent with our previous findings with the composite cathodes consisting of layered $Li[Li_{0.2}Mn_{0.54}Ni_{0.13}Co_{0.13}]O_2$ and other lithium-free insertion hosts such as V_2O_5, $Li_4Mn_5O_{12}$, and LiV_3O_8.[57, 58]

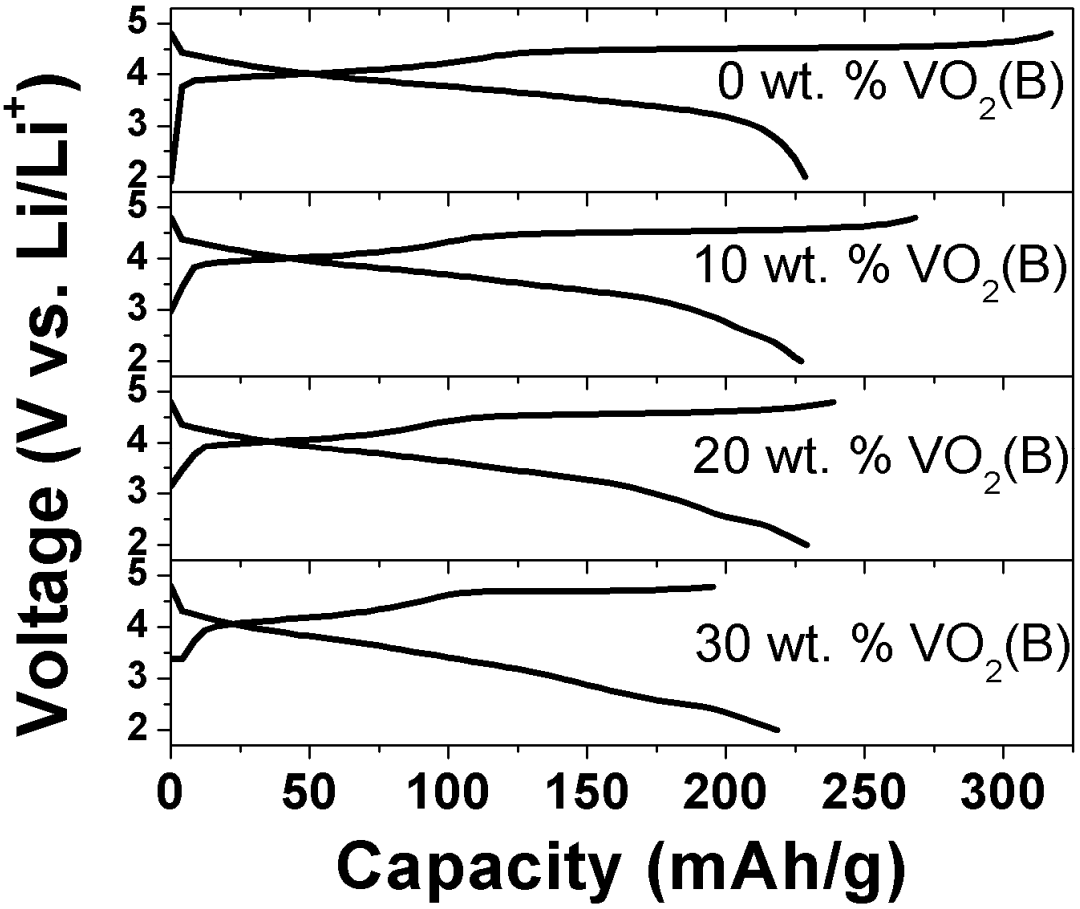

Figure 7.5. First charge-discharge profiles (C/10 rate) of $Li[Li_{0.2}Mn_{0.54}\ Ni_{0.13}Co_{0.13}]O_2 - VO_2(B)$ composite cathodes with various $VO_2(B)$ content. The $VO_2(B)$ sample was prepared by the borohydride method.

Table 7.1 Electrochemical data of layered $Li[Li_{0.2}Mn_{0.54}Ni_{0.13}Co_{0.13}]O_2$ and $Li[Li_{0.2}Mn_{0.54}Ni_{0.13}Co_{0.13}]O_2 - VO_2(B)$ composite cathodes.

$VO_2(B)$ content (wt.%)	First charge capacity (mAh/g)	First discharge capacity (mAh/g)	Irreversible capacity loss (mAh/g)
0	317	229	88
10	268	227	41
20	239	229	10
30	195	218	-23

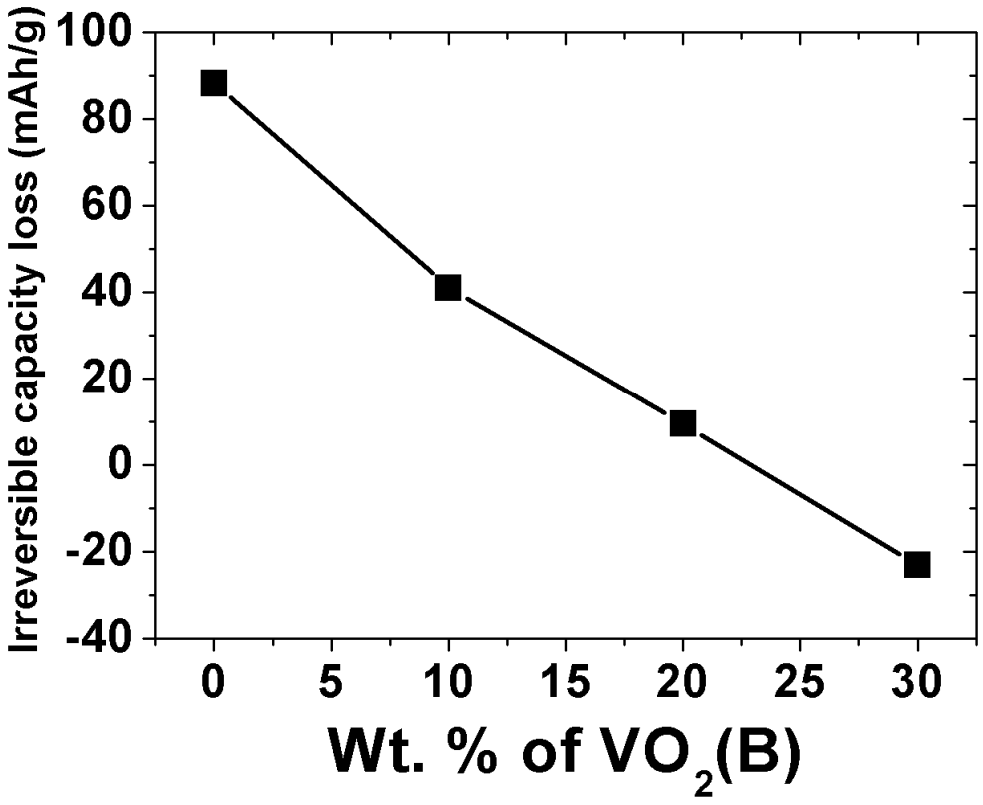

Figure 7.6. Variation of irreversible capacity loss with the VO_2(B) content in the $Li[Li_{0.2}Mn_{0.54}\ Ni_{0.13}Co_{0.13}]O_2$ – VO_2(B) composite cathodes. The VO_2(B) sample was prepared by the borohydride method.

Figure 7.7 compares the cyclabilities of the $Li[Li_{0.2}Mn_{0.54}\ Ni_{0.13}Co_{0.13}]O_2$ – VO_2(B) composite cathodes with variousVO_2(B) content at a constant current of 25 mA/g (C/10) between 2 and 4.8 V. The composite cathodes with up to 20 wt. % VO_2(B) show capacity retention similar to or better than that of pristine layered oxide. The slightly larger fade observed at higher VO_2(B) content could be related to the faster fade of VO_2(B) at higher voltages of up to 4.8 V. VO_2(B) has been found to show better cyclability with HF-free electrolytes like lithium bisoxalatoborate (LiBOB) in propylene carbonate,[146] so further investigation with LIBOB-based electrolytes could show better performance at higher VO_2(B) contents.

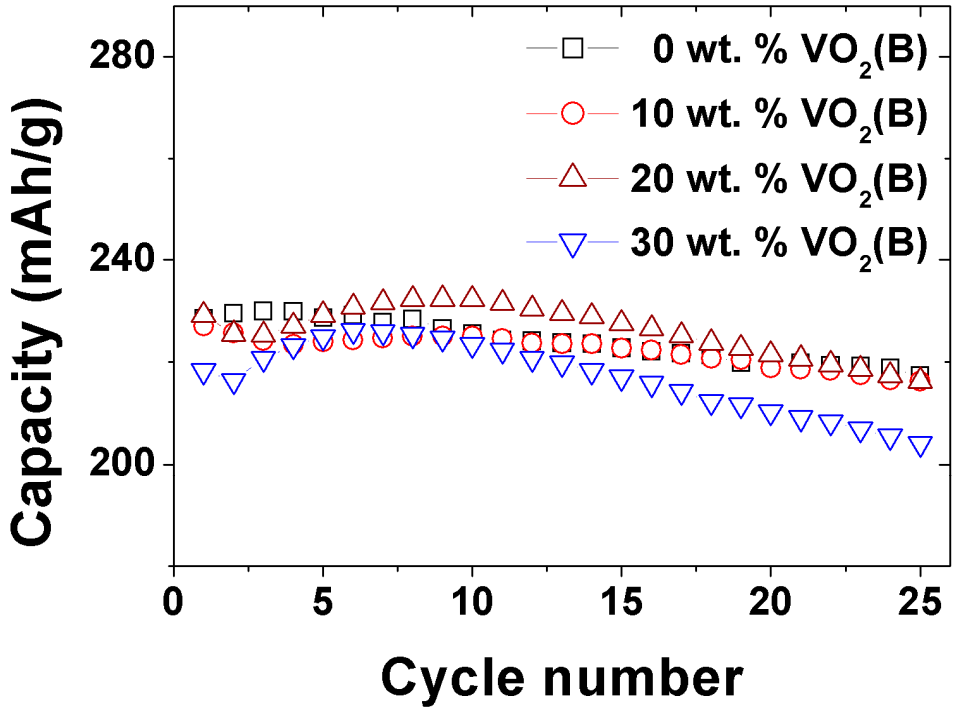

Figure 7.7. Comparison of the cyclabilities (C/10 rate) of the $Li[Li_{0.2}Mn_{0.54}\ Ni_{0.13}Co_{0.13}]O_2$ – VO_2(B) composite cathodes with various VO_2(B) content. The VO_2(B) sample was prepared by the borohydride method.

Figure 7.8 compares the rate capabilities of the $Li[Li_{0.2}Mn_{0.54}\ Ni_{0.13}Co_{0.13}]O_2 - VO_2(B)$ composite cathodes with various $VO_2(B)$ content. The rate capability data were obtained by charging all the coin cells at 12.5 mA/g (C/20 rate) and discharging at 12.5 (C/20), 25 (C/10), 50 (C/5), 250 (1C), and 500 mA/g (2C). The composite cathodes show slightly better rate capability than pristine layered cathode due to the better rate capability of the nanocrystalline $VO_2(B)$ attributed its better electronic and lithium diffusion characteristics. The results demonstrate that the $Li[Li_{0.2}Mn_{0.54}\ Ni_{0.13}Co_{0.13}]O_2 - VO_2(B)$ composite cathodes with an optimum $VO_2(B)$ content can help not only to decrease irreversible capacity loss but also to improve the cyclability and rate capability.

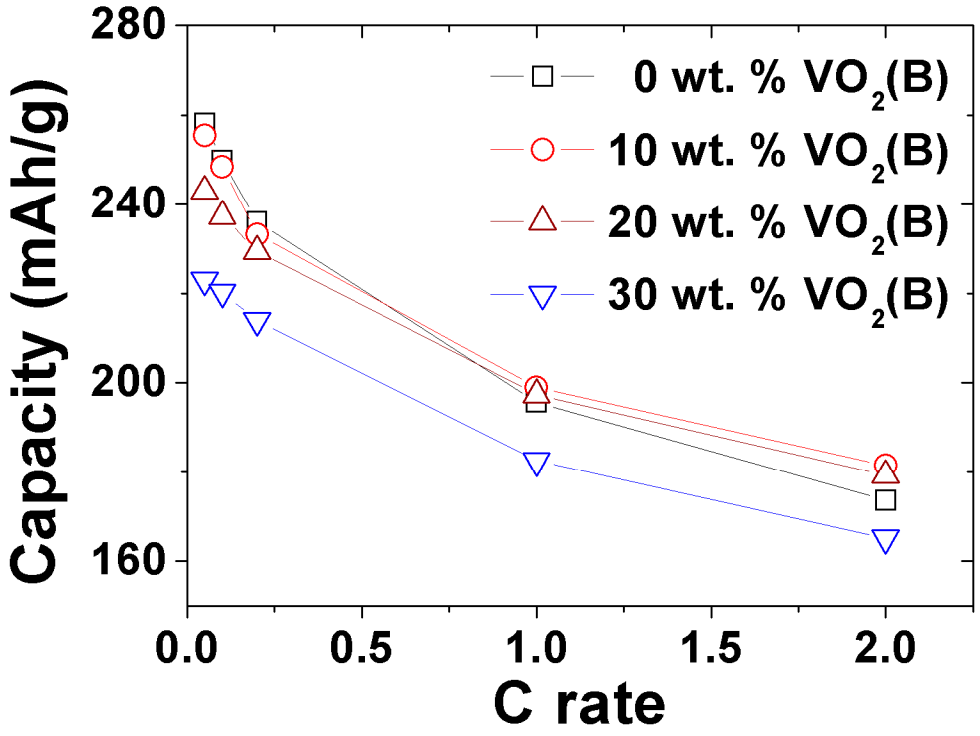

Figure 7.8. Comparison of the rate capabilities of the $Li[Li_{0.2}Mn_{0.54}\ Ni_{0.13}Co_{0.13}]O_2 - VO_2(B)$ composite cathodes with various $VO_2(B)$ content. The $VO_2(B)$ sample was prepared by the borohydride method.

7.4 CONCLUSIONS

The incorporation of the lithium-free insertion host VO_2(B) into the high-capacity layered oxide $Li[Li_{0.2}Mn_{0.54}\ Ni_{0.13}Co_{0.13}]O_2$ decreases the irreversible capacity loss as it can insert the lithium ions that cannot be inserted back into the layered oxide lattice. The irreversible capacity vanishes to zero at ~ 23 wt. % VO_2(B) in the $Li[Li_{0.2}Mn_{0.54}\ Ni_{0.13}Co_{0.13}]O_2 - VO_2$(B) composite cathode. The composite cathodes with an optimum amount of VO_2(B) also exhibit better cyclability and rate capability than the pristine layered oxide. The study demonstrates that blending the high-capacity lithium-rich layered oxide cathode with lithium-free insertion hosts could offer a viable approach to improve their electrochemical performance.

Chapter 8: Improved electrochemical performance of lithium-rich layered oxide cathodes by controlling the first charge process

8.1 INTRODUCTION

As mentioned in Chapter 7, to overcome the drawbacks and improve the electrochemical performances of the high-capacity layered oxide cathodes, various strategies have been pursued. Recently, a completely new approach has been reported wherein electrochemical pre-treatment has also been shown to improve the cyclability of the lithium-rich layered oxides without any chemical processing.[59-61] From our own experience with the lithium-rich layered oxides, we found that the samples exhibiting good electrochemical performance usually show slightly lower first charge capacities (lower number of lithium ions extracted) than the other samples. This analysis prompted an investigation of the effect of controlling the number of lithium ions extracted in the first charge process on the electrochemical performance of the lithium-rich layered oxides. Little information is available about the effect of the first charge capacity on the electrochemical performance of lithium-rich layered oxides, even though the first charge process is critical to the performance of these materials. The high-capacity of these lithium-rich layered oxides is ascribed to the irreversible loss of oxygen from the lattice during the first charge, followed by a lowering of the oxidation state of the transition-metal ions at the end of first discharge[44]. Accordingly, we present here the electrochemical performance variations of three lithium-rich layered oxides, $Li[Li_{0.2}Mn_{0.54}Ni_{0.13}Co_{0.13}]O_2$, $Li[Li_{0.2}Mn_{0.6}Ni_{0.17}Co_{0.03}]O_2$, and $Li[Li_{0.2}Mn_{0.6}Ni_{0.2}]O_2$, as a function of the amount of lithium ions extracted during the first charge process.

8.2 EXPERIMENTAL

8.2.1 Synthesis

Three lithium-rich layered oxides, $Li[Li_{0.2}Mn_{0.54}Ni_{0.13}Co_{0.13}]O_2$, $Li[Li_{0.2}Mn_{0.6}Ni_{0.17}Co_{0.03}]O_2$, and $Li[Li_{0.2}Mn_{0.6}Ni_{0.2}]O_2$, were synthesized by firing required amounts of the mixed metal hydroxides of Mn, Ni, and Co and lithium hydroxide, respectively, at 900, 800, and 900 $^{\circ}C$ for 12 h in air. The mixed metal hydroxides were obtained by a co-precipitation method involving the addition of the required amounts of the aqueous metal acetate solutions of Mn, Ni, and Co drop-wise into a 2 M KOH solution under continuous stirring, as described in Chapter 2.

8.2.2 Characterization

Characterization procedures for XRD and electrochemical performance analyses are described in Chapter 2.

8.3 RESULT AND DISCUSSION

8.3.1 Structural analysis

The XRD patterns of the pristine $Li[Li_{0.2}Mn_{0.54}Ni_{0.13}Co_{0.13}]O_2$, $Li[Li_{0.2}Mn_{0.6}Ni_{0.17}Co_{0.03}]O_2$, and $Li[Li_{0.2}Mn_{0.6}Ni_{0.2}]O_2$ are shown in Figure 8.1. The XRD patterns of all compositions correspond to a Li_2MnO_3-type single-phase solid solution with C2/m monoclinic symmetry and multiple planar defects.[128] The weak and broad reflections appearing around 20.5 – 22.5° are due to the ordering of the Li^+, Ni^{2+}, and Mn^{4+} ions in the transition metal layer.[39, 123, 124, 126-128] The lattice parameter values obtained with the C2/m monoclinic symmetry of the three samples are listed in Table 8.1. The lattice parameters increase with decreasing cobalt content due to the substitution of larger Ni^{2+} for smaller Co^{3+}.

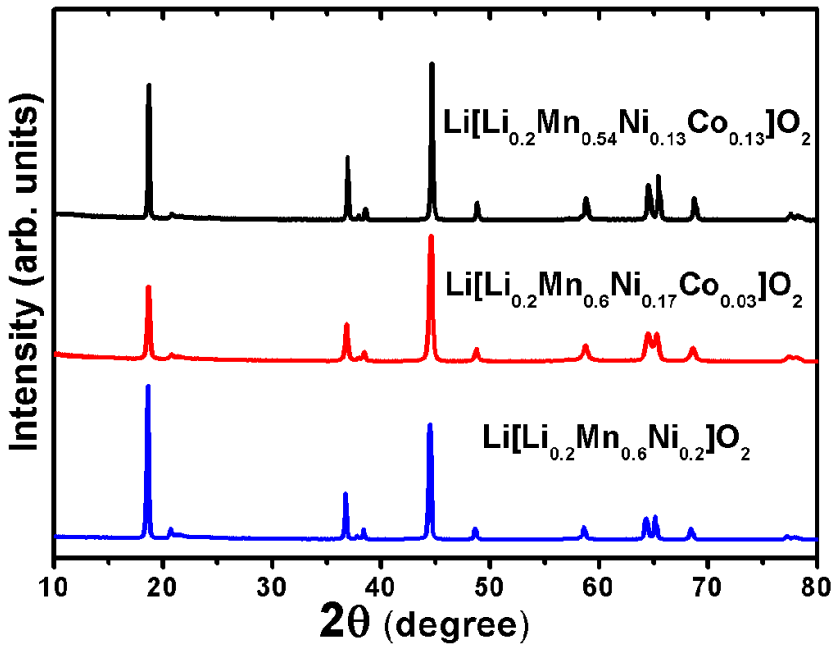

Figure 8.1. XRD patterns of the pristine $Li[Li_{0.2}Mn_{0.54}Ni_{0.13}Co_{0.13}]O_2$, $Li[Li_{0.2}Mn_{0.6}Ni_{0.17}Co_{0.03}]O_2$, and $Li[Li_{0.2}Mn_{0.6}Ni_{0.2}]O_2$ samples.

Table 8.1 Lattice parameters of the lithium-rich layered oxide samples with the C2/m monoclinic symmetry.

Sample	a (Å)	b (Å)	c (Å)	β (°)
$Li[Li_{0.2}Mn_{0.54}Ni_{0.13}Co_{0.13}]O_2$	4.9376(3)	8.5491(5)	5.0237(3)	109.23
$Li[Li_{0.2}Mn_{0.6}Ni_{0.17}Co_{0.03}]O_2$	4.9456(5)	8.5783(8)	5.0263(6)	109.17
$Li[Li_{0.2}Mn_{0.6}Ni_{0.2}]O_2$	4.9580(4)	8.5791(8)	5.0379(6)	109.24

8.3.2 Electrochemical characterization

8.3.2.1 $Li[Li_{0.2}Mn_{0.54}Ni_{0.13}Co_{0.13}]O_2$

The first and second charge-discharge profiles of the $Li[Li_{0.2}Mn_{0.54}Ni_{0.13}Co_{0.13}]O_2$ sample with and without controlling the number of lithium ions extracted during first charge between 2.0 and 4.8 V at a current density of 10 mA/g (C/25 rate based on a capacity of ~ 250 mAh/g) are shown in Figure 8.2. The number of lithium ions extracted during first charge was controlled to 0.8, 0.9, and 1.0 by limiting the first charge capacity to, respectively, 252, 283, and 314 mAh/g. For a comparison, the charge-discharge profiles obtained by charging to the conventional cutoff charge voltage of 4.8 V in the first cycle, which corresponds to a capacity of 336 mAh/g, are also shown in Figure 8.2. The differential capacity (dQ/dV) plots from the first and second charge profiles in Figure 8.2 are compared in Figure 8.3. Significant differences can be seen among the four plots involving different degrees of lithium extraction during first charge. All samples show distinctly different first charge and discharge profiles as has been reported previously in the literature.[55] During the initial charging, the voltage gradually increases up to ~ 4.5 V with a sloping profile as the transition metal ions are oxidized to a 4+ state[42, 43]. The subsequent plateau region that begins around 4.5 V corresponds predominantly to the extraction of lithium ions from the lattice that is accompanied by an oxidation of O^{2-} ions to oxygen and possibly to a partial extraction of lithium ions by the Li^+/H^+ exchange at room temperature.[44, 131-133, 147, 148] During the first discharge, the voltage gradually decreases down to 2 V without any plateau region as the transition metal ions are reduced from the 4+ state.[55] Interestingly, during the second charge process, only the cells that had a controlled amount of lithium extraction during first charge show the plateau region again although it is shorter than that of the first charge, as indicated by the small peak at 4.54 V in Figure 8.3, since the oxygen loss reaction could

not be completed under the controlled first charge process. As the number of lithium ions extracted during first charge increases, the height and area of the dQ/dV peak at 4.54 V decreases. The peak at 4.54 V disappears completely for the cell that was charged to the 4.8 V cut-off during first charge.

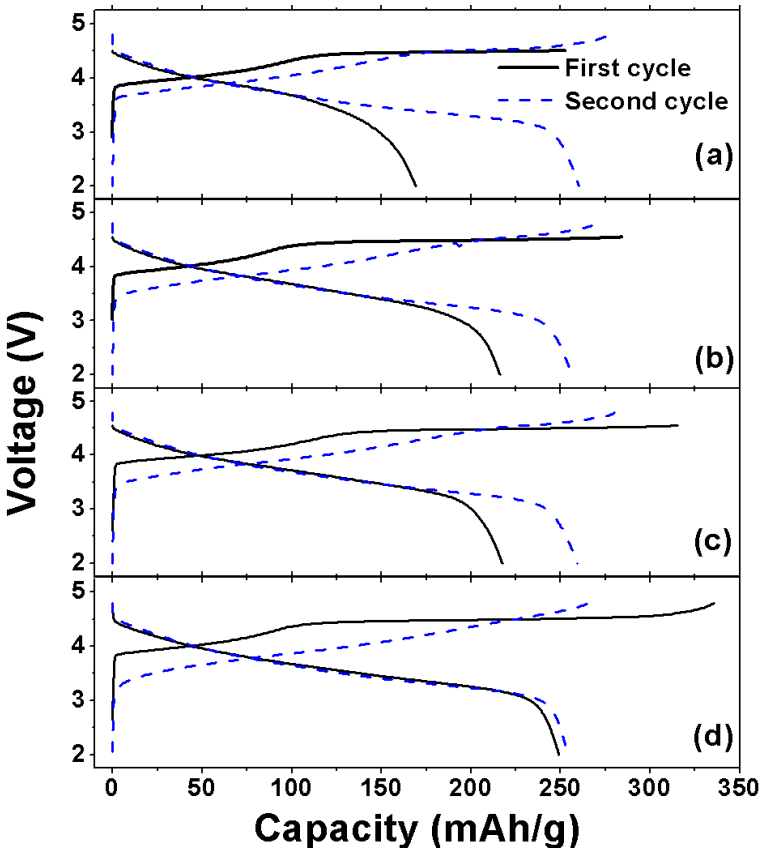

Figure 8.2. The first and second cycle charge-discharge profiles of the $Li[Li_{0.2}Mn_{0.54}Ni_{0.13}Co_{0.13}]O_2$ sample with and without controlling the number of lithium ions extracted during the first charge and then cycled between 2.0 and 4.8 V in the second cycle at a current density of 10 mA/g (C/25 rate): (a) 0.8 Li^+ extracted during first charge, (b) 0.9 Li^+ extracted during first charge, (c) 1.0 Li^+ extracted during first charge, and (d) 4.8 V cut-off during first charge.

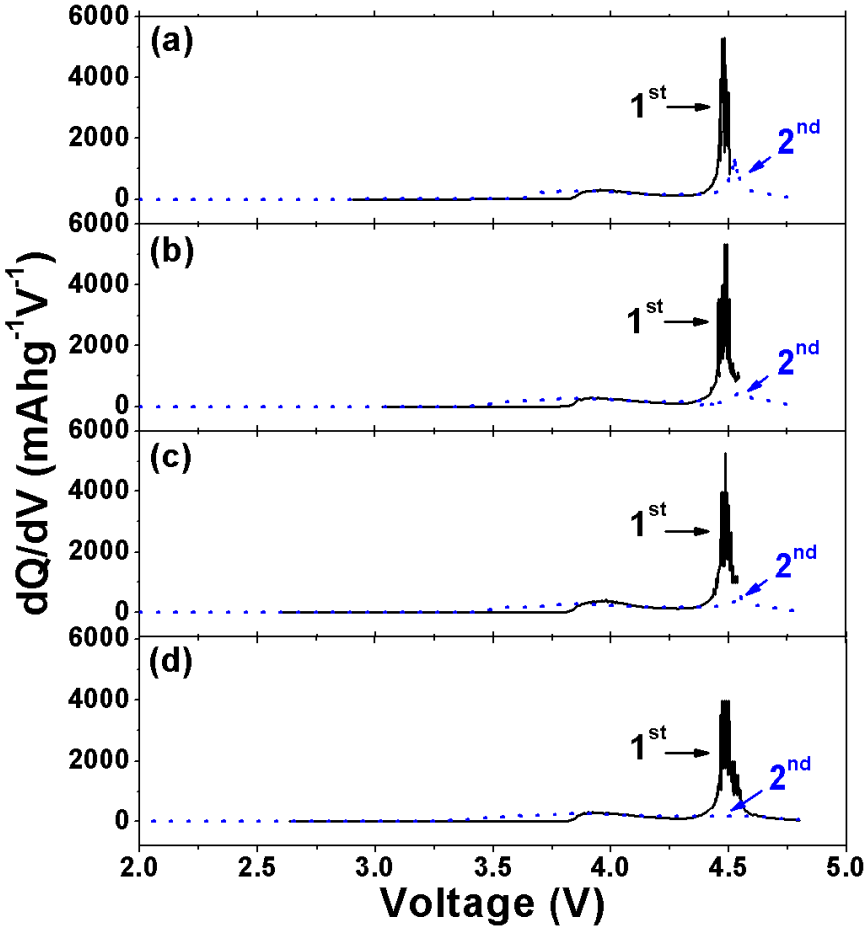

Figure 8.3. Differential capacity (dQ/dV) plots of the first and second charge processes of the $Li[Li_{0.2}Mn_{0.54}Ni_{0.13}Co_{0.13}]O_2$ sample with and without controlling the number of lithium ions extracted during the first charge and then cycled between 2.0 and 4.8 V in the second cycle at a current density of 10 mA/g (C/25 rate): (a) 0.8 Li^+ extracted during first charge, (b) 0.9 Li^+ extracted during first charge, (c) 1.0 Li^+ extracted during first charge, and (d) 4.8 V cut-off during first charge.

The charge capacity, discharge capacity, and C_{irr} values for the first and second cycles depicted in Figure 8.2 are summarized in Table 8.2. The first discharge capacity increases with increasing fraction of lithium ions extracted during the first charge process from 169 to 249 mAh/g. Nevertheless, all samples show similar second discharge capacities of 254 – 260 mAh/g. This indicates that the reversible capacity is not affected by the number of lithium ions extracted during the first charge process for the $Li[Li_{0.2}Mn_{0.54}Ni_{0.13}Co_{0.13}]O_2$ sample; however, the C_{irr} value differs depending on the first charge process. The cell with an extraction of 0.9 lithium ions during first charge shows the lowest total (first and second cycles together) C_{irr} value of 82 mAh/g, while the cell with an extraction of 1.0 lithium shows the highest C_{irr} value of 119 mAh/g.

Table 8.2 Electrochemical data of the lithium-rich layered oxide samples with and without controlling the number of lithium ions extracted during the first charge process.

Sample	First cycle capacity				Second cycle capacity				Irreversible capacity loss, C_{irr}		
	Charge		Discharge		Charge		Discharge		First cycle	Second cycle	First + second cycle
	Number of Li^+ extracted	mAh/g	Number of Li^+ inserted	mAh/g	Number of Li^+ extracted	mAh/g	Number of Li^+ inserted	mAh/g	mAh/g		
$Li[Li_{0.2}Mn_{0.54}Ni_{0.13}Co_{0.13}]O_2$ Controlled	0.8	251	0.54	169	0.88	277	0.83	260	83	17	100
	0.9	283	0.69	216	0.86	270	0.82	256	68	14	82
	1.0	316	0.69	218	0.89	280	0.82	259	98	21	119
$Li[Li_{0.2}Mn_{0.54}Ni_{0.13}Co_{0.13}]O_2$ 4.8 V Cut-Off	1.07	336	0.79	249	0.85	266	0.81	254	87	12	99
$Li[Li_{0.2}Mn_{0.6}Ni_{0.17}Co_{0.03}]O_2$ Controlled	0.9	283	0.68	215	0.92	289	0.88	278	68	11	79
$Li[Li_{0.2}Mn_{0.6}Ni_{0.17}Co_{0.03}]O_2$ 4.8 V Cut-Off	1.11	348	0.83	262	0.86	271	0.82	257	86	14	100
$Li[Li_{0.2}Mn_{0.6}Ni_{0.2}]O_2$ Controlled	0.9	284	0.67	212	0.81	255	0.80	251	72	4	76
$Li[Li_{0.2}Mn_{0.6}Ni_{0.2}]O_2$ 4.8 V Cut-Off	1.0	316	0.75	234	0.77	242	0.75	235	80	7	87

The cyclability plots of the $Li[Li_{0.2}Mn_{0.54}Ni_{0.13}Co_{0.13}]O_2$ samples with and without the controlled lithium ion extraction between 2.0 and 4.8 V at a current density of 10 mA/g (C/25 rate) are shown in Figure 8.4. All cells show similar cyclability with a discharge capacity of ~ 247 mAh/g at the 50th cycle. The rate capabilities of the $Li[Li_{0.2}Mn_{0.54}Ni_{0.13}Co_{0.13}]O_2$ samples with and without controlled lithium ion extraction are compared in Figure 8.5. Rate capabilities were evaluated by charging at a fixed current density of 10 mA/g (C/25 rate) and discharging at various C rates. All the cells with controlled lithium extraction during first charge display enhanced rate capability compared to the cell with the 4.8 V cut-off charging during first charge.

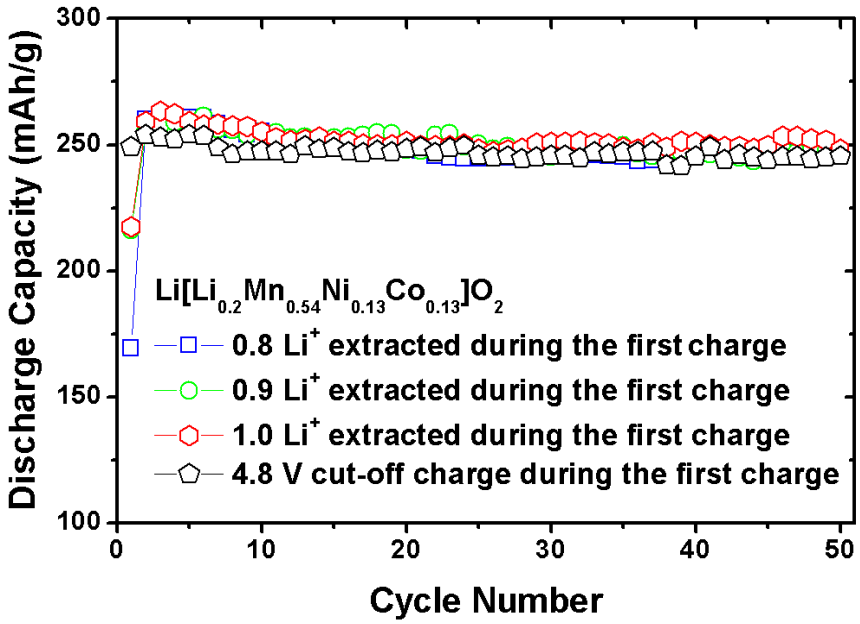

Figure 8.4 Cyclability data of the $Li[Li_{0.2}Mn_{0.54}Ni_{0.13}Co_{0.13}]O_2$ sample with and without controlling the number of lithium ions extracted during the first charge and then cycled between 2.0 and 4.8 V in the subsequent cycles at a current density of 10 mA/g (C/25 rate).

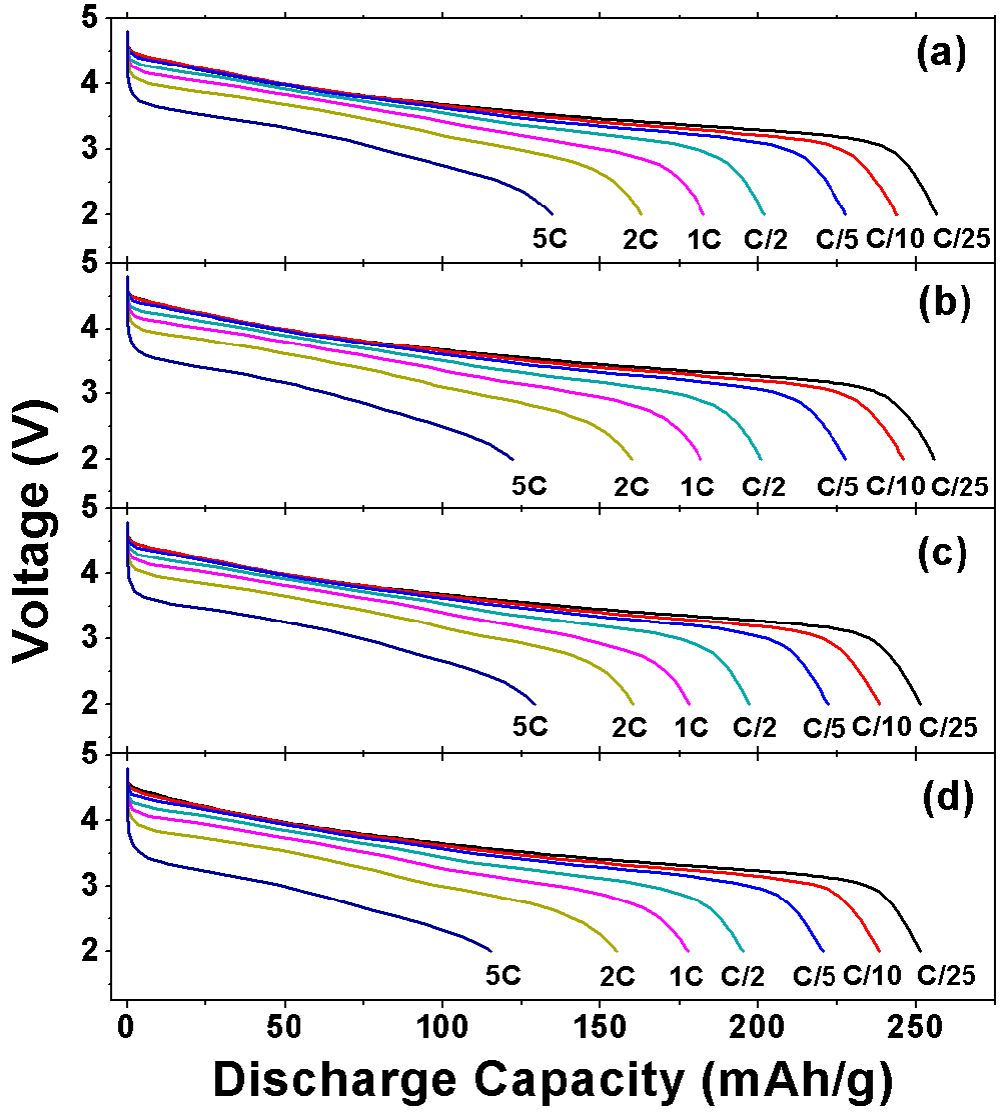

Figure 8.5 Discharge profiles of the $Li[Li_{0.2}Mn_{0.54}Ni_{0.13}Co_{0.13}]O_2$ sample with and without controlling the number of lithium ions extracted during the first charge at various C rates: (a) 0.8 Li^+ extracted during first charge, (b) 0.9 Li^+ extracted during first charge, (c) 1.0 Li^+ extracted during first charge, and (d) 4.8 V cut-off during first charge.

Cyclability and rate capability data were also obtained with a higher charge voltage limit (5.0 V) to investigate more clearly the effectiveness of controlling the fraction of lithium ions extracted in the first charge. The sample with an extraction of 0.9 lithium ions during the first charge was selected for comparison because it had the lowest C_{irr} and a similar reversible discharge capacity with other samples. Figures 8.6 and 8.7 compare the cyclability and rate capability data of the cells with a 5.0 V cut-off and an extraction of 0.9 lithium ions during the first charge. The cell with an extraction of 0.9 lithium ions during the first charge exhibits higher discharge capacity from the 2^{nd} cycle to the 50^{th} cycle at both 10 and 25 mA/g current densities (C/25 and C/10 rates). In addition, the cell with an extraction of 0.9 lithium ions during the first charge shows enhanced rate capability compared to the cell with a 5.0 V cut-off during first charge. Thus, the effect of controlling the amount of lithium ions extracted during the first charge process is demonstrated more clearly with a higher charge voltage limit condition.

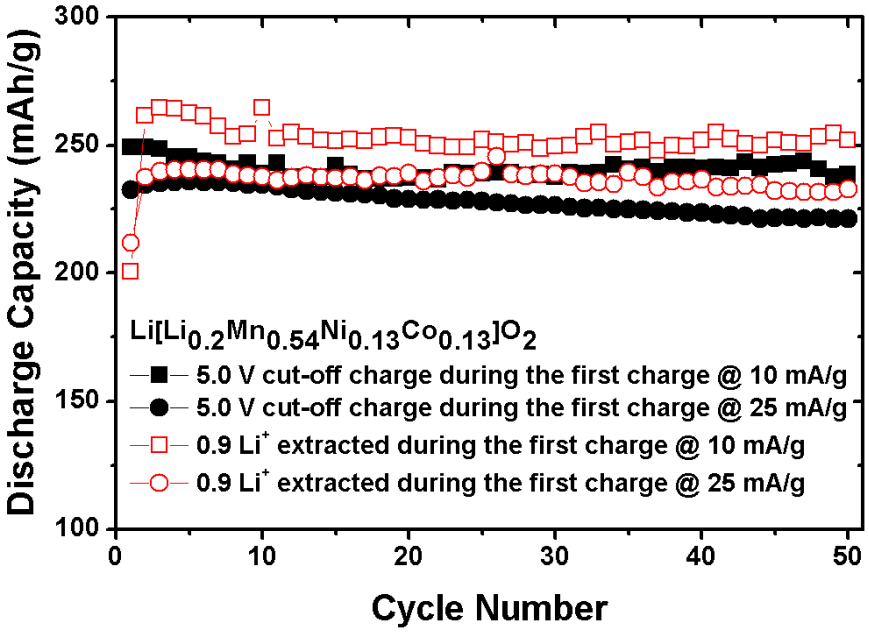

Figure 8.6 Cyclability data of the $Li[Li_{0.2}Mn_{0.54}Ni_{0.13}Co_{0.13}]O_2$ sample with 5.0 V cut-off and an extraction of 0.9 Li^+ during the first charge and then cycled between 2.0 and 5.0 V in the subsequent cycles at a current density of 10 mA/g (C/25 rate) and 25 mA/g (C/10 rate).

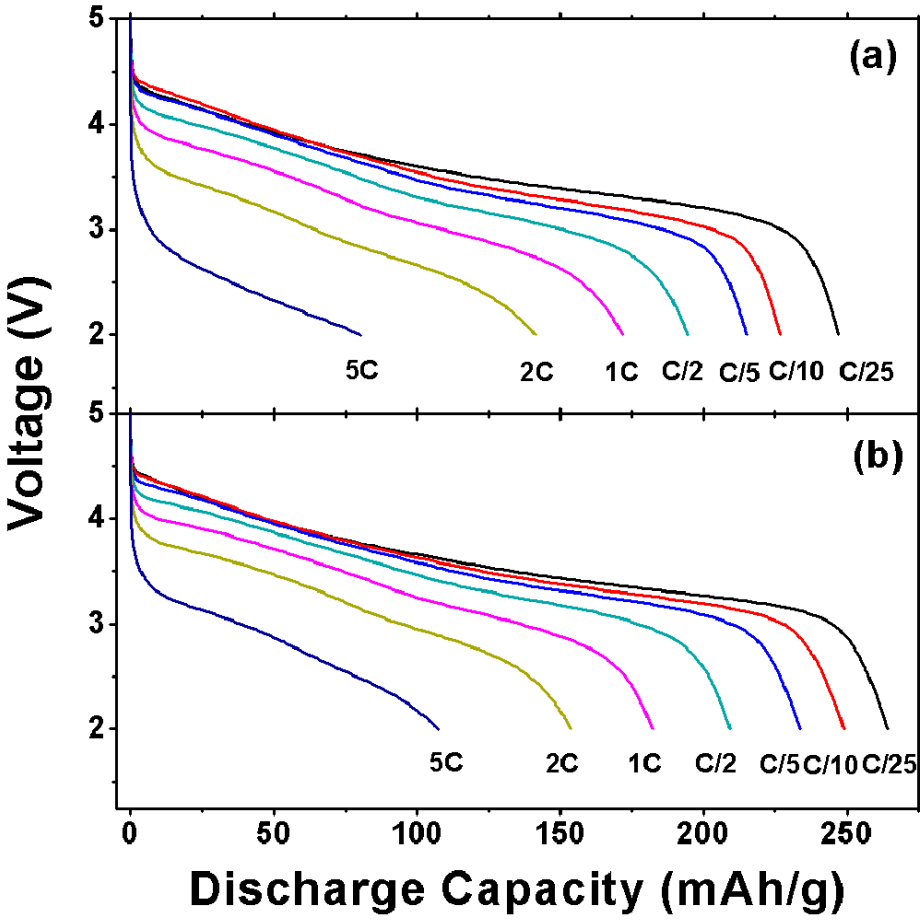

Figure 8.7 Discharge profile of the $Li[Li_{0.2}Mn_{0.54}Ni_{0.13}Co_{0.13}]O_2$ sample at various C rates: (a) 5.0 V cut-off and (b) 0.9 Li^+ extracted during the first charge.

8.3.2.2 $Li[Li_{0.2}Mn_{0.6}Ni_{0.17}Co_{0.03}]O_2$ and $Li[Li_{0.2}Mn_{0.6}Ni_{0.2}]O_2$

The effects of controlling the amount of lithium ions extracted during the first charge process have also been investigated for two other lithium-rich layered oxides, $Li[Li_{0.2}Mn_{0.6}Ni_{0.17}Co_{0.03}]O_2$ and $Li[Li_{0.2}Mn_{0.6}Ni_{0.2}]O_2$. The first and second cycle charge-discharge profiles of the $Li[Li_{0.2}Mn_{0.6}Ni_{0.17}Co_{0.03}]O_2$ and $Li[Li_{0.2}Mn_{0.6}Ni_{0.2}]O_2$ samples with a 4.8 V cut-off and 0.9 lithium ions extracted during the first charge between 2.0 and 4.8 V at a current density of 10 mA/g (C/25 rate) are shown in Figure 8.8. The charge capacity, discharge capacity, and C_{irr} values of the first and second cycles are summarized in Table 8.2. In contrast to the $Li[Li_{0.2}Mn_{0.54}Ni_{0.13}Co_{0.13}]O_2$ sample, the cells with controlled first charge show not only low C_{irr}, but also higher second cycle discharge capacities for these two compositions. The cells with an extraction of 0.9 lithium ions during the first charge process exhibit discharge capacities that are 21 and 16 mAh/g higher in the second cycle (278 and 251mAh/g) than the cells with 4.8 V cut-off (257 and 235mAh/g), respectively, for the $Li[Li_{0.2}Mn_{0.6}Ni_{0.17}Co_{0.03}]O_2$ and $Li[Li_{0.2}Mn_{0.6}Ni_{0.2}]O_2$ samples. They also have 21 mAh/g ($Li[Li_{0.2}Mn_{0.6}Ni_{0.17}Co_{0.03}]O_2$) and 11 mAh/g ($Li[Li_{0.2}Mn_{0.6}Ni_{0.2}]O_2$) lower C_{irr} values during the first and second cycles compared to the cells with a 4.8 V cut-off charge. The cyclability plots of the $Li[Li_{0.2}Mn_{0.6}Ni_{0.17}Co_{0.03}]O_2$ and $Li[Li_{0.2}Mn_{0.6}Ni_{0.2}]O_2$ samples with a 4.8 V cut-off and an extraction of 0.9 lithium ions during the first charge between 2.0 and 4.8 V at a current density of 10 mA/g (C/25 rate) are shown in Figure 8.9. For both compositions, the cells with an extraction of 0.9 lithium ions during the first charge show higher discharge capacities from the 2^{nd} to 50^{th} cycle with better capacity retentions compared to the cell with 4.8 V cut-off. The electrochemical data collected with all the three lithium-rich layered oxide compositions support the argument that controlling the number of lithium

ions extracted during the first charge process is an effective method to improve their electrochemical performances.

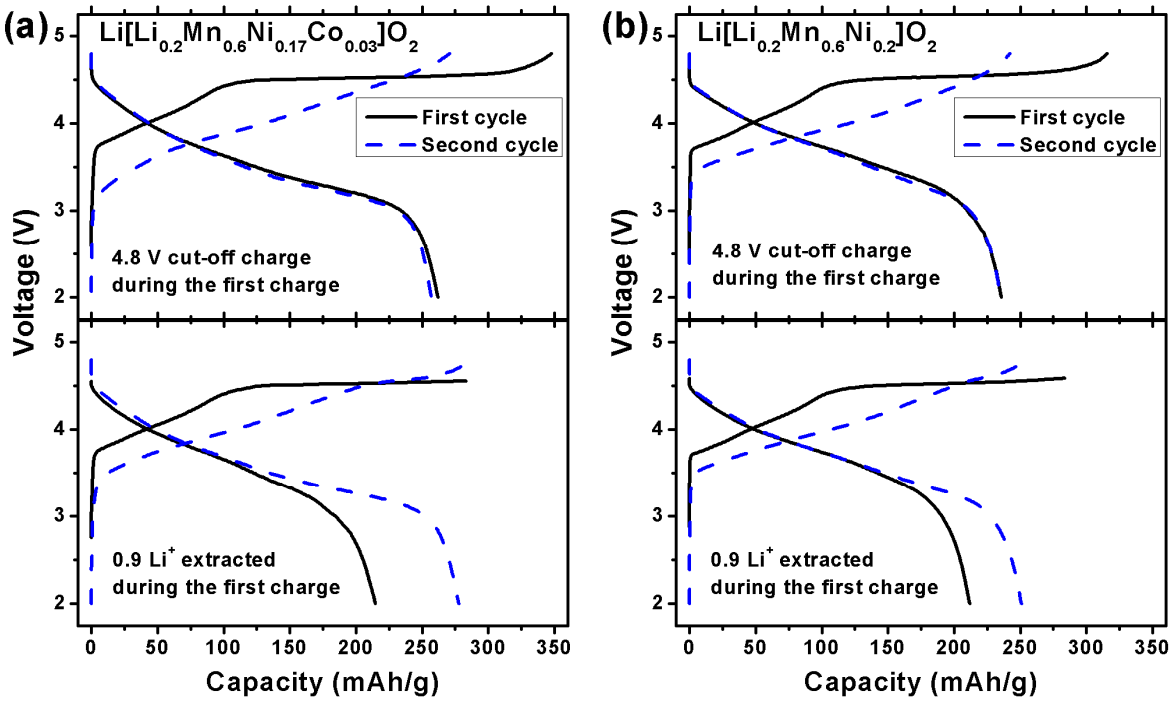

Figure 8.8. The first and second cycle charge-discharge profiles of lithium-rich layered oxides with 4.8 V cut-off and 0.9 Li^+ extracted during the first charge and then cycled between 2.0 and 4.8 V in the second cycle at a current density of 10 mA/g (C/25 rate): (a) $Li[Li_{0.2}Mn_{0.6}Ni_{0.17}Co_{0.03}]O_2$ and (b) $Li[Li_{0.2}Mn_{0.6}Ni_{0.2}]O_2$.

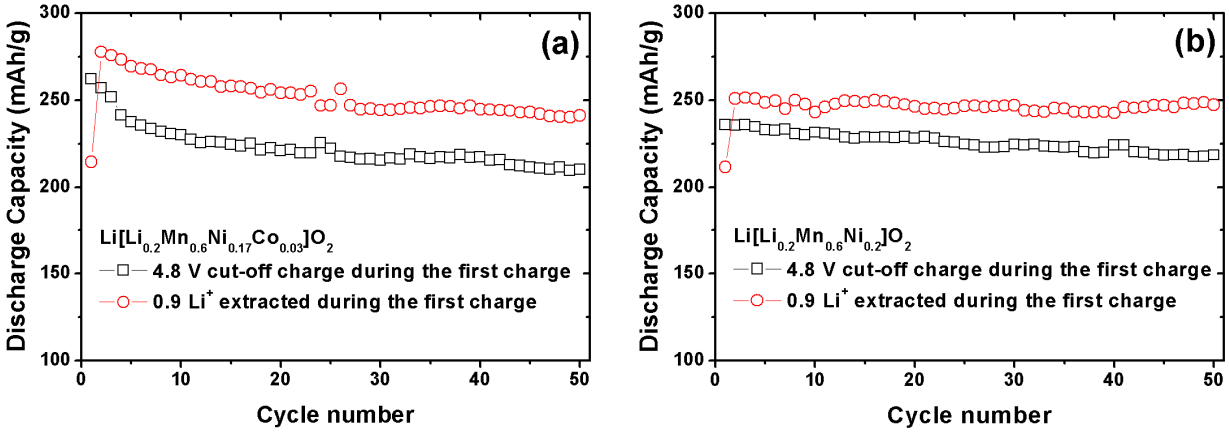

Figure 8.9. Cyclability data of the lithium-rich layered oxides with 4.8 V cut-off and 0.9 Li^+ extracted during first charge and then cycled between 2.0 and 4.8 V in the subsequent cycles at a current density of 10 mA/g (C/25 rate): (a) $Li[Li_{0.2}Mn_{0.6}Ni_{0.17}Co_{0.03}]O_2$ and (b) $Li[Li_{0.2}Mn_{0.6}Ni_{0.2}]O_2$.

8.3.3 Origin of improved electrochemical performances

As discussed above, the samples with the controlled first charge process show better electrochemical performance in terms of discharge capacity, C_{irr}, cyclability, and rate capability. With an aim to understand the observed improvement in electrochemical performance resulting from the controlled first charge process, we have considered both the suppression of side reactions and oxide-ion vacancy elimination.

As mentioned earlier, the plateau region around 4.5 V during the first charge process corresponds to the extraction of lithium ions from the lattice, both by the oxidation of O^{2-} ions to oxygen and the Li^+/H^+ exchange.[44, 131-133, 147, 148] According to the reports of Bruce's group, during the plateau region, lithium ions are extracted mainly by the oxidation of O^{2-} ions to oxygen; however, Li^+/H^+ exchange was found to dominate at high levels of lithium ion extraction.[132, 147, 148] The protons originate from the decomposition of the PF_6^- based electrolyte solution, which invariably results in the formation of HF. With the controlled first charge process, it may be possible to suppress this side reaction during the first charge process through the diminished plateau region around 4.5 V. In other words, a lower number of lithium ions extracted could suppress Li^+/H^+ exchange reaction during the first charge process.

In addition, the retention of more oxide ion vacancies in the layered oxide[48, 49, 54] with the controlled first charge process could also contribute to the better electrochemical properties. The calculated nominal compositions of each sample with an extraction of 0.9 lithium ions during the first charge and a 4.8 V cut-off at a current density of 10 mA/g (C/25 rate) are summarized in Table 8.3. We demonstrate these calculations below using the data of the $Li[Li_{0.2}Mn_{0.6}Ni_{0.2}]O_2$ sample from Table 8.2 and Figure 8.8(b), as an example. First, we will illustrate the oxide-ion vacancy retention after the second cycle

with the 4.8 V cut-off cell. Assuming no side reactions with the electrolyte, the first charge capacity (316 mAh/g) corresponds to an extraction of 1.002 lithium ions from the lattice per formula unit. Of this fraction, 0.4 lithium ions can be attributed to the oxidation of Ni^{2+} to Ni^{4+} [120] as

$$Li[Li_{0.2}M_{0.8}]O_2 \rightarrow Li_{0.6}[Li_{0.2}M_{0.8}]O_2 + 0.4\ Li^+ + 0.4\ e^- \qquad (1)$$

For simplicity, $Li[Li_{0.2}Mn_{0.6}Ni_{0.2}]O_2$ is represented as $Li[Li_{0.2}M_{0.8}]O_2$, with M representing Mn and Ni. The extraction of the remaining 0.602 lithium ions occurs as a result of the oxidation of O^{2-} ions to oxygen as

$$Li_{0.6}[Li_{0.2}M_{0.8}]O_2 \rightarrow [Li_{0.198\ \ 0.002}M_{0.8}]O_{1.7\ \ 0.3} + 0.602\ Li^+ + 0.602\ e^- + 0.15\ O_2 \qquad (2)$$

At the end of the first charge, the migration of lithium ions from the transition metal layer to the lithium layer, combined with the partial elimination of oxide ion vacancies in the transition metal layer, results in the formation of $Li_{0.125}[Li_{0.073}M_{0.8}]O_{1.7\ \ 0.047}$ as

$$[Li_{0.198\ \ 0.002}M_{0.8}]O_{1.7\ \ 0.3} \rightarrow Li_{0.125}[Li_{0.073\ \ 0.127}M_{0.8}]O_{1.7\ \ 0.3}$$
$$\rightarrow Li_{0.125}[Li_{0.073}M_{0.8}]O_{1.7\ \ 0.047} \qquad (3)$$

The composition at the end of the first discharge can be obtained from the observed first discharge capacity (234 mAh/g), which corresponds to the insertion of 0.748 lithium ions into the lattice.

$$Li_{0.125}[Li_{0.073}M_{0.8}]O_{1.7\ \ 0.047} + 0.748\ Li^+ + 0.748\ e^- \rightarrow Li_{0.873}[Li_{0.073}M_{0.8}]O_{1.7\ \ 0.047} \qquad (4)$$

Due to the absence of the oxidation reaction of O^{2-} ions during the second charge process, the compositions at the end of the second charge can be obtained from the observed charge capacity (242 mAh/g) in the second cycle as

$$Li_{0.873}[Li_{0.073}M_{0.8}]O_{1.7\ \ 0.047} \rightarrow Li_{0.104}[Li_{0.073}M_{0.8}]O_{1.7\ \ 0.047} + 0.769\ Li^+ + 0.769\ e^- \qquad (5)$$

This outcome reveals that 15.7 % of the oxide ion vacancies are retained in the lattice after the second charge.

Let us now compare this value with the fraction of oxide ion vacancies retained after the second charge in the cell with an extraction of 0.9 lithium ions during first charge. Based on the experimentally observed capacity values, we can assume that reactions (6) and (7) occur in the plateau region of the first charge and reaction (8) occurs during the first discharge much like reactions (2), (3), and (4):

$$Li_{0.6}[Li_{0.2}M_{0.8}]O_2 \rightarrow Li_{0.1}[Li_{0.2}M_{0.8}]O_{1.75\ \ 0.25} + 0.5\ Li^+ + 0.5\ e^- + 0.125\ O_2 \qquad (6)$$

$$Li_{0.1}[Li_{0.2}M_{0.8}]O_{1.75\ \ 0.25} \rightarrow Li_{0.214}[Li_{0.086\ \ 0.114}M_{0.8}]O_{1.75\ \ 0.25}$$

$$\rightarrow Li_{0.214}[Li_{0.086}M_{0.8}]O_{1.75\ \ 0.022} \qquad (7)$$

$$Li_{0.214}[Li_{0.086}M_{0.8}]O_{1.75\ \ 0.022} + 0.672\ Li^+ + 0.672\ e^- \rightarrow Li_{0.886}[Li_{0.086}M_{0.8}]O_{1.75\ \ 0.022} \qquad (8)$$

However, the small plateau region attributed to the oxidation of O^{2-} ions during the second charge causes a divergence from reaction (5) to reactions (9), (10), and (11). The second charge capacity (255 mAh/g) corresponds to an extraction of 0.810 lithium ions from the lattice. The initial extraction of 0.672 lithium ions occurs due to the oxidation of the transition metals ions as

$$Li_{0.886}[Li_{0.086}M_{0.8}]O_{1.75\ \ 0.022} \rightarrow Li_{0.214}[Li_{0.086}M_{0.8}]O_{1.75\ \ 0.022} + 0.672\ Li^+ + 0.672\ e^- \qquad (9)$$

The extraction of the remaining 0.138 lithium ions from the lattice occurs as a result of the oxidation of O^{2-} ions to oxygen. The composition at the end of second-charge can be obtained from reactions (10) and (11) as

$$Li_{0.214}[Li_{0.086}M_{0.8}]O_{1.75\ \ 0.022}$$

$$\rightarrow Li_{0.076}[Li_{0.086}M_{0.8}]O_{1.681\ \ 0.091} + 0.138\ Li^+ + 0.138\ e^- + 0.0345\ O_2 \qquad (10)$$

$$Li_{0.076}[Li_{0.086}M_{0.8}]O_{1.681\ \ 0.091} \rightarrow Li_{0.083}[Li_{0.079\ \ 0.007}M_{0.8}]O_{1.681\ \ 0.091}$$

$$\rightarrow Li_{0.083}[Li_{0.079}M_{0.8}]O_{1.681\ \ 0.077} \qquad (11)$$

This result shows that 24.1 % of the oxide ion vacancies are retained in the lattice after the second charge in the cell with an extraction of 0.9 lithium ions during first charge. Therefore, a higher percentage of oxide ion vacancies are retained in the cell with

an extraction of 0.9 lithium ions during first charge compared to the 15.7 % retention in the cell with 4.8 V cut-off during first charge. The retention of higher number of oxide-ion vacancies and lithium sites, along with the suppression of the Li^+/H^+ exchange side reaction, could account for the improved electrochemical performance in terms of lower C_{irr}, higher discharge capacity, and enhanced cyclability of the cell with a controlled extraction of 0.9 lithium ions during first charge.

Table 8.3 Calculated compositions of the lithium-rich layered oxides during the first and second cycle with different first charge conditions.

Sample	Number of Li^+ extracted during 1st charge	First cycle		Second cycle	% Oxide ion vacancy retention after 2nd charge
		End of charge	End of discharge	End of charge	
$Li[Li_{0.2}Mn_{0.54}Ni_{0.13}Co_{0.13}]O_2$ Controlled	0.9	$Li_{0.204}[Li_{0.092}M_{0.8}]O_{1.717\ \ 0.067}$	$Li_{0.892}[Li_{0.092}M_{0.8}]O_{1.717\ \ 0.067}$	$Li_{0.058}[Li_{0.071}M_{0.8}]O_{1.633\ \ 0.108}$	29.4
$Li[Li_{0.2}Mn_{0.54}Ni_{0.13}Co_{0.13}]O_2$ 4.8 V Cut-Off	1.07	$Li_{0.0695}[Li_{0.062}M_{0.8}]O_{1.634\ \ 0.089}$	$Li_{0.862}[Li_{0.062}M_{0.8}]O_{1.634\ \ 0.089}$	$Li_{0.016}[Li_{0.062}M_{0.8}]O_{1.634\ \ 0.089}$	24.3
$Li[Li_{0.2}Mn_{0.6}Ni_{0.17}Co_{0.03}]O_2$ Controlled	0.9	$Li_{0.211}[Li_{0.091}M_{0.8}]O_{1.730\ \ 0.053}$	$Li_{0.892}[Li_{0.091}M_{0.8}]O_{1.730\ \ 0.053}$	$[Li_{0.066\ \ 0.007}M_{0.8}]O_{1.612\ \ 0.135}$	34.8
$Li[Li_{0.2}Mn_{0.6}Ni_{0.17}Co_{0.03}]O_2$ 4.8 V Cut-Off	1.11	$Li_{0.033}[Li_{0.064}M_{0.8}]O_{1.627\ \ 0.101}$	$Li_{0.864}[Li_{0.064}M_{0.8}]O_{1.627\ \ 0.101}$	$Li_{0.002}[Li_{0.064}M_{0.8}]O_{1.627\ \ 0.101}$	27.1
$Li[Li_{0.2}Mn_{0.6}Ni_{0.2}]O_2$ Controlled	0.9	$Li_{0.214}[Li_{0.086}M_{0.8}]O_{1.75\ \ 0.022}$	$Li_{0.886}[Li_{0.086}M_{0.8}]O_{1.75\ \ 0.022}$	$Li_{0.083}[Li_{0.079}M_{0.8}]O_{1.681\ \ 0.077}$	24.1
$Li[Li_{0.2}Mn_{0.6}Ni_{0.2}]O_2$ 4.8 V Cut-Off	1.0	$Li_{0.125}[Li_{0.073}M_{0.8}]O_{1.7\ \ 0.047}$	$Li_{0.873}[Li_{0.073}M_{0.8}]O_{1.7\ \ 0.047}$	$Li_{0.104}[Li_{0.073}M_{0.8}]O_{1.7\ \ 0.047}$	15.7

8.4 CONCLUSIONS

It has been shown with three lithium-rich compositions, $Li[Li_{0.2}Mn_{0.54}Ni_{0.13}Co_{0.13}]O_2$, $Li[Li_{0.2}Mn_{0.6}Ni_{0.17}Co_{0.03}]O_2$, and $Li[Li_{0.2}Mn_{0.6}Ni_{0.2}]O_2$, that their electrochemical performances can be improved by controlling the amount of lithium ions extracted from the layered lattice during the first charge process. The samples with the controlled first charge process show better electrochemical performances in terms of higher discharge capacity, lower irreversible capacity loss, improved cyclability, and enhanced rate capability. A detailed analysis of the first and second charge-discharge cycles supports the argument that a higher number of oxide ion vacancies and lithium sites are retained in the layered lattice at the end of second charge, resulting in lower irreversible capacity loss and higher discharge capacity. A shorter 4.5 V plateau during the first charge process could also suppress side reactions with the electrolyte involving Li^+/H^+ exchange. This study demonstrates that controlling the amount of lithium ions extracted during the first charge process could be a simple and viable approach to enhance the electrochemical performances of lithium-rich layered oxides without requiring post-chemical process such as coating with other materials or acid treatment.

Chapter 9: Summary

With an aim to develop a firm understanding of the unique characteristics of the layered-spinel composites along with their component phases (the high-capacity lithium-rich layered oxide Li[Li,Mn,Ni,Co]O_2 and the high-voltage spinel oxide $LiMn_{1.5}Ni_{0.5}O_4$), the structural and electrochemical characteristics of layered-spinel composite oxides xLi[$Li_{0.2}M_{0.8}$]O_2–(1-x) Li[$Mn_{1.5}M_{0.5}$]O_4 ($0 \leq x \leq 1$), (M = Mn, Ni, Co) have been systematically investigated.

First, the effect of cation ordering on both the electrochemical and structural characteristics of $LiMn_{1.5}Ni_{0.5}O_4$ when operated between 5.0 and 2.0 V was investigated. Structural studies revealed that the cation ordering affects the size of the empty-octahedral sites in the spinel $LiMn_{1.5}Ni_{0.5}O_4$. The differing sizes of the empty-octahedral sites highly influence the discharge profile below 3 V due to the differences in lattice distortion during lithium ion insertion into the 16c octahedral sites. *Ex-situ* XRD analysis confirms that the evolution of the two tetragonal phases (T1 and T2) is linked to the two distinct ~ 2.7 and ~ 2.1 V plateaus corresponding to the insertion of lithium ions into the 16c octahedral sites. The evolution of the new tetragonal phase (T2) is due to the additional lattice strain/distortion caused by the lithium ion insertion into 16c octahedral sites in addition to the lattice distortion caused by the Jahn−Teller distortion of Mn^{3+} ions as the 16c sites in the disordered phase are smaller than the lithium ions. Both the volume and the *c/a* ratio changes associated with the cubic to T1 and T2 phase transitions cause unacceptable capacity fade when $LiMn_{1.5}Ni_{0.5}O_4$ is cycled between 5.0 – 2.0 V.

From the electrochemical analysis, it is found that specific dopant ions alter the degree of cation ordering in the doped $LiMn_{1.5}Ni_{0.5-x}M_xO_4$ (M = Cr, Fe, Co, and Ga) spinels. The difference in lattice strain, which originates from the size difference between

the Mn^{4+} and the M^{3+} (M = Cr, Fe, Co, and Ga) dopant ions in the ordered $LiMn_{1.5}Ni_{0.5-x}M_xO_4$ spinel phase, explains the origin of the variation in the degree of cation ordering. Among the doped samples, the Co-doped sample shows the highest degree of cation disordering due to the non-surface-segregation character of the Co dopant ions and the consequent decrease in the Ni^{2+} ion concentration in the bulk compared to that in other doped samples.

For the first time, the compositional and wt. % variations of the layered and spinel phases from the nominal values in the layered-spinel composite system $xLi[Li_{0.2}Mn_{0.6}Ni_{0.17}Co_{0.03}]O_2 - (1-x)Li[Mn_{1.5}Ni_{0.425}Co_{0.075}]O_4$ ($0 \leq x \leq 1$) were obtained by employing a joint XRD and ND Rietveld refinement method. *Ex-situ* XRD data analysis indicates that the entire layered phase (*C2/m*) transforms irreversibly into a spinel phase (*Fd*-3*m*) in the composite cathodes during extended electrochemical cycling. Higher lithium occupancy in the transition metal layer of the layered phase appears to be the driving force for this facile structural transformation. As suggested by first principles calculations in the literature, the migration of lithium ions from the transition metal layer into the tetrahedral sites and the subsequent formation of Li-Li dumbbells during the charging process facilitate the formation of a spinel-like phase with an extremely low energy. Electrochemical data analysis suggests that the transformed cubic spinel phase (*Fd*-3*m*) consists of Mn and Ni in the 4+ state with part of the 16d octahedral sites occupied by lithium ions as, for example, in $Li[Li_{1/3}Ni_{1/2}Mn_{7/6}]O_4$. Such a spinel phase can only insert lithium into the empty 16c octahedral sites in the 3 V region without any plateau in the 4 or 4.7 V region as Mn and Ni are present in the 4+ state. In addition, $Li[Li_{1/3}Ni_{1/2}Mn_{7/6}]O_4$ does not suffer from Jahn-Teller distortion or Mn dissolution because Mn remains in the 4+ state during the charge-discharge process.

An investigation on the influence of synthesis temperature revealed that the electrochemical characteristics of both the layered and spinel phases in the composites are highly affected by the synthesis temperature due to changes in surface area and cation ordering. While no significant compositional or weight percent variations were found by altering the synthesis temperature, the electrochemical characteristics of both the layered and spinel phases were drastically altered by the synthesis temperature. The capacity from the layered phase increases with decreasing synthesis temperature due to the increased surface area. For the spinel phase, the synthesis temperature greatly influences the discharge profile below 3 V due to the decrease in lattice distortion during lithium ion insertion into 16c octahedral site, which is caused by the increase in cation ordering with decreasing synthesis temperature.

In addition, the electrochemical performance of the lithium-rich layered oxide $Li[Li,Mn,Ni,Co]O_2$ was improved by blending it with a lithium-free insertion host, $VO_2(B)$, and controlling the amount of lithium ions extracted from the layered lattice during the first charge process. The incorporation of the lithium-free insertion host $VO_2(B)$ into the lithium-rich layered oxide decreases the irreversible capacity loss as it can accept the lithium ions that cannot be inserted back into the layered oxide lattice. The samples with the controlled first charge process show better electrochemical performance in terms of higher discharge capacity, lower irreversible capacity loss, improved cyclability, and enhanced rate capability. A detailed analysis of the first and second charge-discharge cycles supports the argument that a higher number of oxide ion vacancies and lithium sites are retained in the layered lattice at the end of the second charge, which results in a lower irreversible capacity loss and higher discharge capacity. A shorter 4.5 V plateau during the first charge process could also suppress side reactions with the electrolyte involving a Li^+/H^+ ion exchange.

Overall, the study suggests that tailored and optimized electrochemical characteristics of layered-spinel composite oxide cathodes could be possible by controlling the transition metal composition, synthesis temperature, degree of cation ordering in the spinel phase, and the particle size of the samples.

1. K. Ozawa, *Lithium Ion Rechargeable Batteries*, WILEY-VCH Verlag GmbH & Co. KGaA, Weinheim, 2009.

2. J. B. Goodenough and Y. Kim, *Chemistry of Materials*, 2010, **22**, 587-603.

3. A. Mendiboure, C. Delmas and P. Hagenmuller, *Materials Research Bulletin*, 1984, **19**, 1383-1392.

4. A. Manthiram, in *New Trends in Intercalation Compounds for Energy Storage*, eds. C. Julien, J. P. Pereira-Ramos and A. Momchilov, Kluwer Academic Publisher, 2002, p. 177.

5. R. V. Chebiam, A. M. Kannan, F. Prado and A. Manthiram, *Electrochemistry Communications*, 2001, **3**, 624-627.

6. R. V. Chebiam, F. Prado and A. Manthiram, *Journal of Solid State Chemistry*, 2002, **163**, 5-9.

7. S. Venkatraman and A. Manthiram, *Chemistry of Materials*, 2003, **15**, 5003-5009.

8. S. Venkatraman and A. Manthiram, *Chemistry of Materials*, 2002, **14**, 3907-3912.

9. J. Morales, C. Perez-Vicente and J. L. Tirado, *Materials Research Bulletin*, 1990, **25**, 623-630.

10. H. Arai, S. Okada, H. Ohtsuka, M. Ichimura and J. Yamaki, *Solid State Ionics*, 1995, **80**, 261-269.

11. T. Ohzuku, A. Ueda and M. Nagayama, *Journal of The Electrochemical Society*, 1993, **140**, 1862-1870.

12. R. Kanno, H. Kubo, Y. Kawamoto, T. Kamiyama, F. Izumi, Y. Takeda and M. Takano, *Journal of Solid State Chemistry*, 1994, **110**, 216-225.

13. C. Delmas, I. Saadoune and A. Rougier, *Journal of Power Sources*, 1993, **44**, 595-602.

14. R. J. Gummow and M. M. Thackeray, *Solid State Ionics*, 1992, **53**, 681-687.

15. K. M. Shaju, G. V. Subba Rao and B. V. R. Chowdari, *Electrochimica Acta*, 2002, **48**, 145-151.

16. I. Belharouak, Y. K. Sun, J. Liu and K. Amine, *Journal of Power Sources*, 2003, **123**, 247-252.

17. N. Yabuuchi and T. Ohzuku, *Journal of Power Sources*, 2003, **119**, 171-174.

18. T. Ohzuku, A. Ueda and M. Kouguchi, *Journal of The Electrochemical Society*, 1995, **142**, 4033-4039.

19. J. Choi and A. Manthiram, *Electrochemical and Solid-State Letters*, 2005, **8**, C102-C105.

20. J. Choi and A. Manthiram, *Journal of The Electrochemical Society*, 2005, **152**, A1714-A1718.

21. J. O. Besenhard, in *Handbook of Battery Materials*, ed. J. O. Besenhard, Wiley-VCH, Weinheim, 1999.

22. M. M. Thackeray, *Journal of The Electrochemical Society*, 1995, **142**, 2558-2563.

23. M. M. Thackeray, Y. Shao, Horn, A. J. Kahaian, K. D. Kepler, E. Skinner, J. T. Vaughey and S. A. Hackney, *Electrochemical and Solid-State Letters*, 1998, **1**, 7-9.

24. T. Ohzuku, M. Kitagawa and T. Hirai, *Journal of The Electrochemical Society*, 1990, **137**, 769-775.

25. D. H. Jang, Y. J. Shin and S. M. Oh, *Journal of The Electrochemical Society*, 1996, **143**, 2204-2211.

26. Y. Shin and A. Manthiram, *Journal of The Electrochemical Society*, 2004, **151**, A204-A208.

27. J. Kim and A. Manthiram, *Journal of The Electrochemical Society*, 1998, **145**, L53-L55.

28. S. Choi and A. Manthiram, *Journal of The Electrochemical Society*, 2000, **147**, 1623-1629.

29. M. H. Rossouw, A. de Kock, L. A. de Picciotto, M. M. Thackeray, W. I. F. David and R. M. Ibberson, *Materials Research Bulletin*, 1990, **25**, 173-182.

30. A. de Kock, M. H. Rossouw, L. A. de Picciotto, M. M. Thackeray, W. I. F. David and R. M. Ibberson, *Materials Research Bulletin*, 1990, **25**, 657-664.

31. K. Amine, H. Tukamoto, H. Yasuda and Y. Fuiita, *Journal of The Electrochemical Society*, 1996, **143**, 1607-1613.

32. Q. Zhong, A. Bonakclarpour, M. Zhang and J. R. Dahn, *Journal of The Electrochemical Society*, 1997, **144**, 205-205.

33. A. K. Padhi, K. S. Nanjundaswamy, C. Masquelier, S. Okada and J. B. Goodenough, *Journal of The Electrochemical Society*, 1997, **144**, 1609-1613.

34. H. Huang, S. C. Yin and L. F. Nazar, *Electrochemical and Solid-State Letters*, 2001, **4**, A170-A172.

35. T. Muraliganth, A. V. Murugan and A. Manthiram, *Journal of Materials Chemistry*, 2008, **18**, 5661-5668.

36. A. V. Murugan, T. Muraliganth and A. Manthiram, *The Journal of Physical Chemistry C*, 2008, **112**, 14665-14671.

37. A. Vadivel Murugan, T. Muraliganth and A. Manthiram, *Electrochemistry Communications*, 2008, **10**, 903-906.

38. A. Manthiram, *The Journal of Physical Chemistry Letters*, 2011, **2**, 176-184.

39. Z. Lu, D. D. MacNeil and J. R. Dahn, *Electrochemical and Solid-State Letters*, 2001, **4**, A191-A191.

40. Z. Lu, L. Y. Beaulieu, R. a. Donaberger, C. L. Thomas and J. R. Dahn, *Journal of The Electrochemical Society*, 2002, **149**, A778-A778.

41. C. S. Johnson, N. Li, C. Lefief and M. M. Thackeray, *Electrochemistry Communications*, 2007, **9**, 787-795.

42. J. Breger, Y. S. Meng, Y. Hinuma, S. Kumar and K. Kang, *Chemistry of Materials*, 2006, **18**, 4768-4781.

43. X.-Q. Yang, J. McBreen, W.-S. Yoon and C. P. Grey, *Electrochemistry Communications*, 2002, **4**, 649-654.

44. A. R. Armstrong, S.-H. Kang, M. Holzapfel, P. Nova, M. M. Thackeray and P. G. Bruce, *Journal of American Chemical Society*, 2006, **128**, 8694-8698.

45. A. Boulineau, L. Simonin, J.-F. Colin, E. Canévet, L. Daniel and S. Patoux, *Chemistry of Materials*, 2012, 120830053707002.

46. C. S. Johnson, N. Li, J. Vaughey, S. Hackney and M. M. Thackeray, *Electrochemistry Communications*, 2005, **7**, 528-536.

47. J. Liu and A. Manthiram, *Chemistry of Materials*, 2009, **21**, 1695-1707.

48. Y. Wu, A. Vadivel Murugan and A. Manthiram, *Journal of The Electrochemical Society*, 2008, **155**, 635-641.

49. Y. Wu and A. Manthiram, *Solid State Ionics*, 2009, **180**, 50-56.

50. J. R. Croy, D. Kim, M. Balasubramanian, K. Gallagher, S.-H. Kang and M. M. Thackeray, *Journal of The Electrochemical Society*, 2012, **159**, A781.

51. J. Liu, Q. Wang, B. Reeja-Jayan and A. Manthiram, *Electrochemistry Communications*, 2010, **12**, 750-753.

52. J. Liu and B. Reeja-Jayan, *The Journal of Physical Chemistry C*, 2010, **114**, 9528-9533.

53. J. Liu and A. Manthiram, *Journal of Materials Chemistry*, 2010, **20**, 3961-3967.

54. Q. Y. Wang, J. Liu, A. V. Murugan and A. Manthiram, *Journal of Materials Chemistry*, 2009, **19**, 4965-4972.

55. C. S. Johnson, J. Kim, C. Lefief, N. Li, J. Vaughey and M. M. Thackeray, *Electrochemistry Communications*, 2004, **6**, 1085-1091.

56. J. S. Kim, C. S. Johnson, J. T. Vaughey and M. M. Thackeray, *Journal of Power Sources*, 2006, **153**, 258-264.

57. J. Gao and A. Manthiram, *Journal of Power Sources*, 2009, **191**, 644-647.

58. J. Gao, J. Kim and A. Manthiram, *Electrochemistry Communications*, 2009, **11**, 84-86.

59. A. Ito, D. Li, Y. Sato, M. Arao, M. Watanabe, M. Hatano, H. Horie and Y. Ohsawa, *Journal of Power Sources*, 2010, **195**, 567-573.

60. A. Ito, D. Li, Y. Ohsawa and Y. Sato, *Journal of Power Sources*, 2008, **183**, 344-346.

61. K. Nakahara, M. Tabuchi, S. Kuroshima, A. Toda, K. Tanimoto and K. Nakano, *Journal of The Electrochemical Society*, 2012, **159**, A1398-A1404.

62. K. Amine, H. Tukamoto, H. Yasuda and Y. Fujita, *Journal of Power Sources*, 1997, **68**, 604-608.

63. S.-T. Myung, S. Komaba, N. Kumagai, H. Yashiro, H.-T. Chung and T.-H. Cho, *Electrochimica Acta*, 2002, **47**, 2543-2549.

64. J. Kim, S. Myung, C. S. Yoon, S. G. Kang and Y. Sun, *Chemistry of Materials*, 2004, **16**, 906-914.

65. R. Alcantara, M. Jaraba, P. Lavela and J. L. Tirado, *Electrochimica Acta*, 2002, **47**, 1829-1835.

66. P. Strobel, A. Ibarra-Palos, M. Anne, C. Poinsignon and A. Crisci, *Solid State Sciences*, 2003, **5**, 1009-1018.

67. K. Ariyoshi, Y. Iwakoshi and N. Nakayama, *Journal of The Electrochemical Society*, 2004, 296-303.

68. S. H. Park, S.-W. Oh, C.-S. Yoon, S.-T. Myung and Y.-K. Sun, *Electrochemical and Solid-State Letters*, 2005, **8**, A163-A163.

69. S. Park, S. Oh, S. H. Kang, I. Belharouak, K. Amine and Y. Sun, *Electrochimica Acta*, 2007, **52**, 7226-7230.

70. Y. J. Lee, C. Eng and C. P. Grey, *Journal of The Electrochemical Society*, 2001, **148**, A249-A249.

71. T. A. Arunkumar and A. Manthiram, *Electrochemical and Solid-State Letters*, 2005, **8**, A403-A403.

72. D. W. Shin, C. A. Bridges, A. Huq, M. P. Paranthaman and A. Manthiram, *Chemistry of Materials*, 2012, DOI: 10.1021/cm301844w.

73. J. Liu and A. Manthiram, *Journal of The Electrochemical Society*, 2009, **156**, A66-A66.

74. J. Cabana, C. S. Johnson, X. Q. Yang, K. Y. Chung, W.-S. Yoon, S. H. Kang, M. M. Thackeray and C. P. Grey, *Journal of Materials Research*, 2010, **25**, 1601-1616.

75. S. Park, S. H. Kang, C. S. Johnson, K. Amine and M. M. Thackeray, *Electrochemistry Communications*, 2007, **9**, 262-268.

76. J. Cabana, S. H. Kang, C. S. Johnson, C. P. Grey and M. M. Thackeray, *Journal of The Electrochemical Society*, 2009, **156**, A730-A730.

77. H. Deng, I. Belharouak, Y.-K. Sun and K. Amine, *Journal of Materials Chemistry*, 2009, **19**, 4510-4510.

78. H. Deng, I. Belharouak, R. E. Cook, H. Wu, Y.-k. Sun and K. Amine, *Journal of The Electrochemical Society*, 2010, **157**, A447-A452.

79. M. Winter, J. O. Besenhard, M. E. Spahr and P. Novák, *Advanced Materials*, 1998, **10**, 725-763.

80. U. Kasavajjula, C. Wang and A. J. Appleby, *Journal of Power Sources*, 2007, **163**, 1003-1039.

81. M. Winter and J. O. Besenhard, *Electrochimica Acta*, 1999, **45**, 31-50.

82. D. Larcher, S. Beattie, M. Morcrette, K. Edstrom, J.-C. Jumas and J.-M. Tarascon, *Journal of Materials Chemistry*, 2007, **17**, 3759-3772.

83. R. Benedek and M. M. Thackeray, *Journal of Power Sources*, 2002, **110**, 406-411.

84. http://www.sony.net/SonyInfo/News/Press/200502/05-006E/.

85. J. L. Goldman, B. R. Long, A. A. Gewirth and R. G. Nuzzo, *Advanced Functional Materials*, 2011, **21**, 2411-2411.

86. G. Liu, S. Xun, N. Vukmirovic, X. Song, P. Olalde-Velasco, H. Zheng, V. S. Battaglia, L. Wang and W. Yang, *Advanced Materials*, 2011, **23**, 4679-4683.

87. T. Ohzuku, A. Ueda and N. Yamamoto, *Journal of The Electrochemical Society*, 1995, **142**, 1431-1435.

88. P. Reale, S. Panero, B. Scrosati, J. Garche, M. Wohlfahrt-Mehrens and M. Wachtler, *Journal of The Electrochemical Society*, 2004, **151**, A2138-A2142.

89. A. Y. Shenouda and K. R. Murali, *Journal of Power Sources*, 2008, **176**, 332-339.

90. W.-J. Zhang, *Journal of Power Sources*, 2011, **196**, 13-24.

91. J. Fuller, R. T. Carlin and R. A. Osteryoung, *Journal of The Electrochemical Society*, 1997, **144**, 3881-3886.

92. F. Croce, L. Settimi and B. Scrosati, *Electrochemistry Communications*, 2006, **8**, 364-368.

93. J. B. Bates, N. J. Dudney, B. Neudecker, A. Ueda and C. D. Evans, *Solid State Ionics*, 2000, **135**, 33-45.

94. J. Fuller, A. C. Breda and R. T. Carlin, *Journal of The Electrochemical Society*, 1997, **144**, L67-L70.

95. G. Schuck, A. Iwata, A. Sasaki, A. Himeda, H. Konaka and N. Muroyama, *Acta Crystallographica*, 2010, **A66**, S311.

96. A. C. Larson and R. B. V. Dreele, in *Los Alamos National Laboratory Report LAUR*, Los Alamos National Laboratory, Los Alamos, NM, USA, 2000, p. 86.

97. B. H. Toby, *Journal of Applied Crystallography*, 2001, **34**, 210-213.

98. A. Huq, J. P. Hodges, O. Gourdon and L. Heroux, *Zeitschrift für Kristallographie Proceedings*, 2011, **1**, 127.

99. K. M. Shaju and P. G. Bruce, *Dalton Transactions*, 2008, 5471-5475.

100. Y. Idemoto, H. Sekine, K. Ui and N. Koura, *Solid State Ionics*, 2005, **176**, 299-306.

101. A. Caballero, M. Cruz, L. Hernan, M. Melero, J. Morales and E. R. Castellon, *Journal of The Electrochemical Society*, 2005, **152**, A552-A559.

102. M. Kunduraci, J. F. Al-Sharab and G. G. Amatucci, *Chemistry of Materials*, 2006, **18**, 3585-3592.

103. M. Kunduraci and G. G. Amatucci, *Journal of Power Sources*, 2007, **165**, 359-367.

104. M. Kunduraci and G. G. Amatucci, *Journal of The Electrochemical Society*, 2006, **153**, A1345-A1345.

105. D. Gryffroy and R. Vandenberghe, *Journal of Physics and Chemistry of Solids*, 1992, **53**, 777-784.

106. F. Ooms, *Solid State Ionics*, 2002, **152-153**, 143-153.

107. H. Taguchi, S. Omori, M. Nagao, H. Kido and M. Shimada, *Journal of Solid State Chemistry*, 1995, **118**, 112-116.

108. G. K. Williamson and W. H. Hall, *Acta metallurgica et materialia*, 1953, **1**, 22.

109. Y. Terada, K. Yasaka, F. Nishikawa, T. Konishi, M. Yoshio and I. Nakai, *Journal of Solid State Chemistry*, 2001, **156**, 286-291.

110. M. M. Thackeray, *Progress in Solid State Chemistry*, 1997, **25**, 1-71.

111. G. Bergerhoff, M. Berndt and K. Brandenburg, *Journal of Research of the National Institute of Standards and Technology*, 1996, **101**, 221.

112. A. Ueda and T. Ohzuku, *Journal of The Electrochemical Society*, 1994, **141**, 2010-2014.

113. T. Ohzuku and A. Ueda, *Journal of The Electrochemical Society*, 1994, **141**, 2972-2977.

114. H. Wang, T. A. Tan, P. Yang, M. O. Lai and L. Lu, 2011, 6102-6110.

115. D. Li, a. Ito, K. Kobayakawa, H. Noguchi and Y. Sato, *Journal of Power Sources*, 2006, **161**, 1241-1246.

116. T. A. Arunkumar and A. Manthiram, *Electrochimica Acta*, 2005, **50**, 5568-5572.

117. W. Qin, T. Nagase, Y. Umakoshi and J. A. Szpunar, *Philosophical Magazine Letters*, 2008, **88**, 169-179.

118. T. Ohzuku, *Journal of Power Sources*, 1999, **81-82**, 90-94.

119. M. Kunduraci and G. G. Amatucci, *Electrochimica Acta*, 2008, **53**, 4193-4199.

120. T. A. Arunkumar, Y. Wu and A. Manthiram, *Chemistry of Materials*, 2007, **19**, 3067-3073.

121. Z. Q. Deng and A. Manthiram, *The Journal of Physical Chemistry C*, 2011, **115**, 7097-7103.

122. Y. J. Park, Y.-S. Hong, X. Wu, K. S. Ryu and S. H. Chang, *Journal of Power Sources*, 2004, **129**, 288-295.

123. M. M. Thackeray, C. S. Johnson, J. T. Vaughey, N. Li and S. A. Hackney, *Journal of Materials Chemistry*, 2005, **15**, 2257-2267.

124. J. Breger, M. Jiang, N. Dupre, Y. Meng, Y. Shaohorn, G. Ceder and C. Grey, *Journal of Solid State Chemistry*, 2005, **178**, 2575-2585.

125. C. S. Johnson, N. Li, C. Lefief, J. T. Vaughey and M. M. Thackeray, *Lithium*, 2008, **2**, 6095-6106.

126. P. S. Whitfield, I. J. Davidson, P. W. Stephens, L. M. D. Cranswick and I. P. Swainson, *Z. Krist.*, 2011, **26**, 483-488.

127. C. Lei, J. Bareno, J. Wen, I. Petrov, S.-H. Kang and D. Abraham, *Journal of Power Sources*, 2008, **178**, 422-433.

128. K. A. Jarvis, Z. Deng, L. F. Allard, A. Manthiram and P. J. Ferreira, *Chemistry of Materials*, 2011, 3614-3621.

129. Y. S. Meng, G. Ceder, C. P. Grey, W.-S. Yoon, M. Jiang and J. Breger, *Chemistry of Materials*, 2005, **2**, 2386-2394.

130. C. R. Fell, K. J. Carroll, M. Chi and Y. S. Meng, *Journal of The Electrochemical Society*, 2010, **157**, A1202-A1202.

131. P. Kalyani, S. Chitra, T. Mohan and S. Gopukumar, *Journal of Power Sources*, 1999, **80**, 103-106.

132. A. D. Robertson and P. G. Bruce, *Chemistry of Materials*, 2003, **15**, 1984-1992.

133. Z. Lu and J. R. Dahn, *Journal of The Electrochemical Society*, 2002, 815-822.

134. B. Xu, C. R. Fell, M. Chi and Y. S. Meng, *Energy & Environmental Science*, 2011, **4**, 2223-2233.

135. T. Ohzuku and A. Ueda, *Solid State Ionics*, 1994, **69**, 201-211.

136. M. M. Thackeray, A. Kock, M. H. Rossouw and D. Liles, *Journal of The Electrochemical Society*, 1992, **139**, 363-363.

137. A. D. Robertson, A. R. Armstrong and P. G. Bruce, *Chemistry of Materials*, 2001, **13**, 2380-2386.

138. A. R. Armstrong and P. G. Bruce, *Nature*, 1996, **381**, 499-499.

139. P. G. Bruce, a. R. Armstrong and R. L. Gitzendanner, *Journal of Materials Chemistry*, 1999, **9**, 193-198.

140. Y.-M. Chiang, H. Wang and Y.-I. Jang, *Chemistry of Materials*, 2000, **13**, 53-63.

141. S. Park, H. Ahn, G. Park, J. Kim and Y. Lee, *Materials Chemistry and Physics*, 2008, **112**, 696-701.

142. Y. Idemoto, H. Narai and N. Koura, *Journal of Power Sources*, 2003, **119**, 125-129.

143. D. Y. W. Yu, K. Yanagida, Y. Kato and H. Nakamura, *Journal of The Electrochemical Society*, 2009, **156**, A417-A417.

144. A. M. Kannan and A. Manthiram, *Solid State Ionics*, 2003, **159**, 265-271.

145. K.-S. Park, A. Benayad, M.-S. Park, W. Choi and D. Im, *Chemical Communications*, 2010, **46**, 4190-4192.

146. G. Armstrong, J. Canales, A. R. Armstrong and P. G. Bruce, *Journal of Power Sources*, 2008, **178**, 723-728.

147. A. R. Armstrong, A. D. Robertson and P. G. Bruce, *Journal of Power Sources*, 2005, **146**, 275-280.

148. A. D. Robertson and P. G. Bruce, *Chemical Communications*, 2002, 2790-2791.

Vita

Eun Sung Lee was born in 1979, in Seoul, Republic of Korea. He received his B.S. and M.S. degrees in Materials Science and Engineering from Yonsei University in Seoul, Republic of Korea, respectively, in 2003 and 2005. He worked for Hyundai Motor Company as a research engineer from 2005 to 2008 and worked on lithium-ion battery & supercapacitor systems for vehicle application. He entered the graduate school of The University of Texas at Austin in August 2008 and worked on cathode materials for lithium-ion batteries.

Email Address: eunsung79@gmail.com

This dissertation was typed by the author.